Resonant X-Ray Scattering Studies of Ruthenium Oxides and Ruthenocuprates

Von der Fakultät Mathematik und Physik der Universität Stuttgart
zur Erlangung der Würde eines Doktors der Naturwissenschaften
(Dr. rer. nat.) genehmigte Abhandlung

vorgelegt von

Britta Bohnenbuck
aus Dannenberg (Elbe)

Hauptberichter: Prof. Dr. Bernhard Keimer
Mitberichter: Prof. Dr. Peter Michler

Tag der mündlichen Prüfung: 22.06.2009

Max-Planck-Institut für Festkörperforschung
Stuttgart 2009

Contents

Deutsche Zusammenfassung

In der vorliegenden Arbeit wurden die magnetischen und orbitalen Eigenschaften von $Ca_3Ru_2O_7$, Mn haltigem $Sr_3Ru_2O_7$ und $RuSr_2GdCu_2O_8$ mit Hilfe resonanter und hochenergetischen Röntgenbeugung untersucht.
$Ca_3Ru_2O_7$, ein paramagnetisches Metall bei hohen Temperaturen, ordnet antiferromagnetisch unterhalb von $T_N = 56\,\mathrm{K}$, und zeigt einen Metall-Isolator ähnlichen Phasenübergang bei $T_{MI} = 48\,\mathrm{K}$. Dieser wird von abrupten strukturellen Änderungen und einer Reorientierung des magnetischen Moments begleitet. Zudem gibt es Hinweise auf die Existenz orbitaler Ordnung unterhalb von T_{MI}. Zur Klärung der magnetischen Struktur von $Ca_3Ru_2O_7$ wurden resonante Röntgenbeugungsexperimente an den Ru L-Absorptionskanten durchgeführt. Die dabei beobachteten magnetischen Reflexe (001) und (110) sind konsistent mit einer A-Typ antiferromagnetischen Struktur bestehend aus ferromagnetischen Doppelschichten, die antiferromagnetisch entlang der c-Achse gekoppelt sind. Anhand der azimuthalen Abhängigkeit der magnetischen Signale an beiden Reflexen ließ sich zudem die Richtung des magnetische Moments bestimmen. Dieses liegt entlang der b-Achse unterhalb von T_{MI} und entlang der a-Achse zwischen T_{MI} und T_N. Die Reorientierung des magnetischen Momentes bei T_{MI} ist vermutlich auf die starke Spin-Bahn-Kopplung zurückzuführen, aufgrund derer ein ungequenschtes orbitales Moment erwartet wird. Dieses könnte dann zusätzliche Terme im Hamilton-Operator induzieren, die wiederum für die Reorientierung des magnetischen Momentes verantwortlich sind. Letztere könnte zudem mit der Ausbildung orbitaler Ordnung unterhalb von T_{MI} zusammenhängen, für die unterschiedliche experimentelle Methoden zahlreiche indirekte Hinweise geliefert haben. Mit Hilfe resonanter Röntgenbeugung wurden dennoch keine Anzeichen für orbitale Ordnung innerhalb der experimentellen Empfindlichkeit gefunden. Daher ist davon auszugehen, dass die orbitale Ordnung in $Ca_3Ru_2O_7$, sofern überhaupt vorhanden, wesentlich schwächer ist als im einlagigen Ca_2RuO_4. Dies ist vermutlich auf restliche Ladungs- und orbitale Fluktuationen zurückzuführen.
$RuSr_2GdCu_2O_8$ hat aufgrund der Koexistenz von Supraleitung und langreichweitiger magnetischer Ordnung in den letzten Jahren großes wissenschaftliches Interesse geweckt. Da die beiden Phänomene in einem breiten Temperaturbereich koexistieren, eignet sich $RuSr_2GdCu_2O_8$ besonders gut, um eine mögliche Kopplung der entsprechenden Ordnungsparameter zu untersuchen. Über die magnetische Struktur des Materials gibt es jedoch nur wenige Informationen, da bisherige Neutronenmessungen wegen der geringen Masse der verfügbaren Einkristalle nur an Pulverproben durchgeführt wurden. In dieser Situation ist resonante Röntgenbeugung besonders

gut geeignet, da sie sensitiv auf Magnetismus ist, aber im Gegensatz zur Neutronenstreuung nicht auf große Kristallmassen angewiesen ist, so dass auch sehr kleine Einkristalle untersucht werden können. Die Beobachtung der magnetischen Reflexe $(\frac{1}{2}\ \frac{1}{2}\ \frac{1}{2})$ und $(\frac{1}{2}\ \frac{1}{2}\ \frac{3}{2})$ ist konsistent mit einer G-Typ antiferromagnetischen Struktur, die sich durch eine Verdopplung der Einheitszelle entlang aller drei Kristallrichtungen auszeichnet. Aus der azimuthalen Abhängigkeit des magnetischen Signals konnte zudem das magnetische Moment bestimmt werden. Es liegt entlang der Richtung (102) des reziproken Gitters und hat somit einen wesentlichen Beitrag parallel zu den RuO_2 Ebenen wie auch senkrecht zu diesen. Sowohl die magnetische Struktur als auch die Richtung des magnetischen Moments stehen im vollen Einklang mit den Ergebnissen bisheriger Neutronenexperimente und Magnetisierungsmessungen. Außerdem hat eine Symmetrieanalyse ergeben, dass die experimentell beobachtete G-Typ antiferromagnetische Struktur von einer zusätzlichen ferromagnetischen Komponente in den RuO_2-Ebenen begeleitet werden muss, die zwischen den Schichten alterniert. Diese ferromagnetische Komponente in den RuO_2-Ebenen entspricht jedoch exakt der in NMR und FMR beobachteten Mode. Somit haben die resonanten Röntgenbeugungsmessungen die scheinbar widersprüchlichen Ergebnisse aus Neutronenmessungen einerseits und NMR/FMR andererseits geklärt und damit eine große Kontroverse in der experimentellen Literatur gelöst.
$Sr_3Ru_2O_7$ wird seit der Entdeckung von quantenkristischem Verhalten, das mit dem Auftreten eines metamagnetischen Übergangs zwischen zwei metallischen Phasen verbunden ist, intensiv untersucht. In seinem Grundzustand ist das Material ein paramagnetisches Metall, das sich unterhalb von ungefähr 10K wie eine Fermi-Flüssigkeit verhält. Ersetzt man in $Sr_3Ru_2O_7$ Ru teilweise durch Mn, so wird ein isolierender, antiferromagnetischer Zustand induziert, dessen Übergangstemperatur mit zunehmender Mn-Konzentration steigt. Mit Hilfe resonanter Röntgenbeugung an den Ru L-Ab-sorptionskanten wurde die antiferromagetische Struktur von 10% Mn haltigem $Sr_3Ru_2O_7$untersucht. Dabei ergaben die Messungen an den magnetischen Reflexen $(\frac{1}{4}\ \frac{1}{4}\ 0)$ und $(\frac{3}{4}\ \frac{3}{4}\ 0)$, dass die magnetische Struktur nahezu zweidimensional ist und das magnetische Momente entlang der c-Achse liegt. Des Weiteren sind unsere Ergebnisse mit einer magnetischen Struktur konsistent, die aus ferromagnetischen Streifen entlang der Diagonalen des tetragonalen Gitters besteht. Aus dem Vergleich unserer Daten mit den Ergebnissen bisheriger Neutronenmessungen an 5% Mn haltigem $Sr_3Ru_2O_7$ ergibt sich, dass diese antiferromagnetische Spin-Anordnung unabhängig vom Dotierungsniveau ist. Somit scheint eine antiferromagetische Instabilität bereits im undotierten Material vorhanden zu sein. Daher lassen sich Spekulationen anstellen, ob die beobachtete antiferromagnetische Struktur nicht nur durch Dotierung, sondern auch auf eine andere Weise induziert werden kann, zum Beispiel durch das Anlegen eines äußeren Magnetfelds. Interessanterweise lässt sich das anisotrope Verhalten des elektrischen Widerstands, das in der nematischen Phase von $Sr_3Ru_2O_7$ bei hohen Magnetfeldern beobachtet wurde, sehr gut auf Basis der beschriebenen antiferromagnetischen Struktur erklären. Ob die nematische Phase allerdings tatsächlich die gleiche antiferromagnetische Ordnung aufweist wie Mn haltiges $Sr_3Ru_2O_7$, ist jedoch noch völlig offen, und muss mit Hilfe von de-

taillierten Neutronenmessungen an Einkristallen mit genauer Strukturverfeinerung geklärt werden.

Introduction

Transition metal oxides have been intensively studied in the last years due to their interesting physical phenomena resulting from the complex interplay between spin, charge, lattice and orbital degrees of freedom. However, the strong coupling between the various degrees of freedom makes an understanding of the underlying physics difficult. Ruthenium oxides, commonly named ruthenates, and ruthenocuprates are good examples of this class of materials.
The Ruddlesden-Popper ruthenates $(Ca,Sr)_{n+1}Ru_nO_{3n+1}$ have attracted a lot of interest since the discovery of the p-wave superconducting state in Sr_2RuO_4. Besides the superconductivity, these materials show a wide variety of magnetic and transport properties. Bilayered $Ca_3Ru_2O_7$, an antiferromagnetic insulator in the ground state, shows colossal magnetoresistance effects similar to those observed in several manganates. In addition, the material is extremely sensitive to small perturbation such as uniaxial and hydrostatic pressure, doping and applied magnetic fields, giving rise to a complex phase diagram. Orbital order in combination with strong spin-orbit and magnetoelastic coupling are presumably responsible for the rich phase behavior. The Sr based counterpart $Sr_3Ru_2O_7$, which is a paramagnetic Fermi liquid at low temperatures, exhibits quantum critical behavior, that is related to metamagnetism. Many aspects of the metamagnetic transition are not yet understood, including the the role of magnetic fluctuations and the splitting of the metamagnetic transition, which is accompanied by the formation of an electronic liquid crystal phase.
Ruthenocuprates have simulated a lot of scientific research due to the broad coexistence range of superconductivity and long range magnetic order. In $RuSr_2GdCu_2O_8$, magnetic order is established in the RuO_2 layers at 100-150 K and superconductivity occurs in the CuO_2 planes below 15-50 K. Investigations reported thus far have not indicated any coupling between the corresponding order parameters, however, this cannot be excluded since the nature of the magnetic state is still under debate. While nuclear and ferromagnetic resonance experiments indicate a ferromagnetic coupling of the Ru moments in the RuO_2 layers, neutron powder diffraction studies suggest an antiferromagnetic ordering along all three crystallographic directions. Weak ferromagnetism could then be induced by a small canting of neighboring Ru moments due to the Dzyaloshinski-Moriya interaction. Since high quality single crystals are meanwhile available, the magnetic state of $RuSr_2GdCu_2O_8$ can be investigated in more detail and under better experimental conditions.
X-ray diffraction has been widely used in the last decades for the investigation of transition metal oxides. Besides the traditional use for structure determination, the

high flux of the x-ray beam provided at synchrotron facilities allows the investigation of weak phenomena, such as charge order. By tuning the energy of the x-ray beam close to an absorption edge of the transition metal ions, magnetic and orbital phenomena can also be studied due to the resonant enhancement of the magnetic scattering cross section. In contrast to neutron diffraction, which is usually used for magnetic structure determination, resonant x-ray diffraction allows the investigation of small samples with a scattering volume of less than $10^{-2}\,\mathrm{mm}^3$. This is the major advantage of resonant x-ray scattering compared to other complementary experimental techniques.
The thesis is organized as follows:

- Chapter 1 gives an overview about the mechanisms responsible for the physics of ruthenium oxides and ruthenocuprates. Their electronic structure is described within crystal field theory and band theory. Furthermore, the relevant exchange interactions including the single band Hubbard model are treated and the role of orbital degeneracy and spin-orbit coupling is discussed. Finally, conventional and unconventional superconductors are briefly reviewed.

- The principles of x-ray diffraction are described in Chapter 2. Based on the Hamiltonian of electrons in a quantized electromagnetic field, the scattering amplitude of a magnetic ion is deduced. Thomson scattering and nonresonant x-ray scattering are briefly discussed, followed by a detailed description of resonant x-ray diffraction including the derivation of the polarization and azimuthal dependence of the resonant electric dipole scattering amplitude.

- Chapter 3 describes the laboratory x-ray diffraction setup, used for the prealignment of the crystals, and the synchrotron beamlines, at which the x-ray diffraction studies were carried out.

- The results of resonant x-ray diffraction studies of $Ca_3Ru_2O_7$ are presented in Chapter 4, including information about the magnetic structure, the orientation of the magnetic moment and the existence of orbital order in this compound. These studies are supplemented by high energy x-ray diffraction investigations which focused on the structural changes in an applied magnetic field and confirm the strong spin-charge-lattice coupling in this material.

- Chapter 5 contains the resonant x-ray diffraction data of $RuSr_2GdCu_2O_8$. The experimental results concerning the magnetic structure and the direction of the magnetic moment are complemented by a symmetry analysis and discussed with respect to previous experimental findings.

- Resonant x-ray scattering studies of 10% Mn substituted $Sr_3Ru_2O_7$, performed at the Ru L-absorption edges, are presented in Chapter 6. These contain information about the magnetic structure and the orientation of the magnetic moment. The results are discussed with respect to the electronic liquid crystal phase observed in the parent compound $Sr_3Ru_2O_7$.

- The main results and conclusions of this work are summarized in the last chapter.

Chapter 1

Ruthenium Oxides and Ruthenocuprates

Ruthenium oxides and ruthenocuprates have attracted a great deal of interest in the last years due to the wide variety of their fascinating physical phenomena. Although a complete understanding of the underlying physics is still missing, it is quite clear, that the intimate coupling between spin, charge, lattice and orbital degrees of freedom plays a crucial role. Some of the mechanisms responsible for this strong interplay are discussed in this chapter.

1.1 Crystal structure

The crystal structure of ruthenium oxides and ruthenocuprates can be derived from the ideal perovsikte structure AMO_3, which is shown in Figure 1.1. In this three-dimensional structure, each transition metal ion (M) is surrounded by six oxygen ions (O), which form an octahedron. The lattice is stabilized by the large metallic cations (A). However, the simple cubic structure is rare and most perovskites crystallize in a distorted structure like the orthorhombic $CaTiO_3$.
The perovskite lattice can be regarded as consisting of alternatingly stacked MO_2 and AO layers. The different ruthenium oxides and ruthenocuprates can be deduced by stacking these layers in a different sequence and shifting them with respect to each other. Due to the modified stacking sequence the materials become essentially two-dimensional, which is reflected in almost all physical properties. The bilayered Ruddlesden-Popper ruthenates $(Ca_xSr_{1-x})_3Ru_2O_7$ are a good example of this. They consist of RuO_2 bilayers which are separated by insulating SrO/CaO planes. The crystal symmetry is further lowered by distortions of the RuO_6 octahedra, which strongly depend on the size of the metallic cation. As the Sr ions are gradually substituted by the smaller Ca ions, the crystal structure changes from almost tetragonal to orthorhombic.

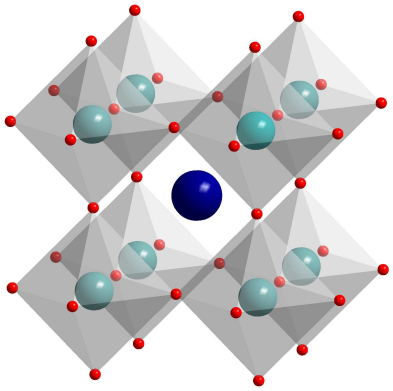

Figure 1.1: Crystal structures of the ideal cubic perovskite AMO_3. The green spheres denote the transition metal ions (M), the blue sphere represents the di- or trivalent cation (A) and the small red spheres are the oxygen-ions (O).

1.2 Electronic Structure

There are basically two approaches to describe the electronic structure of solids [1]. Ionic models focus on the properties of individual ions, assuming that each ion has an integral charge which is given by its oxidation state. Some deficiencies of this view can be taken into account by cluster models where the electronic interactions with the neighboring atoms are considered explicitly. Nevertheless, theses approaches imply a localized electron picture and are hence most suited for the description of insulating solids. In contrast, band models calculate extended electron states based on the wave function of an electron in a periodic potential. Therefore, they are usually applied to metallic solids.
Although ionic models provide a quite naive picture of the electronic structure, they can give qualitative information about the energy levels of the ground and the excited states of a solid, especially of insulators. For this reason, the electronic structure of ruthenates and ruthenocuprates are first discussed using the ionic approach, starting with the crystal field effect. Later, the electronic structure of some ruthenates is described briefly within band theory.

1.2.1 Crystal Field Effect

In the free ruthenium ion, the $4d$ states are characterized by the orbital angular momentum quantum number $l = 2$ and the magnetic quantum number $-2 \leq m \leq 2$ resulting in a five fold degeneracy. However, this is not the case in ruthenates and ruthenocuprates, where each ruthenium ion is surrounded by six oxygen ions which form an octahedron. Hence, the $4d$ electrons of a ruthenium ion are exposed to the Coulomb repulsion of the negatively charged oxygen ions, the so called crystal field

which is described by [2]

$$V_{CF}(\boldsymbol{r}) = \sum_j \frac{Z_i e^2}{|\boldsymbol{R}_j - \boldsymbol{r}|}, \tag{1.1}$$

where $\boldsymbol{r}$ is the position of the $4d$ electron and $\boldsymbol{R}_i$ and $Z_i e$ denote the position and charge of the j-th surrounding ion, respectively. In a cubic crystal field, where all Ru-O distances are equivalent, the wave functions of the $4d$ electrons are no longer spherical harmonics Y_{lm} but are given by linear combination of them:

$$d_{x^2-y^2} \propto \sqrt{\frac{2\pi}{5}}\,(Y_{22} + Y_{2-2}) = \frac{\sqrt{3}}{2}\frac{x^2-y^2}{r^2} \tag{1.2}$$

$$d_{3z^2-r^2} \propto \sqrt{\frac{4\pi}{5}} Y_{20} = \frac{1}{2}\frac{3z^2-r^2}{r^2} \tag{1.3}$$

$$d_{xy} \propto \frac{1}{i}\sqrt{\frac{2\pi}{5}}\,(Y_{22} + Y_{2-2}) = \sqrt{3}\frac{xy}{r^2} \tag{1.4}$$

$$d_{yz} \propto \sqrt{\frac{2\pi}{5}}\,(Y_{2-1} + Y_{21}) = \sqrt{3}\frac{yz}{r^2} \tag{1.5}$$

$$d_{xz} \propto \frac{1}{i}\sqrt{\frac{2\pi}{5}}\,(Y_{2-1} - Y_{21}) = \sqrt{3}\frac{xz}{r^2} \tag{1.6}$$

The shape of each orbital is shown in Figure 1.2. In the presence of a cubic crystal field, the fivefold degeneracy of the $4d$-states is lifted into the twofold degenerate e_g- and the threefold degenerate t_{2g}-orbitals, as schematically illustrated in Figure 1.3b. This can be qualitatively understood as follows: The e_g-states, consisting of $d_{x^2-y^2}$ and $d_{3z^2-r^2}$, are extended along the ruthenium-oxygen bonds and are therefore strongly influenced by the Coulomb repulsion of the negatively charged oxygen ions. In contrast, the t_{2g}-orbitals, comprising d_{xy}, d_{yz} and d_{xz}, do not point towards the oxygen ions, are less affected by the Coulomb repulsion and thus lie lower in energy than the e_g-levels. The energy splitting between the e_g- and the t_{2g}-states is written as $10Dq$ and typically amounts up to 4 eV in ruthenates [3].

Since the RuO_6 octahedron is usually deformed, the crystal fields of most ruthenates have tetragonal or even lower symmetry. For simplicity, we consider the situation, in which the RuO_6 octahedron is elongated along the z-axis as approximately realized in Sr_2RuO_4. In this case, the degeneracy of the e_g and t_{2g}-orbitals is further lifted as schematically shown in Figure 1.3c. The splitting of the e_g-orbitals is explained as follows: The $d_{3z^2-r^2}$ is extended along the z-axis while the $d_{x^2-y^2}$ is prolonged in the xy-plane. Since the apical oxygens of the RuO_6 octahedron move outwards along the z-axis the Coulomb repulsion for the $d_{3z^2-r^2}$-orbital is smaller with respect to the $d_{x^2-y^2}$-level. Thus, the $d_{3z^2-r^2}$-orbital has a lower energy than the $d_{x^2-y^2}$-level. A similar explanation holds for the t_{2g}-states: The d_{yz}- and d_{xz}-orbitals are extended along the z-axis while the d_{xy}-orbital lies in the xy-plane. The Coulomb interaction of the d_{yz}- and d_{xz}-states with the oxygen ions is therefore weaker than the one of

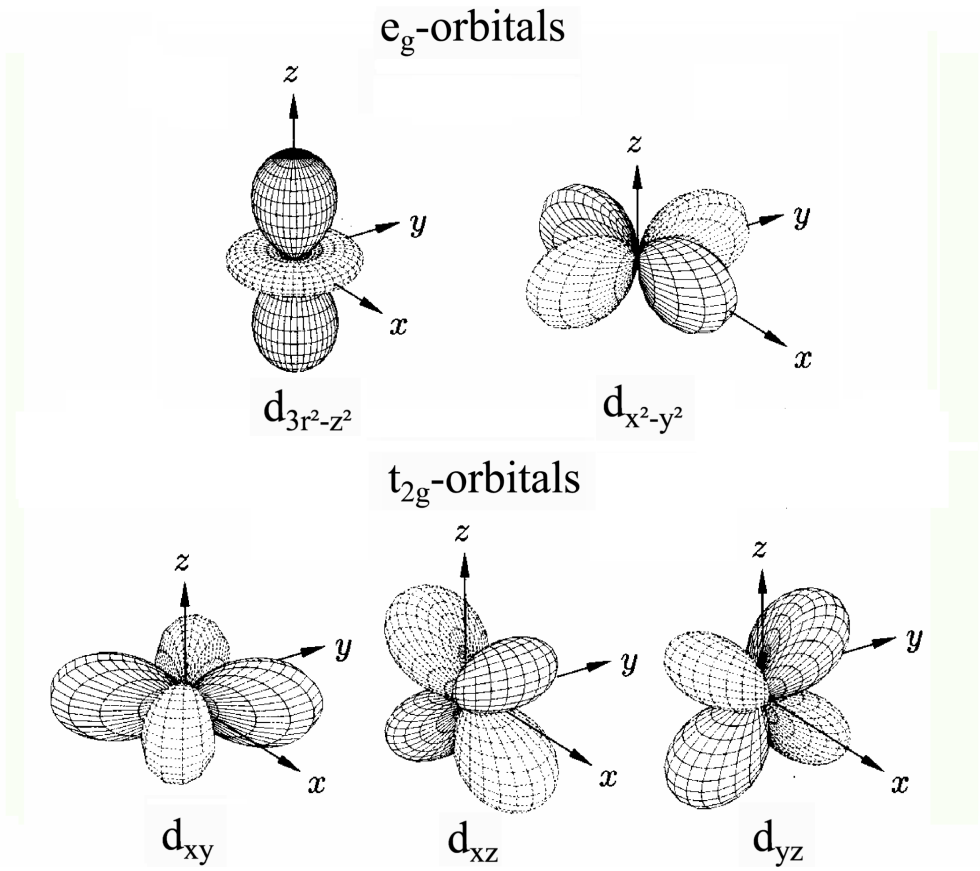

Figure 1.2: The angular distribution of the d-orbitals. In the presence of a cubic crystal field, these split into the twofold degenerate e_g- and the threefold degenerate t_{2g}-orbitals.

the d_{xy}-orbital and the energy of the former is lower than the one of the d_{xy}-level.

In the Ruddlesden-Popper ruthenates $(Ca,Sr)_{n+1}Ru_nO_{3n+1}$, the ruthenium ions are in a Ru^{4+} oxidation state and the $4d$ orbitals are occupied with four electrons. According to Hund's rule one would expect three electrons in the t_{2g}-orbitals and one electron in the e_g-orbital, all having a parallel spin. This electron configuration would correspond to a so called high spin state with a total spin of $S = 2$. However, this is not the case, because the crystal field in ruthenates is quite large ($\approx$ 4eV) and overcomes the Hund's coupling ($\approx$ 1eV). Therefore, a low spin state with a total spin of $S = 1$ is realized and all four electrons occupy the t_{2g}-orbitals, leaving the e_g-states empty. Which of the t_{2g}-levels is doubly occupied, depends essentially on the deformation of the RuO_6 octahedron since it determines the energy splitting among the t_{2g}-levels.

1.2.2 Quenching of Orbital Momentum

Besides lifting the orbital degeneracy, the crystal field is also responsible for the quenching of the orbital angular momentum. In contrast to the free ion, where

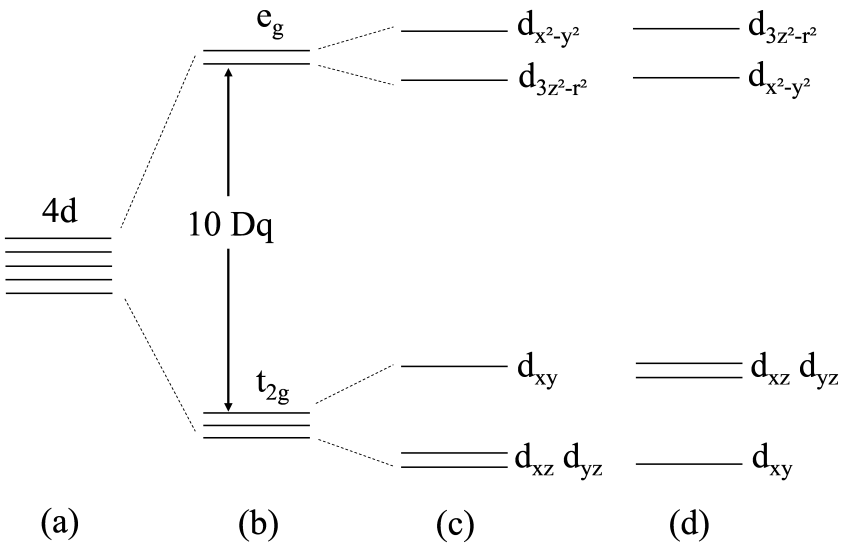

Figure 1.3: Schematic view of energy levels of the 4*d*-orbitals in (a) a free atom, (b) a cubic crystal field, (c) a tetragonal crystal field with elongated octahedron along the z-axis and (d) a tetragonal crystal field with contracted octahedron along the z-axis.

the total magnetic moment is caused by the spin and orbital angular momentum, the latter usually vanishes in a crystal field. As described in the previous section, the eigenstates of the 4*d* electrons are real functions in the presence of a crystal field. Unlike the free ion, where the ground state can be constructed by linear combinations of eigenfunctions belonging to different degenerate states, this is not possible in the presence of a crystal field because the degeneracy is lifted. Hence, the ground state wave function Ψ has to be real. Since the total angular momentum operator $\boldsymbol{L} = -i\hbar\boldsymbol{r} \times \frac{\partial}{\partial \boldsymbol{r}}$ is an imaginary operator, its expectation value for the ground state must be imaginary. On the other hand, the total angular momentum operator $\boldsymbol{L}$ is Hermitian, which requires real eigenvalues. Both conditions can only be met if the total orbital angular moment vanishes, thus

$$\langle \Psi \, | \boldsymbol{L} | \, \Psi \rangle = 0 \tag{1.7}$$

In fact, the orbital angular momentum may not be completely quenched, because the spin-orbit coupling cannot be ignored. This is usually the case for ruthenates, where the spin-orbit interaction can be comparable to the crystal field effect due to the large atomic number of ruthenium.

1.2.3 Jahn-Teller Effect

So far the splitting of energy levels due to the presence of a fixed crystal field has been discussed, indicating a strong coupling between the lattice and the orbital states of the electrons. On the other hand, it is also possible, that the electronic states of a magnetic ion induce a lattice distortion, which tends to lift the remaining orbital

degeneracy by lowering the symmetry of the crystal field. This phenomenon is known as the Jahn-Teller effect [4]. To describe this effect, we consider the distortion of an octahedron along the z-axis, which is quantified by δz. The distortion gives rise to an energy cost that is quadratic in δz and can be expressed as

$$E(\delta z) = B(\delta z)^2. \tag{1.8}$$

The distortion also lifts the orbital degeneracy raising the energy of certain orbitals by $A\,\delta z$ and lowering the energy of others by $-A\,\delta z$. If all orbitals are either completely full or completely empty, the octahedron remains undistorted because the energy level splitting does not yield a reduction of the total energy. However, in case of partially occupied orbitals the energy splitting is relevant and might lead to a net reduction of the total energy. If an orbital is for example occupied by a single electron, the total energy is given by

$$E(\delta z) = -A\,\delta z + B(\delta z)^2, \tag{1.9}$$

and it is energetically favorable for the octahedron to distort by $\delta z = \frac{A}{2B}$. Since the total energy of the crystal needs to be minimized, the Jahn-Teller distortions of the octahedra in a crystal are not independent of each other and show a specific arrangement. The ordering of distortions usually sets in at a particular temperature and is accompanied by a structural phase transition because the global symmetry of the crystal is changed. This phenomenon is called cooperative Jahn-Teller effect.

1.2.4 Band Theory

In band theory, each electron is assumed to move in the crystal potential, determined by the charge distribution of the ion cores and the residual electrons of the solid. The energy levels of the each electron are functions of the crystal momentum $\mathbf{k}$ and thus form energy bands $E_{\mathbf{k}}$. These energy bands are occupied by the electrons of the solid up the Fermi Energy E_F in accordance with Fermi-Dirac statistics. Since the motion of the each electron is independent of the motion of the other electrons, this approach is called mean field approximation or one-electron approximation. By this method, the many-body problem is simplified to a problem of a single electron in a self-consistent mean field potential. In most first-principles band structure calculations the electron-electron interaction in the mean field potential is further simplified by using the so-called local density approximation (LDA).
LDA based band structure calculations have been quite successful in describing the electronic structure of metallic ruthenates such as Sr_2RuO_4 and $Sr_3Ru_2O_7$. The band structure of Sr_2RuO_4 as determined by LDA is highly two-dimensional and is characterized by a strong Ru $4d$ − O $2p$ hybridization [5, 6]. This leads to bonding $e_g - p\sigma$ states at the bottom of the valence band, corresponding anti-bonding states above E_F and hybridized t_{2g} bands near E_F. Three bands cross E_F, which correspond to the three t_{2g}-orbitals (d_{xy}, d_{yz}, d_{xz}). The d_{xy}-band has approximately twice the width of the d_{xz}- and d_{yz}-bands since the d_{xy}-orbital π-hybridizes with the $2p$-orbitals of all four neighboring in-plane oxygen ions, while the other two t_{2g}-orbitals

primarily hybridize with only two in-plane $2p$ oxygen orbitals. The Fermi surface of Sr_2RuO_4 consists of three cylindrical sheets, labeled α, β, and γ. The γ sheet has essentially d_{xy} character and is highly two-dimensional whereas the other two sheets have a mixed d_{xz}/d_{yz} character. The shape and volume of the calculated Fermi surface sheets is in rather good agreement with the ones determined experimentally by de Haas van Alphen experiments [7, 8], angle dependent magnetoresistance oscillations [9] as well as angle resolved photoemission spectroscopy (ARPES) [10]. However, there are several discrepancies between the LDA calculations and the experimental data concerning the effective mass of the electrons and details of the Fermi surface topography (crossing of Fermi sheets, c-axis dispersion). It had been shown recently, that some of these problems can be overcome by the inclusion of the spin-orbit coupling into the LDA calculation [11]. This clearly demonstrates that spin-orbit coupling plays an important role in the ruthenates. Thus, in contrast to most $3d$ transition metal oxides it cannot be neglected or treated as a small perturbation.

1.3 Exchange Interactions

The electronic structure of ruthenates and ruthenocuprates can be qualitatively understood within the crystal field theory, where the Coulomb interactions between the $4d$ electrons are not taken into account. However, these electronic interactions are responsible for the interactions between the spins of magnetic ions and therefore cause magnetism and related phenomena. In the following section, some of the various processes arising from the Coulomb repulsion are discussed.

1.3.1 Direct Exchange Interaction

The Coulomb interaction between two electrons with wave functions $\Psi(r_1)$ and $\Psi(r_2)$, located at r_1 and r_2, is expressed by the following Hamiltonian [2, 12]

$$H = \frac{1}{2}\int \Psi^\dagger(r_1)\Psi^\dagger(r_2)\frac{e^2}{|r_1 - r_2|}\Psi(r_1)\Psi(r_2)d\tau_1 d\tau_2, \tag{1.10}$$

where the integral runs over the spatial variables. The second quantized wave function $\Psi(r)$ can be written in terms of orthogonal states

$$\Psi(r) = \sum_{n,m,\sigma} c_{nm\sigma}\psi_{nm}\phi_\sigma, \tag{1.11}$$

where ψ_{nm} and ϕ_σ are the spatial and the spin wave functions and n, m and σ denote the ionic site, the orbital and the spin quantum numbers of an electron, respectively. Substituting this expression into Equation 1.10 and integrating over the spatial part gives

$$H = \frac{1}{2}\sum_{n,m,\sigma}\left\langle n_1 m_1, n_2 m_2 \left| \frac{e^2}{|r_1 - r_2|} \right| n_3 m_3, n_4 m_4 \right\rangle c^\dagger_{n_1 m_1 \sigma_1} c^\dagger_{n_2 m_2 \sigma_2} c_{n_3 m_3 \sigma_2} c_{n_4 m_4 \sigma_1}.$$

(1.12)

Here, $c^{\dagger}_{nm\sigma}$ and $c_{nm\sigma}$ are Fermi operators, which create and annihilate an electron. If all n are equal, the Hamilton operator describes the Coulomb repulsion of electrons belonging to the same magnetic ion. This case represents the well known Hund's coupling. Considering two electrons located at different ions ($n_1 = n_3$ and $n_2 = n_4$ or $n_1 = n_4$ and $n_2 = n_3$) each having a single orbital, the Hamiltonian can be rewritten as

$$\begin{aligned} H &= \frac{1}{2}\left\langle n_1, n_2 \left| \frac{e^2}{|r_1 - r_2|} \right| n_1, n_2 \right\rangle \sum_{\sigma_1,\sigma_2} c^{\dagger}_{n_1\sigma_1} c_{n_1\sigma_1} c^{\dagger}_{n_2 n_2 \sigma_2} c_{n_2\sigma_2} \\ &\quad -\frac{1}{2}\left\langle n_1, n_2 \left| \frac{e^2}{|r_1 - r_2|} \right| n_1, n_2 \right\rangle \sum_{\sigma_1,\sigma_2} c^{\dagger}_{n_1\sigma_1} c_{n_1\sigma_2} c^{\dagger}_{n_2 n_2 \sigma_2} c_{n_2\sigma_1}. \end{aligned} \tag{1.13}$$

The first term represents the usual Coulomb interaction between two electrons localized at sites n_1 and n_2 whereas the second term describes the exchange interaction. Introducing the following spin and number operators

$$S_{nz} = \frac{1}{2}\left(c^{\dagger}_{n\uparrow} c_{n\uparrow} - c^{\dagger}_{n\downarrow} c_{n\downarrow}\right) \tag{1.14}$$

$$S_{n+} = S_{nx} + iS_{nx} = c^{\dagger}_{n\uparrow} c_{n\downarrow} \tag{1.15}$$

$$S_{n-} = S_{nx} - iS_{nx} = c^{\dagger}_{n\downarrow} c_{n\uparrow} \tag{1.16}$$

$$n_n = n_{n\uparrow} + n_{n\downarrow} = c^{\dagger}_{n\uparrow} c_{n\uparrow} + c^{\dagger}_{n\downarrow} c_{n\downarrow} \tag{1.17}$$

and rewriting the Hamiltonian gives

$$H = K_{n_1 n_2} n_{n_1} n_{n_2} - 2J_{n_1 n_2}\left(\boldsymbol{S}_{n_1} \cdot \boldsymbol{S}_{n_2} + \frac{1}{4} n_{n_1} n_{n_2}\right), \tag{1.18}$$

where $K_{n_1 n_2}$ and $J_{n_1 n_2}$ denote the Coulomb and the exchange integral, respectively. The exchange interaction in the second term is called direct exchange interaction. It is responsible for ferromagnetic interactions, since the total energy is lowest for electrons with parallel spins.

1.3.2 Hubbard Model and Superexchange Interaction

The direct exchange interaction arises from the Coulomb repulsion in a localized electron system. Similar, but much stronger spin interactions can be deduced by considering the one-band Hubbard model in second order perturbation theory. This model describes two competing effects: The kinetic energy tends to delocalize the electrons into itinerant states leading to a metallic behavior whereas the Coulomb interaction between electrons wants to localize the electrons at the sites driving

the system towards an insulating state, which is usually antiferromagnetic. The Hubbard model can be written as [13]

$$H = -t \sum_{n_1,n_2,\sigma} \left(c^{\dagger}_{n_1\sigma} c_{n_2\sigma} + c^{\dagger}_{n_2\sigma} c_{n_1\sigma} \right) + U \sum_{n} n_{n\uparrow} n_{n\downarrow}, \tag{1.19}$$

where each ion is assumed to have a single orbital. The first term with the hopping integral t describes the electron transfer to a neighboring site without changing its spin direction. The second term represents the Coulomb interaction between two electrons located at the same site with opposite spins. The Coulomb integral U is given by

$$U = \int |\Psi_n(r_1)|^2 \frac{e^2}{|r_1 - r_2|} |\Psi_n(r_2)|^2 \, d\tau_1 d\tau_2. \tag{1.20}$$

The transport behavior is then determined by the ratio of U and t. For $\frac{U}{t} \to 0$, the electrons are delocalized and the system is metallic. In the opposite case, $\frac{U}{t} \to \infty$, the electrons are strongly localized at their sites and the material is an insulator. By changing the ratio of the two parameters a metal-insulator transition is expected, which is well known as Mott transition.
Starting from a Mott insulating state, the hopping integral t can be treated as a perturbation, which gives rise to second order processes which are shown in Figure 1.4. Due to the Pauli exclusion principle the intermediate state must have an antiparallel spin alignment and its energy is by U larger than the ground state energy. There are two possible final states depending on which electron goes to which ion. The second order processes are described by

$$H' = -\sum_{n_1,n_2} \sum_{\sigma_1,\sigma_2} \frac{2t^2}{U} c^{\dagger}_{n_1\sigma_2} c_{n_2\sigma_2} c^{\dagger}_{n_2\sigma_1} c_{n_1\sigma_1} \tag{1.21}$$

Using the spin operators introduced in the previous section and performing the summation over the spin part of Equation 1.21 gives

$$H' = \sum_{n_1,n_2} \frac{4t^2}{U} \left(\boldsymbol{S}_i \cdot \boldsymbol{S}_j - \frac{1}{4} n_{n_1} n_{n_2} \right). \tag{1.22}$$

In the half filled case $n_{n_1} = n_{n_2} = 1$, where each site is occupied by one electron, the energy is zero for a parallel, ferromagnetic spin configuration. This reflects the fact that electron hopping is not allowed if the electrons have a parallel spin. Due to the motions of the electrons, an antiparallel spin alignment is energetically favoured resulting in an antiferromagnetic insulating ground state. In ruthenates, as in other transition metal oxides, this antiferromagnetic interaction is mediated by the oxygen ions, located between neighboring ruthenium ions, and is therefore called superexchange interaction.

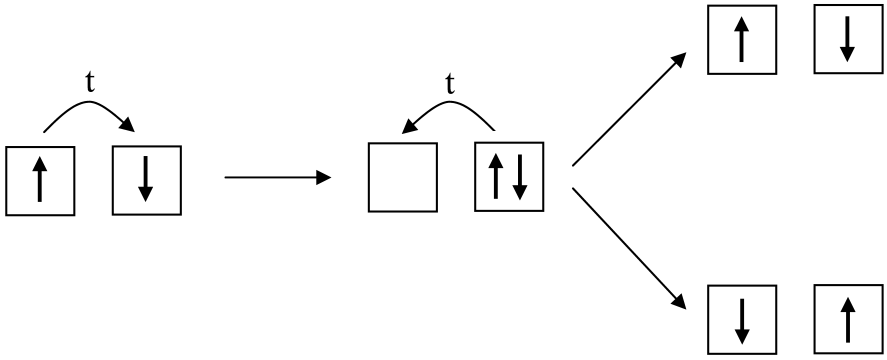

Figure 1.4: The process of superexchange interaction: An electron jumps to a neighboring site forming an intermediate state with an antiparallel spin configuration. Depending on the subsequent hopping process there are two possible final states.

1.4 Orbital Degeneracy and Orbital Order

In the previous section the single-orbital Hubbard model has been discussed, which gives rise to an antiferromagnetic insulating ground state, observed in various ruthenium oxides. However, due to the degeneracy of the t_{2g} orbitals most ruthenates also have an orbital degree of freedom which is responsible for additional, interesting phenomena. In these systems, the sign and magnitude of the superexchange interaction depends on the orbital occupation, which determines the degree of overlap of the participating states.
For simplicity, we consider two ions each with a twofold orbital degeneracy. The orbitals are denoted by φ_a and φ_b and the corresponding electron creation operators are $c_{ja\sigma}$ and $c_{jb\sigma}$, respectively, where $j = 1, 2$ denotes the ionic site and σ its spin. If electron hopping does not mix the orbital states, the one-electron part of the Hamiltonian is given by [14]

$$H_{hop} = -t_a \sum_{\sigma} \left(c^{\dagger}_{1a\sigma} c_{2a\sigma} + c^{\dagger}_{2a\sigma} c_{1a\sigma} \right) - t_b \sum_{\sigma} \left(c^{\dagger}_{1b\sigma} c_{2b\sigma} + c^{\dagger}_{2b\sigma} c_{1b\sigma} \right), \qquad (1.23)$$

where the hopping integrals t_a and t_b depend on the nature of the particular orbital. When an ionic site is occupied by two electrons, Coulomb energy has to be paid, which depends on whether the electrons share the same orbital or different ones. The corresponding Coulomb integrals are U_a, U_b and U_{ab}, where the interorbital Coulomb integral U_{ab} is expected to be smaller than the intraorbital terms U_a and U_b. In addition, two electrons on the same site, but in different orbitals can either form a spin singlet or a spin triplet. According to Hund's first rule the spin triplet, a ferromagentic state, is energetically favored. Denoting the Hund's coupling constant

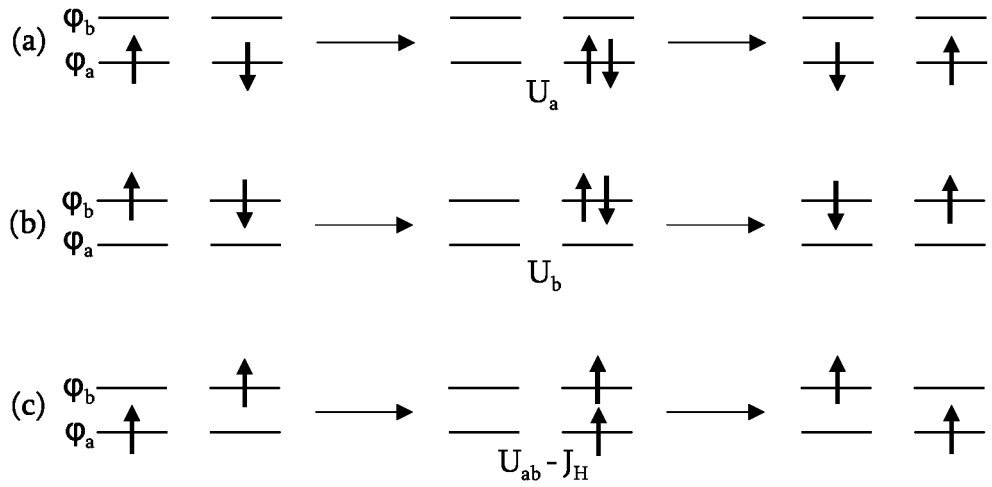

Figure 1.5: Schematic illustration of superexchange processes in a system consisting of two ions each with a twofold orbital degeneracy. The energies of the intermediate states of processes (a), (b) and (c) are U_a, U_b, $U_{ab} - J_H$, respectively.

with J_H, the interaction terms are summarized by

$$\begin{aligned} H_{int} &= U_a \sum_j n_{ja\uparrow} n_{ja\downarrow} + U_b \sum_j n_{jb\uparrow} n_{jb\downarrow} + U_{ab} \sum_j \sum_{\sigma\sigma'} n_{ja\sigma} n_{jb\sigma'} \\ &\quad -2J_H \sum_j \left(\boldsymbol{S}_{ja} \cdot \boldsymbol{S}_{jb} + \frac{1}{4} \right), \end{aligned} \tag{1.24}$$

where the spin and number operators introduced in the previous section have been used. The full Hamiltonian of the system is then given by

$$H = H_{hop} + H_{int}. \tag{1.25}$$

In the following, the hopping integrals t_a and t_b are assumed to be smaller than the intra- and interorbital Coulomb integrals and the Hund's coupling constant. Therefore, the hopping processes can be treated as a perturbation giving rise to superexchange interactions, which eventually determine the ground state of the system. Considering two electrons in the system, there are 16 low lying energy states arranged in four singlets and four triplets. Some of the possible superexchange processes in this system are shown in Figure 1.5. If the electrons at the two sites have an antiparallel spin (singlet state) and either occupy the orbital φ_a or orbital φ_b, hopping between the sites is allowed (Fig. 1.5a,b) . In this case the resulting interaction is antiferromagnetic and the kinetic exchange energy is given by $E_{singlet,a} \approx -\frac{4t_a^2}{U_a}$ and $E_{singlet,b} \approx -\frac{4t_b^2}{U_b}$ respectively. If the electrons of neighboring sites are either located in orbital φ_a or orbital φ_b and have parallel spins (triplet state), electron hopping between the two sites is forbidden due to Pauli's exclusion principle and the kinetic exchange energy is zero $E_{triplet,a} = E_{triplet,b} = 0$. However, the situation

is different if the electrons have parallel spins, but occupy different orbitals at neighboring sites (Fig.1.5c). In this case, hopping from one site to the other is allowed and the resulting superexchange interaction is ferromagnetic. The lowest energy of such a triplet state is given by

$$E_{triplet,ab} \approx -\frac{(t_a + t_b)^2}{U_{ab} - J_H}, \tag{1.26}$$

which is lower than those of the singlet states due to the smaller energy denominator. Hence, in contrast to the single-orbital Hubbard model which leads to an antiferromagnetic ground state, the orbital degeneracy gives rise to a ferromagnetic ground state due to the intraatomic Hund's coupling.
In addition, it is obvious that the orbital occupation plays a key role in the determination of the ground state. In general, ferromagnetism occurs if the orbital occupation varies between sites (antiferroorbital order), whereas a system exhibits antiferromagnetism if the orbital configuration is the same at every site (ferroorbital order). These relations are known as the Goodenough-Kanamori rules [15, 16].

1.5 Magnetic Anisotropy

The exchange interactions discussed in the last two sections are responsible for the arrangement of neighboring spins but they do not determine the direction of the magnetic moments. The coupling of the spins to the crystal environment results from the spin-orbit interaction, since the orbitals are sensitive to the lattice and hence cause magnetic anisotropy. The spin-orbit coupling in ruthenates is quite strong compared to other transition metal oxides due to the large atomic number of Ru.

1.5.1 Single Ion Anisotropy

Many antiferromagnetic ruthenates show single ion anisotropy due to the deformation of the RuO_6 octahedron, which lifts the degeneracy of the t_{2g} orbitals and therefore determines the easy axis of the magnetic moment by the spin orbit coupling. The Hamiltonian of the spin-orbit coupling is given by

$$H_{so} = \lambda \sum_i \mathbf{L}_i \cdot \mathbf{S}_i, \tag{1.27}$$

where λ is the coupling constant. The sum runs over all $4d$ electrons of the ruthenium ion. $\mathbf{L}_i$ and $\mathbf{S}_i$ denote the orbital angular momentum and spin momentum, respectively. In second order perturbation theory, this Hamiltonian gives rise to the following single ion anisotropy [2]

$$H_A = -\left(\frac{\lambda}{2}\right)^2 \sum_\nu A^\nu (S_\nu)^2, \tag{1.28}$$

where $\nu = x, y, z$ denotes the axes of the octahedron. The coefficients A^ν are functions of the energies of the $4d$ orbitals. Since these are nondegenerate, the three coefficients have different magnitudes and a particular spin direction is energetically favored. This direction then corresponds to the magnetic easy axis.

1.5.2 Anisotropic Exchange Interactions

Antiferromagnets with low crystal symmetry sometimes exhibit weak ferromagnetism which results from antisymmetric interactions. The existence of such interactions was first shown by Dzyaloshinski based on a symmetry analysis [17]. Later, their microscopic origin was discussed by Moriya in terms of the superexchange mechanism, taking into account the spin-orbit coupling [18]. In second order perturbation theory, this leads to the following Hamiltonian

$$H = \sum_{ij} J_{ij} \boldsymbol{S}_i \cdot \boldsymbol{S}_j + \sum_{ij} \boldsymbol{S}_i \Gamma_{ij} \boldsymbol{S}_j + \sum_{ij} \boldsymbol{D}_{ij} \cdot (\boldsymbol{S}_i \times \boldsymbol{S}_j) \,, \tag{1.29}$$

The first term denotes the isotropic superexchange interaction. The second term describes the symmetric anisotropic exchange interaction. It gives rise to a similar expression as the usual magnetic dipole interaction and is therefore termed pseudo-dipole interaction. The last term is the antisymmetric anisotropic exchange interaction, which is called Dzyaloshinski-Moriya interaction. The coupling constant $\boldsymbol{D}_{ij}$ vanishes when the the crystal field has inversion symmetry with respect to the center between the magnetic ions. This is usually not satisfied for low crystal symmetries. In this case, the Dzyaloshinski-Moriya interaction leads to a small canting of the sublattice spins, which are initially aligned antiparallel due to the superexchange interaction, and induces a weak ferromagnetic moment perpendicular to the spin axis of the antiferromagnet. Assuming two sublattices with magnetizations $\boldsymbol{M}_A$ and $\boldsymbol{M}_B$ with the canting angle $\theta = \frac{1}{2} \tan^{-1} \frac{|\boldsymbol{D}_{ij}|}{J}$, as schematically shown in Figure 1.6, the energy gain resulting from the Dzyaloshinski-Moriya interaction is calculated as

$$\boldsymbol{D} \left(\boldsymbol{M}_A \times \boldsymbol{M}_B \right) = - \left| \boldsymbol{D} \right| \left| \boldsymbol{M} \right|^2 \sin 2\theta \approx - \frac{\left| \boldsymbol{D} \right|^2}{J} \left| \boldsymbol{M} \right|^2 . \tag{1.30}$$

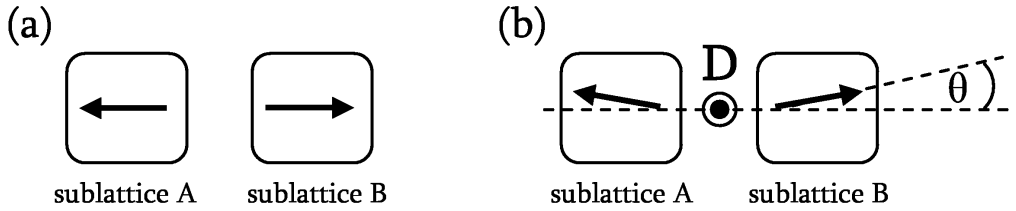

Figure 1.6: Weak ferromagnetism induced by the Dzyaloshinski-Moriya interaction: Due to the canting of the spins of the sublattices, which are initially aligned antiferromagnetically (a), weak ferromagnetism perpendicular to the antiferromagnetic axis is created (b).

1.6 Superconductivity

The phenomenon of superconductivity, which is characterized by zero electrical resistance and perfect diamagnetism below the superconducting transition temperature T_c, was first discovered in mercury (Hg) in 1911 by H. Kamerlingh. In the following decades, superconductivity was observed in various metals and alloys including lead (Pb), niobium (Nb) and Nb_3Ge. These conventional superconductors are well described within the framework of BCS theory. However, their transition temperatures are quite low, making technical applications difficult. The discovery of superconductivity in $La_{2-x}Ba_xCuO_4$ in 1986 by G. Bednorz and K. A. Müller [19] established the era of high temperature cuprate superconductors, which are characterized by much higher transition temperatures than those of conventional superconductors. The class of cuprate superconductors differ fundamentally from conventional superconductors, including the symmetry of the pairing state and the underlying pairing mechanism [20].

1.6.1 Conventional Superconductors and BCS Theory

The physics of conventional superconductors is well described by the BCS theory suggested by Bardeen, Cooper and Schrieffer in 1957 [21]. This microscopic theory is consistent with the previously proposed macroscopic theory of Landau and Ginzburg. According to BCS theory, a weak attractive interaction between the electrons leads to the formation of bound electron pairs, called Cooper pairs. This weak attractive interaction between the electrons originates from the electron-phonon interaction. This can be understood as follows: As an electron moves through the crystal, it creates a small lattice distortion by attracting the neighboring positive ions. A second electron is then attracted by the excess of positive charge, which results in an effective attraction between the two electrons mediated by the distortion of the lattice. If this attraction is strong enough to overcome the repulsive Coulomb interaction between the electrons, the net interaction is attractive and Cooper pairs are formed. The Cooper pairs then undergo Bose condensation into a single quantum state and carry the supercurrent without losses. For conventional superconductors, the electrons of a Cooper pair have opposite spin giving rise to a total spin of $S = 0$. The order parameter of the superconducting state is represented by the complex order parameter Φ which is zero above the superconducting transition temperature and non-zero in the superconducting state. For conventional superconductors, the phase of the order parameter is constant, whereas its magnitude, the superconducting energy gap, might slightly depend on the position on the Fermi surface and thus exhibit some anisotropy. Since conventional superconductors only break gauge symmetry at the superconducting transition temperature, they are called s-wave superconductors.

1.6.2 High Temperature Superconductors

High T_c cuprate superconductors are also characterized by a singlet pairing state, however, the order parameter has d-wave symmetry. This means that the order parameter changes sign under a 90° rotation and that there are points on the Fermi surface where the superconducting gap vanishes completely.
The cuprate superconductors are quasi two-dimensional systems which have a layered perovskite structure consisting of CuO_2 planes that are weakly coupled to each other. Superconductivity is induced by doping the Mott insulating parent compounds. In Mott insulators, the highest occupied band contains one electron per unit cell and electron motion hindered due to the Coulomb repulsion between the electrons which prevents the creation of a doubly occupied sites. Upon doping these systems, additional sites are created and electrical conduction is restored since the electrons can jump without any cost in Coulomb energy.
Due to superexchange interaction, many Mott insulators exhibit long range antiferromagnetic order. Anderson suggested that quantum fluctuations in two-dimensional spin $\frac{1}{2}$ systems are strong enough to destroy this antiferromagnetic order [22]. Instead, a spin liquid state is formed, which contains electron pairs with antiparallel spin. Since the motion of these singlet pairs is similar to the resonance of π bonds in benzene, this scenario is called "resonating valence bond" (RVB). In the undoped Mott insulator the singlet pairs are unable to move. This situation is changed upon doping, because the average occupancy is lowered, the electron pairs become mobile and superconductivity is induced. The transition temperature of the superconducting phase depends on the charge carrier concentration, thus the doping level. However, it has been shown by various experiments that a spin liquid state is not realized in undoped cuprates.
The pairing mechanism of charge carriers in cuprates is still controversial, although it is in general accepted that strong electron correlations play an important role. Among the most promising candidates responsible for the attractive interaction that leads to the formations of Cooper pairs are spin fluctuations. These might play a similar role as phonons in conventional superconductors: The spin of an electron might distort the nearby spins in such a way that it gives rise to an attractive interaction between the electrons and bind them into pairs. However, it is also possible that even more exotic excitations cause the attractive interaction. One of these ideas involves the formation of "stripes", which is based on the inhomogeneous ordering of spin and charge. In this scenario, a locally commensurate spin wave exist in the CuO_2 planes, whose phase jumps by 180° at domain walls, which are periodically ordered. As charge carriers (holes) are introduced by doping, they are not homogeneously distributed in the CuO_2 planes, but reside at the domain walls, forming charged stripes. The spin stripes have twice the periodicity of the charge stripes. The formation of these stripes is energetically favored because the transverse wandering of charge stripes cost less kinetic energy than the hopping a individual holes. Stripes of static and dynamic nature have indeed been observed in several superconducting cuprates [23, 24, 25]. However, the role of stripes for superconductivity

in cuprates is still under debate.
Ruthenocuprates with alternating CuO_2 and RuO_2 layers are very interesting examples of high T_c superconductors. In addition to superconductivity, which is established in the CuO_2 planes below 15-50 K, these materials exhibit long range magnetic order, which is related to the Ru sublattice and sets in well above the superconducting transition temperature. Due to the broad coexistence range of superconductivity and long range magnetic order, ruthenocuprates have attracted a lot of interest in the last years.

1.6.3 Triplet Superconductivity in Sr_2RuO_4

Superconductivity in Sr_2RuO_4 was first observed in 1994 by Y. Maeno and coworkers [26]. Soon after the discovery, it became clear that the superconducting state evolves from a strongly correlated metallic phase with Landau parameters very similar to those of the superfluid ^{3}He [26, 7]. In combination with the tendency towards ferromagnetism in Sr based ruthenates, this led to the speculation that Sr_2RuO_4 might be a spin triplet superconductor [27, 28]. First experimental evidence for an unconventional superconducting state came from a NMR study of the nuclear spin-lattice relaxation rate, which indicated the absence of a coherence peak at T_c [29], and from the fact that superconductivity is substantially suppressed by introducing non-magnetic impurities [30]. In the clean limit, Sr_2RuO_4 becomes superconducting below $T_c = 1.5$ K.
Direct evidence for a triplet superconductivity were provided by Knight shift measurements [31]. In accordance with the two-dimensional electronic structure of the Sr_2RuO_4, superconductivity is highly anisotropic: While the Knight shift cannot be determined for magnetic fields applied perpendicular to the RuO_2 planes due to the low critical field H_{c2}, it can be measured for magnetic fields applied parallel to the RuO_2 planes. For this field direction, the Knight shift remains constant down to very low temperatures. This indicates that the axis of the vector ordering parameter $\mathbf{d}(\mathbf{k})$ lies along c-axis of the crystal. Additional support for a p-wave superconducting state in Sr_2RuO_4 comes from muon spin rotation [32], which detects a spontaneously generated magnetic field as the sample is cooled below T_c. This result implies that the superconducting state breaks time reversal symmetry and suggests a triplet superconducting state with an order parameter of the form $\mathbf{d(k)} = \Delta_0\mathbf{z}(k_x \pm ik_y)$, which is consistent with the Knight shift data. For a quasi two-dimensional system, the corresponding superconducting energy gap is nodeless. However, the power law temperature dependence of the specific heat [33], the nuclear relaxation rate [34], and the thermal conductivity [35] indicate the presence of line nodes in the superconducting gap. This discrepancy might be understood in the following scenario, suggested by Zhitomirsky and Rice [36]: Due to the strong orbital character of the Fermi surface sheets (γ sheet based on d_{xy}-orbital, α and β sheets composed of hybridized d_{xy}- and d_{xy}-orbitals) the electronic structure of Sr_2RuO_4 might be regarded as consisting of two almost decoupled electronic subsystems. As a consequence, a nodeless gap might exist in the active band, whereas

line nodes develop in the passive bands by the interband proximity effect. Although this scenario reconciles various experimental results, there are many open questions that need to be addressed in order to get a better understanding of the spin triplet superconducting state in Sr_2RuO_4.

Chapter 2

X-ray diffraction

X-ray diffraction is the coherent scattering of x-rays by the atoms of a material. In the classical picture the oscillating electromagnetic field of the incident x-ray beam exerts a force on the atoms of the material causing them to oscillate and emit radiation with the same wavelength as the incident beam. Due to its large mass relative to that of an electron the nucleus of an atom is hardly put into oscillation and does not contribute to the scattering of an atom in a significant way. Hence, in a good approximation only the electrons of a material are responsible for coherent scattering.

2.1 Magnetic X-ray diffraction

For common samples, x-ray diffraction can be described by the kinematical theory. This theory is applied when the interaction between the incident and scattered x-ray beam is weak. This means that multiple scattering effects can be neglected and that the attenuation of the incident beam due to scattering events is not taken into account. These conditions are met for sufficiently small crystals. Within kinematical theory, the differential cross section for elastic x-ray diffraction from a small periodic crystal into the solid angle $d\Omega$ is given by

$$\frac{d\sigma}{d\Omega} = r_0^2 \left| \sum_m e^{i\mathbf{Q}\mathbf{R}_m} \sum_n e^{i\mathbf{Q}\mathbf{r}_n} D_n f_n(\mathbf{k}, \mathbf{k}', \hbar\omega) \right|^2 \tag{2.1}$$

where $r_0 = \frac{e^2}{mc^2}$ is the classical electron radius, $\mathbf{R}_m$ denotes the position of the unit cell, $\mathbf{r}_n$ is the position of an atom within the unit cell, $\mathbf{k}$ and $\mathbf{k}'$ are the incident and scattered wave vector of the photon with energy $\hbar\omega$, $\mathbf{Q}$ is the momentum transfer, D_n is the temperature dependent Debye-Waller factor and f_n represents the elastic scattering amplitude of the n-th atom in the unit cell.
The scattering amplitude of an atom is derived by considering the Hamiltonian for electrons in a quantized electromagnetic field within second order perturbation theory [37, 38]. Beside its dependence on the charge density, it is also sensitive to the magnetization of the atom which gives rise to magnetic scattering. Two limits of

magnetic scattering can be distinguished: Resonant scattering, where the incident photon energy is tuned close to an absorption edge of the atom and nonresonant scattering, where the photon energy is far from any absorption edge of the atom. Hence, the scattering amplitude can be written as [39]

$$f_n(\mathbf{k},\mathbf{k}',\hbar\omega) = f_n^{charge}(\mathbf{Q}) + f_n^{nonres}(\mathbf{Q},\mathbf{k},\mathbf{k}') + f_n^{res}(\mathbf{k},\mathbf{k}',\hbar\omega). \tag{2.2}$$

The first term is the well known Thomson scattering

$$f_n^{charge}(\mathbf{Q}) = \rho_n(\mathbf{Q})\ \boldsymbol{\epsilon}^{'}\cdot\boldsymbol{\epsilon}, \tag{2.3}$$

where $\rho_n(\mathbf{Q})$ is the Fourier transform of the charge density of the n-th atom and $\boldsymbol{\epsilon}$ and $\boldsymbol{\epsilon}^{'}$ denote the polarization of the incident and scattered photon, respectively. The second term of Equation 2.2 is the nonresonant scattering amplitude, which is expressed by

$$f_n^{nonres}(\mathbf{k},\mathbf{k}^{'},\hbar\omega) = -i\frac{\hbar\omega}{mc^2}\left(\frac{1}{2}\mathbf{L}_n(\mathbf{Q})\cdot\mathbf{B}_L + \mathbf{S}_n(\mathbf{Q})\cdot\mathbf{B}_S\right). \tag{2.4}$$

Here, $\mathbf{L}_n(\mathbf{Q})$ and $\mathbf{S}_n(\mathbf{Q})$ are the Fourier transforms of the orbital and spin magnetization densities, respectively. The vectors $\mathbf{B}_L$ and $\mathbf{B}_S$ contain the polarization dependence. They are given by

$$\mathbf{B}_L = 2(1-\hat{\boldsymbol{k}}\cdot\hat{\boldsymbol{k}}^{'})(\boldsymbol{\epsilon}^{'}\times\boldsymbol{\epsilon}) - (\hat{\boldsymbol{k}}\times\boldsymbol{\epsilon})(\hat{\boldsymbol{k}}\cdot\boldsymbol{\epsilon}^{'}) + (\hat{\boldsymbol{k}}^{'}\times\boldsymbol{\epsilon}^{'})(\hat{\boldsymbol{k}}^{'}\cdot\boldsymbol{\epsilon}), \tag{2.5}$$

$$\mathbf{B}_S = \boldsymbol{\epsilon}^{'}\times\boldsymbol{\epsilon} - (\hat{\boldsymbol{k}}\times\boldsymbol{\epsilon})(\hat{\boldsymbol{k}}\cdot\boldsymbol{\epsilon}^{'}) + (\hat{\boldsymbol{k}}^{'}\times\boldsymbol{\epsilon}^{'})(\hat{\boldsymbol{k}}^{'}\cdot\boldsymbol{\epsilon}) - (\hat{\boldsymbol{k}}^{'}\times\boldsymbol{\epsilon}^{'})\times(\hat{\boldsymbol{k}}\times\boldsymbol{\epsilon}), \tag{2.6}$$

where $\hat{\boldsymbol{k}}$ and $\hat{\boldsymbol{k}}^{'}$ denote the unit vectors along the incident and scattered wave vector. In contrast to neutron diffraction, the orbital and spin part of the nonresonant scattering amplitude exhibit a different polarization dependence which allows to separate them by a polarization analysis. However, due to the factor $\frac{\hbar\omega}{mc^2}$, nonresonant magnetic scattering is much smaller than the usual charge scattering. Hence, its observation is only feasible when the magnetization of the atom gives rise to additional Bragg reflections, which do not result from charge scattering. This is for instance the case for antiferromagnets.

The last term of (2.2) denotes the resonant scattering amplitude which is due to a second order scattering process. In a simple picture (Figure 2.1), this process corresponds to the absorption of an incident photon by an electron of the atom, the creation of an intermediate state with a short lifetime and the subsequent transition into the initial state, which is accompanied by the emission of a photon. The resonant scattering amplitude can be written as

$$\begin{aligned} f_n^{res}(\mathbf{k},\mathbf{k}^{'},\hbar\omega) &= \frac{1}{m}\sum_c \frac{E_a-E_c}{\hbar\omega}\frac{\left\langle a\left|O^{\dagger}_{\boldsymbol{\epsilon}'}(\mathbf{k}^{'})\right|c\right\rangle\left\langle c\left|O_{\boldsymbol{\epsilon}}(\mathbf{k})\right|a\right\rangle}{E_a-E_c+\hbar\omega-i\Gamma_c/2} \\ &\quad -\frac{1}{m}\sum_c \frac{E_a-E_c}{\hbar\omega}\frac{\left\langle a\left|O_{\boldsymbol{\epsilon}}(\mathbf{k})\right|c\right\rangle\left\langle c\left|O^{\dagger}_{\boldsymbol{\epsilon}'}(\mathbf{k}^{'})\right|a\right\rangle}{E_a-E_c-\hbar\omega} \end{aligned} \tag{2.7}$$

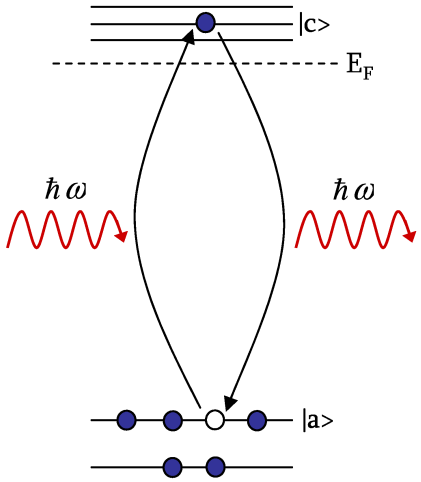

Figure 2.1: Schematic single electron picture of a resonant scattering process: An electron is excited from the initial state $|a\rangle$ into an unoccupied state $|c\rangle$ above the Fermi level by the absorption of a photon. Subsequently, the virtually excited electron decays emitting a photon.

where $|a\rangle$; E_a and $|c\rangle$; E_c denote the wave function and energy of the initial and intermediate states, respectively and Γ_c represents the inverse lifetime of the intermediate state. The operator $O_{\boldsymbol{\epsilon}}^{\beta}(\mathbf{k})$ is given by

$$O_{\boldsymbol{\epsilon}}(\mathbf{k}) = \sum_j e^{-i\mathbf{k}\mathbf{r}_j} \left(\boldsymbol{\epsilon} \cdot \mathbf{p}_j - i\hbar\boldsymbol{\epsilon}(\mathbf{k} \times \mathbf{s}_j)\right), \tag{2.8}$$

where $\mathbf{s}_j$ and $\mathbf{p}_j$ are the spin and momentum of the j-th electron of the atom. Resonant magnetic scattering is usually much stronger than nonresonant magnetic scattering. Therefore, it is also suitable for the investigation of weak magnetic and orbital phenomena.

2.2 Resonant X-ray diffraction

The resonant scattering amplitude contains both electric and magnetic multipole transitions. However, the magnetic mulitpole transitions are by a factor of $\frac{\hbar\omega}{mc^2}$ smaller than the electric ones and can therefore be neglected. If the atom has a spherical symmetric environment, but possesses a magnetic moment, the coherent resonant scattering amplitude of Equation 2.7 can be rewritten in terms of vector spherical harmonics $\mathbf{Y}_{LM}(\hat{\boldsymbol{k}})$ [40]

$$f_{n,EL}^{res}(\mathbf{k}, \mathbf{k}', \hbar\omega) = \frac{4\pi}{k} \sum_{M=-L}^{L} \left(\boldsymbol{\epsilon}'^{*} \cdot \mathbf{Y}_{LM}(\hat{\boldsymbol{k}}')\mathbf{Y}_{LM}(\hat{\boldsymbol{k}}) \cdot \boldsymbol{\epsilon}\right) F_{LM}(\omega), \tag{2.9}$$

where the factor F_{LM} determines the resonance strength which in turn depends on the atomic properties:

$$F_{LM}(\omega) = \sum_{a,c} \frac{p_a p_{ac} \Gamma_x(aMc; EL)}{2(E_c - E_a - \hbar\omega) - i\Gamma_c} \tag{2.10}$$

Here, p_a represents the probability to find the atom in the initial state $|a\rangle$ and p_{ac} denotes the probability for a transition from the initial state $|a\rangle$ to the intermediate state $|c\rangle$, which is determined by the overlap integral of the two states. Γ_x is the partial linewidth of the intermediate state due to pure electric multipole radiative decays.
For the evaluation of experiments, it is useful to express the resonant scattering amplitude with respect to the polarization of the incident and scattered beam. If we restrict ourselves to electric dipole ($E1$) transitions ($L = 1$, $M = 0, \pm 1$), which usually dominate the resonant magnetic scattering cross section, the resonant scattering amplitude can be written as [41]:

$$f_{n,E1}^{res} = \frac{3}{4k}\Big(\big(\boldsymbol{\epsilon}^{'} \cdot \boldsymbol{\epsilon}\big) F^{(0)} - i\big(\boldsymbol{\epsilon}^{'} \times \boldsymbol{\epsilon}\big)\boldsymbol{m}_n F^{(1)} + \big(\boldsymbol{\epsilon}^{'} \cdot \boldsymbol{m}_n\big)\big(\boldsymbol{\epsilon} \cdot \boldsymbol{m}_n\big) F^{(2)} \Big) \tag{2.11}$$

with

$$F^{(0)} = F_{11} + F_{1-1} \tag{2.12}$$

$$F^{(1)} = F_{11} - F_{1-1} \tag{2.13}$$

$$F^{(1)} = 2F_{10} - F_{11} - F_{1-1} \tag{2.14}$$

where $\boldsymbol{m}_n$ is the unit vector in the direction of the magnetic moment of the atom. The first term of Equation 2.11 is the anomalous dispersion term. Since it is independent of the magnetic moment, it contributes to the Bragg charge scattering. The second term of the resonant scattering amplitude is linear in the magnetic moment. It gives rise to first harmonic satellites in incommensurate antiferromagnets and is responsible for magnetic circular dichroism in ferromagnets. The third term of Equation 2.11 is quadratic in the magnetic moment and produces second harmonic satellites. It is related to linear magnetic dichroism which is usually much weaker than circular magnetic dichroism.

Considering the polarization dependence of the three terms, it is useful to express the polarization of a photon with respect to the scattering plane. Assuming linear polarization, the polarization of an incident/scattered photon is chosen to be either perpendicular (σ/σ') or parallel (π/π') to the diffraction plane as shown in Figure 2.2. Hence, four polarization channels can be distinguished: $\sigma\sigma'$, $\sigma\pi'$ $\pi\sigma'$ and $\pi\pi'$. Using this notation introduced by Bergevin and Brunel [42], the individual terms of the resonant scattering amplitude can be written as 2x2 matrices. This leads to the

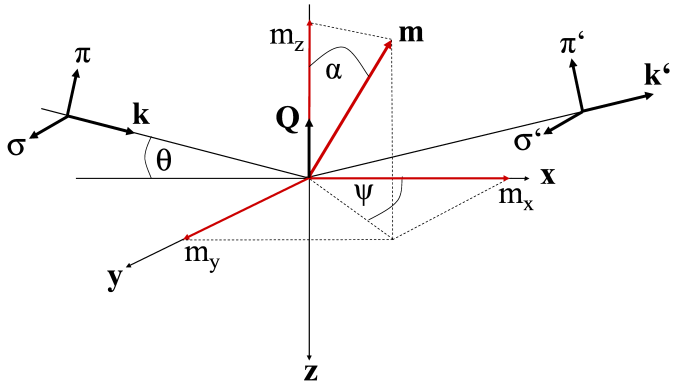

Figure 2.2: Schematic configuration of the scattering process. The sample is located at the origin of the reference system defined by the unit vectors **x**, **y**, **z**. The incident and scattered beam characterized by **k** and **k**′ are linearly polarized parallel (π/π') or perpendicular (σ/σ') to the diffraction plane. θ denotes the scattering angle, ψ is the azimuthal angle and α is the angle between the scattering vector **Q** and the magnetic moment **m**.

following expression for the resonant scattering amplitude [41]

$$\begin{aligned} f^{res}_{n,E1} &= \begin{pmatrix} f^{\sigma\sigma'} & f^{\pi\sigma'} \\ f^{\sigma\pi'} & f^{\pi\pi'} \end{pmatrix} \\ &= F^0 \begin{pmatrix} 1 & 0 \\ 0 & \cos 2\theta \end{pmatrix} - iF^1 \begin{pmatrix} 0 & m_x \cos\theta + m_z \sin\theta \\ -m_x \cos\theta + m_z \sin\theta & -m_y \sin 2\theta \end{pmatrix} \\ &\quad + F^2 \begin{pmatrix} m_y^2 & m_y(m_x \sin\theta - m_z \cos\theta) \\ m_y(m_x \sin\theta + m_z \cos\theta) & -\cos^2\theta(m_x^2 \tan^2\theta + m_z^2) \end{pmatrix}, \end{aligned} \tag{2.15}$$

where $f^{\mu\nu'}$ represents the scattering amplitude of a particular polarization channel, θ is the scattering angle and m_x, m_y, m_z denote the components of the magnetic moment along the axes of the reference system displayed in Figure 2.2. These are given by

$$\begin{aligned} m_x &= \sin\alpha \cos\psi \\ m_y &= \sin\alpha \sin\psi \\ m_z &= -\cos\alpha \end{aligned} \tag{2.16}$$

Here, α represents the angle between the scattering vector and the magnetic moment and ψ is the azimuthal angle. For $\psi = 0$, the magnetic moment lies in the scattering plane. The derived notation for the resonant scattering amplitude is very useful for experimental purposes, since it shows, which component of the magnetic moment is probed in a particular experimental configuration and how the magnetic signal changes as a function of azimuthal angle.

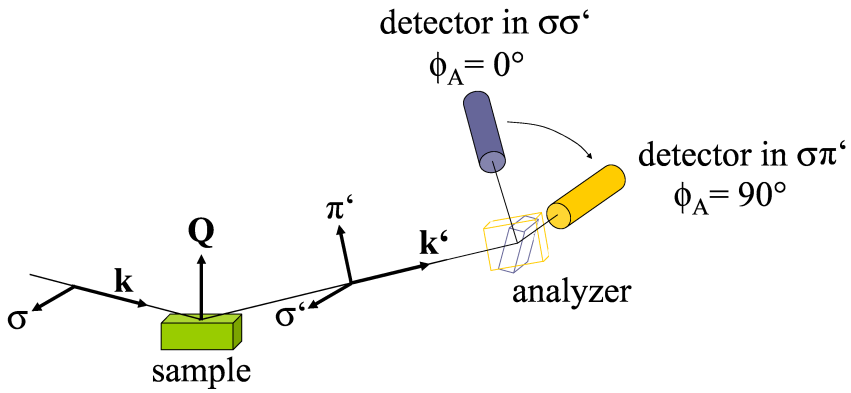

Figure 2.3: Experimental configuration for the polarization analysis of the scattered signal. The incident beam is linearly polarized perpendicular (σ) to the diffraction plane. The scattered beam in general contains both polarization components parallel (π') and perpendicular (σ') to the scattering plane, which are selected by the polarization analyzer.

2.2.1 Resonant X-ray interference scattering

Resonant x-ray diffraction is usually used to study materials, which exhibit antiferromagnetic or antiferroorbital order, since these allow the investigation of the magnetic and orbital phenomena at reflections, which are forbidden for Thomson scattering. In contrast, ferromagnetism and ferroorbital order manifest themselves as additional resonant intensity at the usual crystallographic Bragg reflections. Since Thomson scattering and magnetic/orbital scattering exhibit different polarization dependences, a polarization analysis needs to be performed to separate the contributions from each other.
For simplicity, we restrict the discussion to the situation with the incident polarization perpendicular (σ) to the diffraction plane as shown in Fig. 2.3. The scattered beam contains both polarization components. The signal in the $\sigma\sigma'$ channel is predominantly due to Thomson scattering, whereas the signal in the $\sigma\pi'$ channel results exclusively from magnetic/orbital scattering since charge scattering does not rotate the polarization of the diffracted signal. However, the magnetic/orbital signal is expected to be weak compared to the charge scattering signal of the $\sigma\sigma'$ channel. Therefore, it is difficult to directly observe the magnetic/orbital signal in an experiment. To enhance it, the authors of Refs. [43, 44] developed an interference technique where the magnetic/orbital signal is amplified by charge scattering. To this end, the polarization analyzer is rotated out of the $\sigma\pi'$-position ($\phi_A = 90°$) by some degrees ($\phi_A = 90° \pm \Delta$). The scattered intensity at an analyzer angle ϕ_A is given by

$$I(\phi_A) \propto \left| f^{\sigma\to\sigma'} \cos\phi_A - f^{\sigma\to\pi'} \sin\phi_A \right|^2 + \left| f^{\sigma\to\sigma'} \sin\phi_A + f^{\sigma\to\pi'} \cos\phi_A \right|^2 \cos^2 2\theta_A, \tag{2.17}$$

where $f^{\mu\nu'}$ represents the form factor of a particular polarization channel and θ_A is the scattering angle of the analyzer. This leads to the following interference term

$$I(\phi_A = 90^\circ - \Delta) - I(\phi_A = 90^\circ + \Delta) \propto 2Re(f^{\sigma\to\sigma'} f^{*\sigma\to\pi'}) \sin^2 2\theta_A \sin^2 2\Delta,$$

where the weak magnetic/orbital signal of the $\sigma\pi'$ channel is amplified by the Thomson scattering of $\sigma\sigma'$ channel. Since Thomson scattering does not exhibit any intensity change as a function of azimuth, the intensity variation of the interference term as a function of azimuthal angle is completely due to the magnetic/orbital signal.

Chapter 3

Experimental

3.1 Laboratory X-ray diffraction Setup

Prior to the synchrotron experiments, the crystals investigated in this work were characterized, and pre-aligned using the setup in the x-ray diffraction laboratory of Prof. Keimers department in the Max Planck Institute for Solid State Research. The availability of this setup was important for the success of the synchrotron experiments. On the one hand, it allows the identification of the best quality crystals, which saves valuable synchrotron beamtime. On the other hand, a good prealignment of the samples is necessary to measure an azimuthal angle dependence of a reflection, which is essential for the determination of the magnetic structure and orbital state, respectively. In principle, the pre-orientation of the crystals can also be done at the synchrotron beamline, however, this is time consuming and might be difficult, if the crystallographic axes of the sample are not known and a large area detector is not available.
The x-ray source in the laboratory is a RIGAKU molybdenum (Mo) rotating anode. Its characteristic emission lines Mo K_{α_1}, K_{α_2} and K_β correspond to energies of 17.479keV, 17.374keV and 19.608keV, respectively. The x-ray beam is monochromized and focused using two multilayer monochromators. The first focuses the beam vertically and the second one horizontally. Thereby, the K_α and K_β emission lines are spatially separated from each other due to their different scattering angles. Using a slit system, the K_β component is completely suppressed, and the x-ray beam focused onto the sample only contains the K_α components. The sample is mounted on a 4-circle HUBER diffractometer, which is used in a horizontal scattering geometry. For low temperature measurements, a closed cycle cryostat can be mounted on the diffractometer. With this setup, temperatures as low as 10K can be reached. The temperature is controlled using a Lakeshore 330 Temperature Controller.
The scattered signal is detected with a BRUKER SMART-1000 charged coupled device (CCD). Due to its large area, the CCD camera allows the simultaneous detection of several reflections. By rotating the sample, but keeping the detector at a fixed position, a large number of reflections can be detected within a short period.

Using the software program SMART, these reflections are used to determine the crystallographic axes of the sample and the corresponding lattice constants. To this end, the relative distances of the reflections in reciprocal space are compared with the expected ones for the particular space group and a least mean square fitting is performed. Once the crystallographic axes and lattice parameters are known, the crystal is precisely aligned along a particular direction using a scintillation detector, which is also used to determine the crystal quality and to obtain the precise values of the lattice constants.

3.2 Synchrotron Beamlines

The resonant x-ray diffraction experiments at the Ru L-absorption edges were carried out at beamline 4-ID-D of the Advanced Photon Source (APS) at the Argonne National Laboratory and at beamline KMC-1 of the Berliner Elektronenspeicherring-Gesellschaft für Synchrotronstrahlung (BESSY). Both beamlines are described in the following. Another resonant x-ray diffraction study was performed at the Ru K-absorption edge at beamline MagS of BESSY. Since the experimental configuration of this beamline is very similar to that of beamline 4-ID-D of the APS, it is not described in detail. High energy x-ray diffraction experiments in a magnetic field were carried out at beamline BW5 of the Hamburger Synchrotronstrahlungslabor (HASYLAB) at the Deutsches Elektronen Synchrotron (DESY).

3.2.1 Beamline 4-ID-D of the Advanced Photon Source

The beamline 4-ID-D of the APS operates in the hard x-ray regime. The undulator used at this beamline is a 72-pole undulator with a nominal gap of 11 mm, which allows an operation in the energy range between 3 keV and 50 keV. Special modification to the vacuum chamber of the undulator have been made to permit the closure of the gap down to 9.5 mm and hence the operation at energies as low as 2.5 keV, needed for the resonant x-ray experiments at the Ru L-absorption edges, lying at

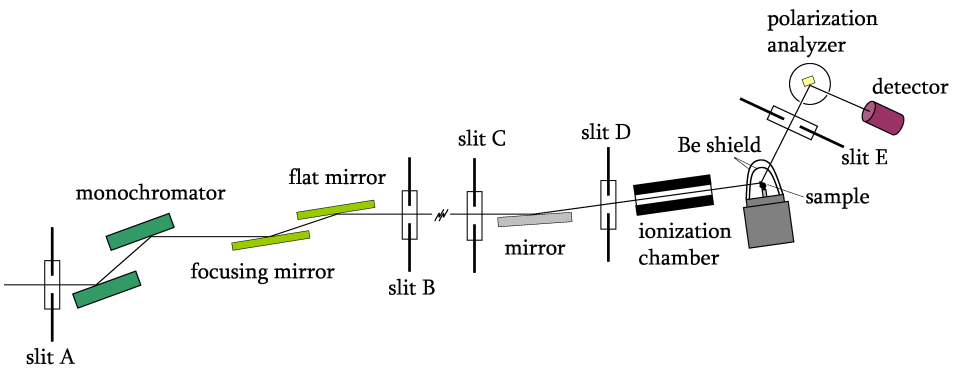

Figure 3.1: Schematic side view of the optics and the experimental configuration of beamline 4-ID-D at the APS.

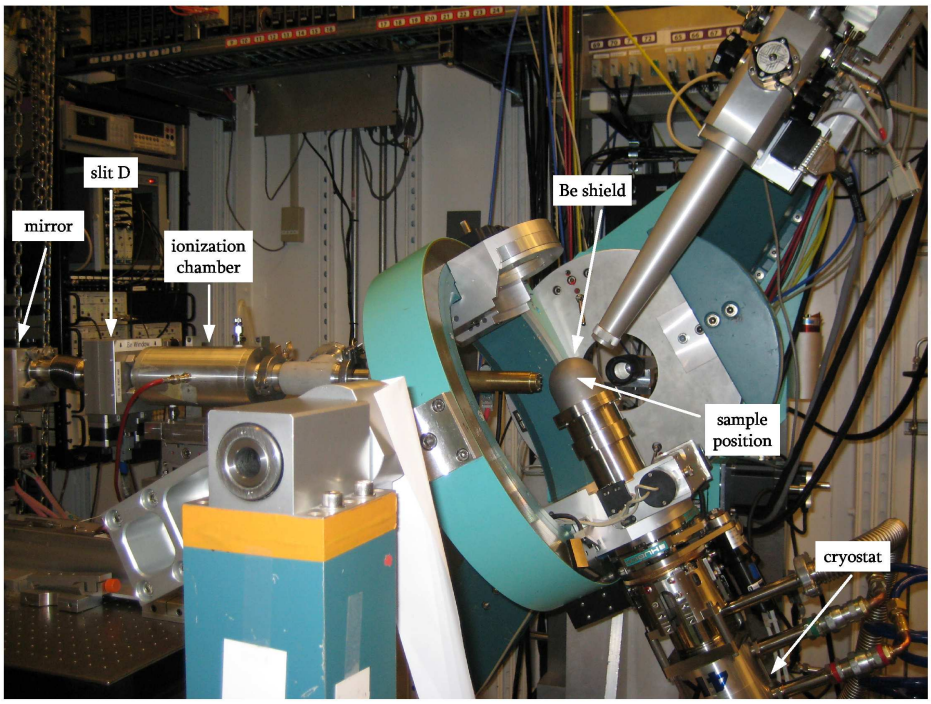

Figure 3.2: Photograph of the experimental setup in the experimental station of beamline 4-ID-D of the APS. The sample hidden beneath the Be dome is mounted on the the cryostat, which is attached to the 8-circle HUBER diffractometer.

2.968 keV and 2.838 keV, respectively.
A schematic view of the optics and the experimental configuration of the beamline is shown in Figure 3.1. The x-ray beam leaving the undulator is monochromized by a KOHZU double crystal monochromator using two Si (111) crystals. The monochromatic beam is focused by a toroidal SiO_2 mirror. To suppress higher harmonic components of the x-ray beam a Pd coated SiO_2 mirror, mounted behind the focusing mirror, and an additional, smaller SiO_2 mirror in the experimental station are used. An ionization chamber, mounted in front of the sample, monitors the intensity of the incident beam. In addition, several slit systems are used to reduce the background and to define the size and shape of the incident x-ray beam, which has a typical size of $200\,\mu m \times 100\,\mu m$ as it reaches the sample. The sample is mounted in the center of an 8-circle HUBER diffractometer, which is used in a vertical scattering geometry as shown in Figure 3.2. The scattered beam is detected by a Cyberstar NaI scintillation detector. This is mounted on the detector arm either directly behind the last slit, which is used to reduce the background mainly resulting from fluorescence, or behind the polarization analyzer. Due to the strong absorption of the x-ray beam below 3 keV, as few beryllium windows as possible are used and the flight path of the incident and diffracted beam is either kept under vacuum or helium atmosphere.
Since the incident x-ray beam is horizontally polarized, it has σ polarization according to the notation introduced in Chapter 2. The polarization of the diffracted beam

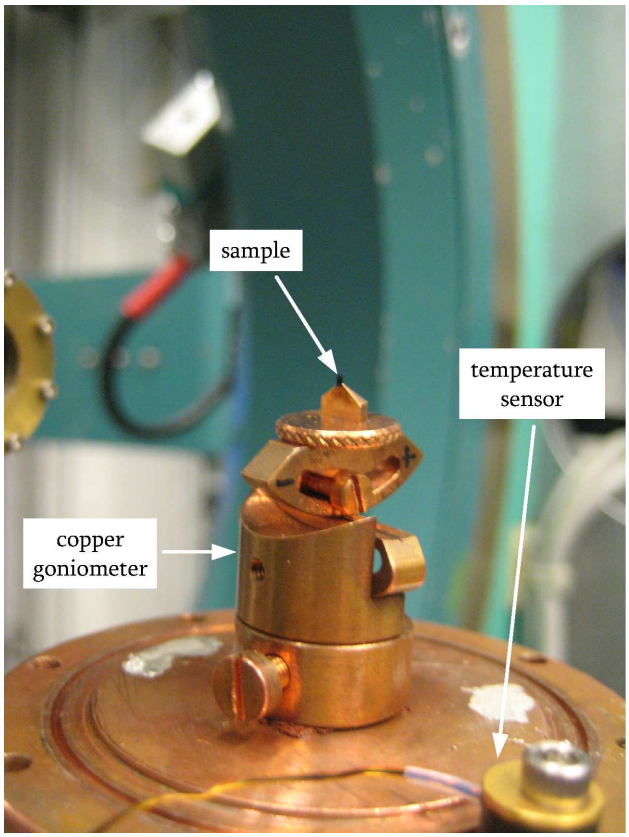

Figure 3.3: Photograph of the sample environment. The sample is mounted on a copper goniometer, which is screwed into the coldfinger of the cryostat. The temperature sensor is attached close to the sample.

can be studied using an in vacuum polarization analyzer which can be mounted between the last slit and the detector. In case of the Ru L-absorption edges, it consists of a Si (111) crystal, which gives a scattering angle of 41.8° and 44.2° at the L_2- and L_3-absorption edges, respectively. The polarization analyzer including the attached detector can be rotated around an axis parallel to the diffracted beam. Thus, the σ' component of the scattered signal is measured if the detector is parallel to the scattering plane and the π' component of the diffracted signal is collected if the detector is perpendicular the scattering plane. In addition, it is possible to measure the diffracted signal in a mixed polarization state, which is necessary to carry out interference scattering experiments. In this case, the detector is rotated to a position neither parallel nor perpendicular to the diffraction plane.

The sample is mounted on a copper goniometer head (Figure 3.3),which is attached to the coldfinger of a closed cycle cryostat capable of reaching temperatures between 4 K and 340 K. The cryostat is mounted on the motorized xyz-translation stage of the diffractometer. In order to cool the sample, two dome shaped beryllium shields are attached to the cryostat around the sample position. The outer beryllium shield with a thickness of 500 μm is needed to reach high vacuum, whereas the inner beryllium shield with a thickness of 200 μm reduces the thermal losses to the

sample environment. To improve the thermal coupling of the sample to the coldfinger of the cryostat, exchange gas (helium) can be used in the inner beryllium shield. Unfortunately, the absorption of the x-ray beam by the beryllium domes is quite strong. At the Ru L-absorption edges, the absorption caused by the shields leads to a total beam attenuation of more than two orders of magnitude. To avoid these strong absorption effects, it is possible to omit the inner beryllium dome. However, this is not feasible, if temperatures below 50 K are required.
Two Si-diodes are used as temperature sensors, which are connected to a Lakeshore 340 Temperature Controller. The first temperature sensor is mounted to the cryostat cold finger in the vicinity of the heater. Based on the temperature read by this control sensor, the heater output needed to stabilize a particular temperature is calculated using a PID algorithm. The second temperature senor is mounted as close as possible to the sample, as shown in Figure 3.3. The temperature measured by this sensor corresponds approximately to the sample temperature.

3.2.2 Beamline KMC-1 of BESSY

The bending magnet beamline KMC-1 of BESSY covers the energy range between 1.7 keV and 12 keV. A schematic top view of the optics and the experimental setup of the beamline is shown in Fig. 3.4. The x-ray beam produced by the bending magnet is focused by a toroidal mirror made of Si with a Pt coating. The focused beam is monochromized by a Oxford-Danfysik double crystal monochromator, which is equipped with three pairs of crystals: InSb, Si (111) and Si (422), which can be exchanged within a few minutes. For the resonant x-ray diffraction studies at the Ru L-absorption edges, the Si (111) crystals were used. To suppress higher order components of the x-ray beam, to attenuate the beam or to calibrate the energy three different filter sets with a thickness between 1 and 5 μm can be inserted into the beam path. An ionization chamber is used to monitor the incident intensity of the x-ray beam. The sample is located in the center of the ultrahigh vacuum (UHV) two-circle diffractometer designed by E. Weschke and E. Schierle from the

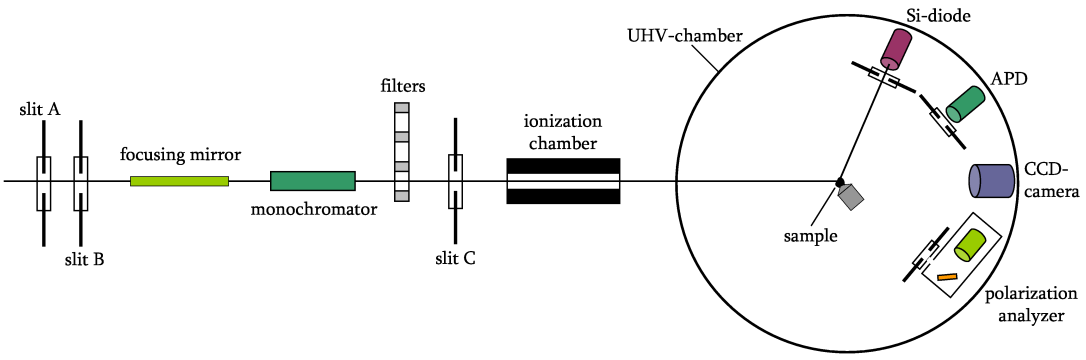

Figure 3.4: Schematic top view of the optics and the experimental configuration of the bending magnet beamline KMC-1 at BESSY.

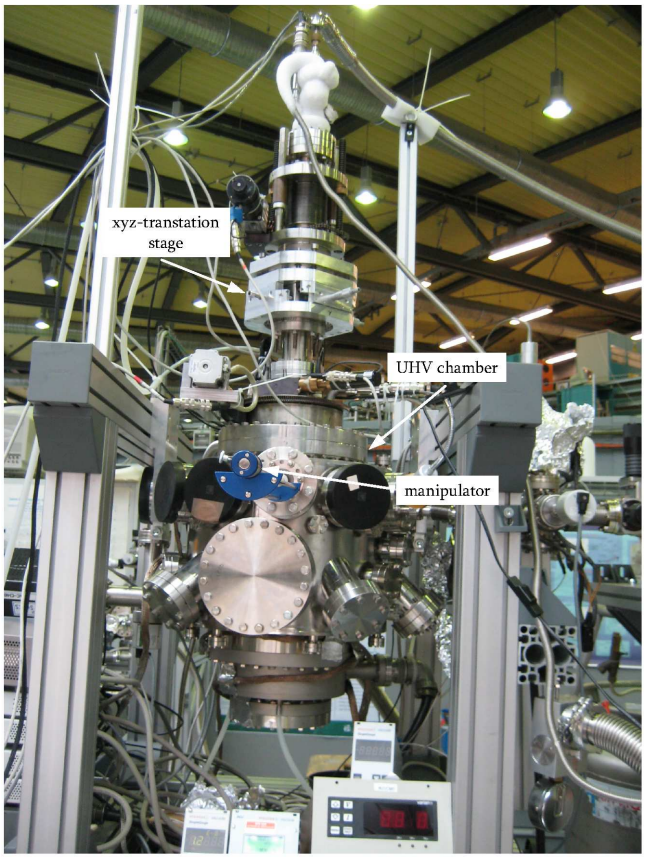

Figure 3.5: Photograph of the UHV two-circle diffractometer used at beamline KMC-1.

Freie Universität Berlin. This diffractometer, shown in Figure 3.5, is used in a horizontal scattering geometry. It allows the independent rotation of the sample and the detector within the full angular range of ± 180°.

Four different detectors are available for the detection of the diffracted signal: A CCD camera is used for the sample alignment, which saves a lot of time compared to the alignment procedure using a point detector. Since the sensitivity of the CCD camera is limited, it provides mainly qualitative information. Therefore, the scattered signal is either detected with a Si photo diode or an Oxford Danfysik avalanche photo diode (APD). The APD has a better signal to noise ratio due to the possibility to discriminate certain photon energies and the absence of electronic noise. Therefore, it is preferable to use the APD instead of the Si-diode, especially for the detection of small signals. On the other hand, the Si photo diode is optimized for operation in the soft x-ray regime, which allows to use it for fluorescence measurements. In addition, a polarization analyzer consisting of a Si (111) crystal can be used to study the polarization of the diffracted beam. The signal diffracted by the analyzer crystal is detected by a Si photo diode. Unfortunately, this diode cannot be rotated out of the diffraction plane. Thus, only the signal in the $\pi\sigma'$-channel can be measured. However, the $\pi\pi'$-signal can be calculated by subtracting the $\pi\sigma'$-signal from the total signal.

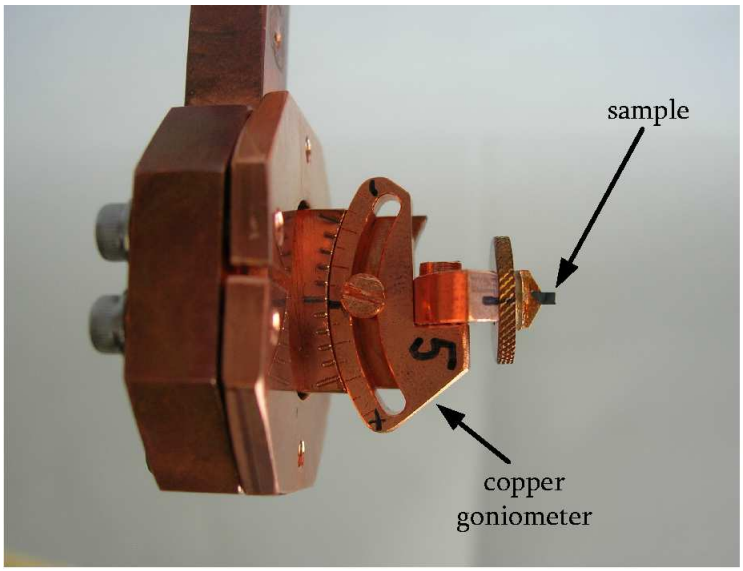

Figure 3.6: Photograph of the sample environment. The sample is mounted on a copper goniometer, which is attached to a copper lead attached to the coldfinger of the cryostat.

The sample is mounted on a small copper goniometer, as shown in Figure 3.6, which is attached to the coldfinger of the cryostat. Since it is not possible to tilt the sample, the prealignment of the sample has to be very precise. Otherwise the rotation of the goniometer would not correspond to a rotation around the scattering vector and an azimuthal angle dependence of the scattered signal could not be measured. For an azimuthal dependence of the diffracted signal, the goniometer is manually rotated using a manipulator attached to the UHV chamber.
Without further thermal shielding temperatures as low as 16 K can be reached with this setup. The temperature is monitored using a Lakeshore 330 temperature controller and two Si diodes as temperature sensors. The first of them is mounted close to the goniometer and measures the sample temperature, whereas the second is located at the coldfinger of the cryostat near the heater. The temperature read by the second sensor is used to control the heater output and stabilize the temperature.

3.2.3 Beamline BW5 of HASYLAB

The beamline BW5 of HASYLAB operates in the high energy x-ray regime. The wiggler used at this beamline has a critical energy of 26.5 keV and a minimum gap of 20 mm. To reduce the heat load on the optical elements, a 1.5 mm thick water cooled copper filter is used to absorb the low energy part of the spectrum produced by the wiggler. This allows the operation at energies between 60 keV and 200 keV. The experiments described in this thesis were carried out at a photon energy of 100 keV.
The experimental setup in the experimental station is shown in Figure 3.7. The beam enters the experimental hutch through a slit of variable size, which is kept under vacuum to minimize the ozone production and reduce the background radi-

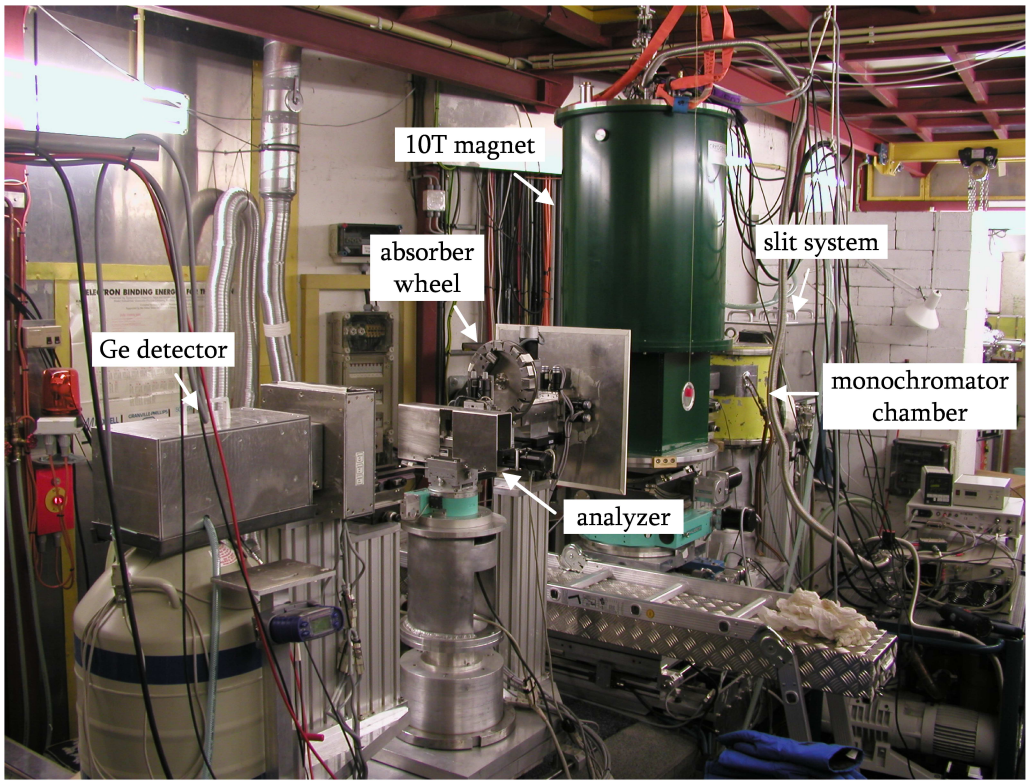

Figure 3.7: Experimental setup in the experimental station of beam line BW5 of HASYLAB.

ation. The beam is monochromized by a SiGe (111) gradient crystal located in a helium chamber. This monochromator allows a broad energy spectrum to pass and thereby assures a large incident beam intensity. The intensity of the incident beam is monitored by a Si-diode mounted behind the monochromator.
The sample is mounted in a Cryogenics superconducting magnet used in a horizontal scattering geometry. Horizontal magnetic fields up to 10 T, parallel as well as perpendicular to the scattering vector, can be applied with this setup. The magnet is mounted on the sample tower of the diffractometer consisting of a three independent circles. This allows a sample rotation of $\pm 180°$ and a sample tilt of $\pm 5°$.
An iron absorber wheel is located behind the magnet to attenuate the diffracted beam if necessary and another SiGe (111) gradient crystal is used as analyzer to minimize the background. The scattered intensity is detected by a Ge detector cooled with liquid nitrogen, which is mounted on the tower in the back of the diffractometer.

Chapter 4

Magnetic and Orbital Order in $Ca_3Ru_2O_7$

Layered perovskite ruthenates exhibit a wide variety of interesting phenomena due to the strong interplay of spin, charge, lattice and orbital degrees of freedom. The latter is particularly pronounced in bilayered $Ca_3Ru_2O_7$ which is extremely sensitive to small perturbations, such as uniaxial or hydrostatic pressure [45, 46, 47, 48], doping [49, 50, 51, 52] and external magnetic fields [53, 54, 55, 56], giving rise to a rich phase diagram (Figure 4.1). Since most of the phase transitions in the material have been attributed to the rearrangement of the magnetic and orbital structure, resonant x-ray diffraction is well suited for the investigation of this system because it probes magnetic and orbital ordering phenomena.

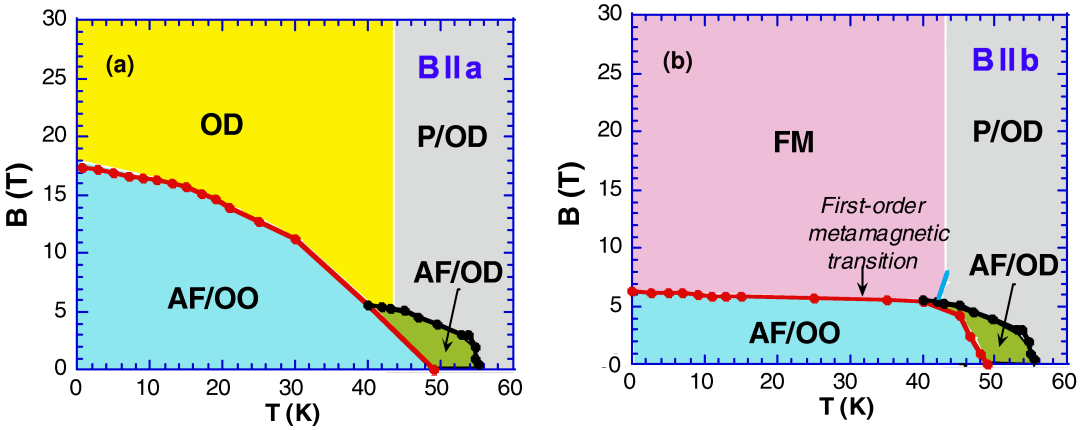

Figure 4.1: Phase diagram of $Ca_3Ru_2O_7$ with (a) $B \parallel a$ and (b) $B \parallel b$ [57](Axes labels have been changed to be consistent with the notation used in this work). Various phases arise as a function of magnetic field including ferromagnetic (FM), antiferromagnetic (AFM), paramagnetic (P), orbitally ordered (OO) and orbitally disordered (OD) states.

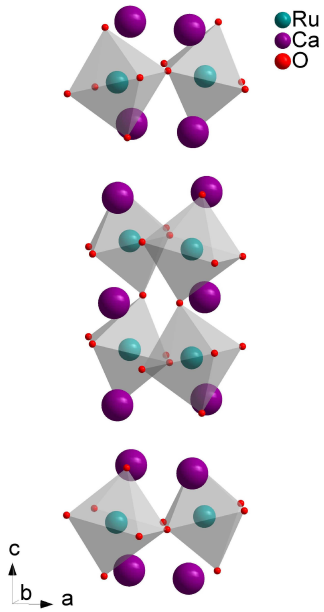

Figure 4.2: Crystal structure of $Ca_3Ru_2O_7$.

4.1 Properties of $Ca_3Ru_2O_7$

$Ca_3Ru_2O_7$ has a distorted orthorhombic symmetry and belongs to space group $Bb2_1m$ with room-temperature lattice parameters a =5.3781(2)Å, b =5.5227(2)Å and c =19.5872(8)Å [58]. As shown in Figure 4.2, it consists of RuO_2 bilayers with corner sharing RuO_6 octahedra which are rotated around the crystallographic c-axis and tilted with respect to the ab-plane. The tilts of the octahedra are mainly projected onto the ac-plane and only slightly affect the bc-plane.

The electronic structure of $Ca_3Ru_2O_7$ is closely related to its crystal structure. The ruthenium ions are in the formal valence state Ru^{4+}, which corresponds to the electron configuration $4d^4$. Due to the large e_g-t_{2g} crystal field splitting, which overcomes the Hund's coupling, all four valence electrons of the Ru^{4+} ions occupy the t_{2g}-orbitals and the material is in a low spin state with a total spin of S=1. Furthermore, the combined distortion, tilt and rotation of the RuO_6 octahedra remove the degeneracy of the t_{2g}-orbitals by lowering the energy of the d_{xy}-orbital with respect to the d_{xz}- and d_{yz}-orbitals as schematically shown in Figure 1.3 of Chapter 1.
The material is a paramagnetic metal at high temperatures and orders antiferromagnetically at $T_N = 56\,\mathrm{K}$, but initially remains metallic [59]. At $T_{MI} = 48\,\mathrm{K}$, it undergoes a second phase transition, which manifests itself in an abrupt resistivity increase along all three crystallographic axes as shown in Figure 4.3. However, whereas the resistivity along the c-axis continues to increase upon further cooling [59], it decreases again in the ab-plane below 30 K, indicating a quasi two dimensional metallic ground state [60, 61]. Despite this unconventional behavior, this transition is referred to as the metal-insulator transition in the following. While

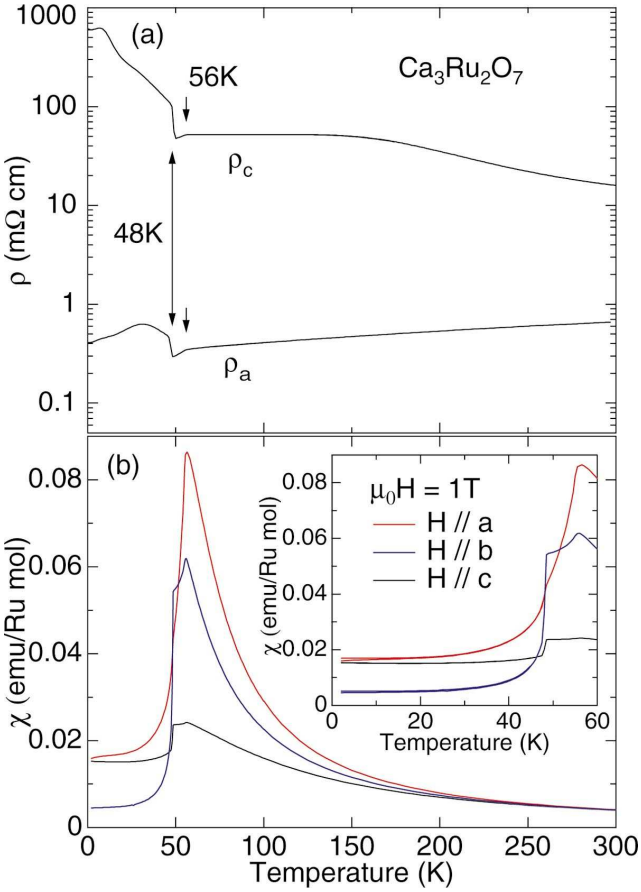

Figure 4.3: Temperature dependence of the resistivity (a) and the susceptibility (b) of $Ca_3Ru_2O_7$[60]. While the resistivity along the c-axis continues to increase below the metal-insulator transition at $T_{MI} = 48\,\mathrm{K}$, the resistivity in the ab-plane decreases again below 30 K, indicating a quasi two dimensional ground state. The susceptibility data clearly indicate an antiferromagnetic transition at $T_N = 56\,\mathrm{K}$ and a second anomaly at T_{MI}.

the space group is unaffected by the metal-insulator transition [58], all lattice constants show a step like change at this temperature (Figure 4.4) with an in-plane expansion [58] and a contraction along the c-axis [62] upon cooling below the transition. This observation bears some resemblance with the single layered compound Ca_2RuO_4, where the relative lattice parameter change at the metal-insulator transition amounts about 2% [63]. However, the observed change of less than 0.2% in $Ca_3Ru_2O_7$ is much smaller than in Ca_2RuO_4.

Various magnetization and susceptibility studies have been carried out on $Ca_3Ru_2O_7$ [53, 45, 64, 60]. The susceptibility along the a- and b-axis is displayed in Figure 4.3. It exhibits a typical Curie-Weiss like behavior in the paramagnetic phase above T_N that can be fitted by a positive Curie temperature for both axes suggesting ferromagnetic (FM) correlations in the RuO_2 planes [53, 60]. The steep decrease of the

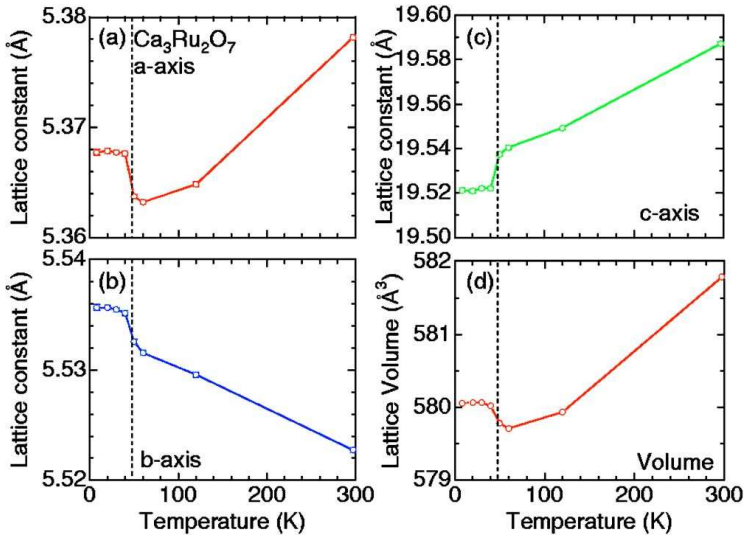

Figure 4.4: Temperature dependence of lattice parameters (a-c) and lattice volume (d) of $Ca_3Ru_2O_7$ determined by powder neutron diffraction [58].

susceptibility along both in-plane axes at T_N indicates the existence of long-range antiferromagnetic (AFM) order with the moments oriented in the *ab*-plane. Below T_{MI}, the susceptibility decreases along all three crystallographic directions and becomes almost temperature independent at low temperatures. Since the susceptibility is lowest along the *b*-axis in this temperature range, the magnetic moment is assumed to lie along the *b*-axis. Additional information about the magnetic structure of $Ca_3Ru_2O_7$ has been deduced from neutron powder diffraction [58]. These studies have proposed an A-type AFM magnetic structure consisting of ferromagnetic RuO_2 bilayers coupled antiferromagnetically along the *c*-axis. However, since only a single magnetic Bragg reflection has been detected in neutron diffraction, the magnetic structure assignment must regarded as tentative.

$Ca_3Ru_2O_7$ exhibits strong anisotropy effects as a function of an external magnetic field. For $\boldsymbol{B} \,||\, a$, the material remains antiferromagnetic at low temperatures and becomes paramagnetic above 17 T [53]. For $\boldsymbol{B} \,||\, b$ and low temperatures, the system undergoes a first order metamagnetic transition at 6 T. Although the phase above the metamagnetic transition is characterized by a large FM moment of $1.73\mu_B$/Ru, which is close to the saturation moment of $2\mu_B$/Ru expected for a $S = 1$ system [53], a significant spin canting alternating between neighboring bilayers has been revealed by a recent neutron diffraction study [65].

Figure 4.5 shows the *b*- and *c*-axis resistivity as a function of applied magnetic fields along all crystallographic axes. For $\boldsymbol{B} \,||\, b$, the resistivity along both axes decreases by about one order of magnitude at 6 T, which coincides with the metamagnetic transition. Interestingly, the resistivity drop is much more pronounced for $\boldsymbol{B} \,||\, a$ (magnetic hard axis), where the *c*-axis resistivity decreases rapidly by about three orders of magnitude above 15 T. Similar colossal magnetoresistance (CMR) effects have also been observed in various manganese compounds [66]. In agreement with

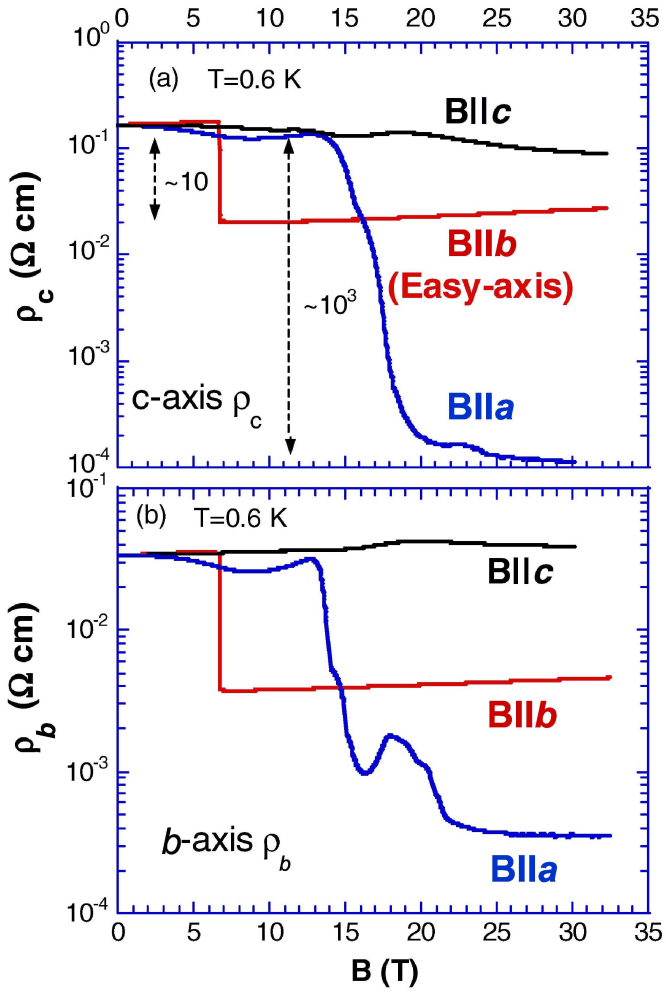

Figure 4.5: Magnetoresistance (a) ρ_c and (b) ρ_b of $Ca_3Ru_2O_7$ [57] (Axes labels have been changed to be consistent with the notation used in this work). The colossal magnetoresistance is most pronounced when the magnetic field is applied along the magnetic hard axis, where it decreases by three orders of magnitude.

the latter, the transition to a spin polarized state seems to be essential for CMR in $Ca_3Ru_2O_7$: For $\boldsymbol{B} \,||\, b$, the state above the metamagnetic transition is not completely spin polarized [65] while this is the case in the paramagnetic phase for $\boldsymbol{B} \,||\, a$ and high magnetic fields.

For $\boldsymbol{B} \,||\, c$, Shubnikov de Haas oscillations corresponding to very small cross sections of the Fermi surface have been reported for the a- and c-axis resistivity [45, 62, 67]. The large anisotropy effects observed in $Ca_3Ru_2O_7$ have been attributed to the strong interplay between spin, lattice and orbital degrees of freedom. The distortions of the RuO_6 octahedra play an important role in this context. Since the projections of octahedral tilts onto the ac-plane are larger than onto the bc-plane, the orbital overlap between states of neighboring Ru ions is different along all three crystallographic axes. Small changes in the octahedral tilts can then give rise to

qualitative changes of the properties. Due to this asymmetry, the coupling of a magnetic field to the system strongly depends on the field orientation causing the big anisotropy effects.
As already mentioned, the metal-insulator transition is accompanied by a resistivity increase, abrupt structural changes and anomalies in the magnetization. In addition, Raman scattering studies [68, 55, 69] revealed an opening of a charge gap of about 0.1 eV and a softening of the apical oxygen phonon mode at T_{MI}. The latter findings have been interpreted in terms of the onset of long-range orbital order at 48 K. This scenario is also supported by optical conductivity measurements [70] and angle-resolved photoemission spectroscopy (ARPES) [71]. Although no calculations have been made for $Ca_3Ru_2O_7$, orbital order has been predicted theoretically for the single layered compound Ca_2RuO_4, which exhibits similar distortions of the RuO_6 octahedra.
Based on LDA + U calculations, several groups have suggested the existence of an ferroorbital ordered (FO) state for Ca_2RuO_4, characterized by a uniform orbital occupation at every Ru site [72, 73, 3]. This result is easily understood considering the simple picture of the electronic structure discussed above. The d_{xy}-orbital has the lowest energy among the t_{2g}-orbitals and is therefore doubly occupied, while the d_{xz}- and d_{xy}-orbitals are occupied by a single electron, respectively.
Considering a three orbital Hubbard model together with lattice distortions, Hotta and Dagotto proposed an antiferro-orbital ordered state for Ca_2RuO_4 [74]. According to their model, the orbital occupation is different at nearest neighbor sites, as

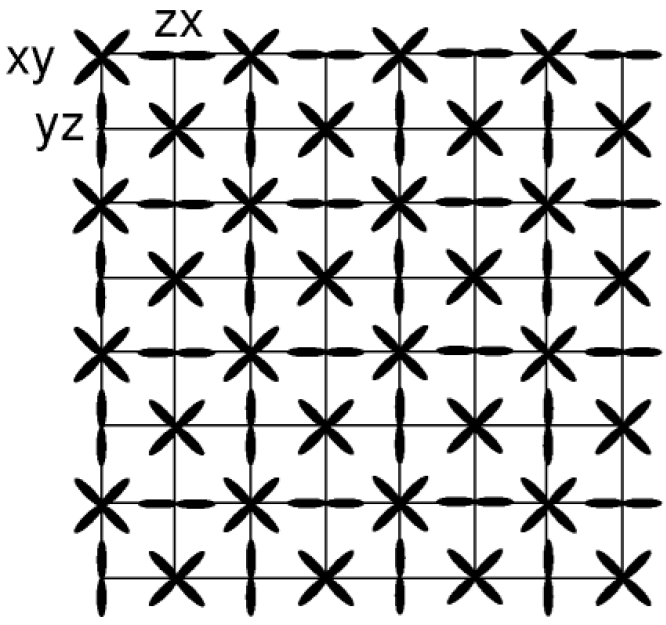

Figure 4.6: Schematic view of the antiferro-orbital ordered state predicted by Hotta and Dagotto for Ca_2RuO_4[74]. According to this model, the occupation of t_{2g} orbitals is different at nearest neighbor sites leading to a doubling of the periodicity within the RuO_2-plane with respect to the unit cell.

schematically shown in Figure 4.6. Each site with a doubly occupied d_{xy}-orbital has nearest neighbors with doubly occupied d_{xz}- and d_{xy}-orbitals, respectively. This orbital ordering pattern leads to a doubling of the crystal periodicity in the RuO_2-plane, which gives rise to the observation of additional Bragg reflections.
Considering these theoretical predictions with respect to the existence of orbital order in $Ca_3Ru_2O_7$, the magnetic interactions within the RuO_2 planes need to be taken into account. According to the susceptibility data [53, 60], the magnetic moments are coupled ferromagnetically in the planes. Based on the Goodenough-Kanomori rules, a ferro-orbital ordered state with doubly occupied d_{xy} orbitals and two singly occupied d_{xz}- and d_{xy}-orbitals is energetically unfavorable since electron hopping is complicated due to the ferromagnetic spin alignment. In contrast, an antiferro-orbital configuration in the RuO_2 planes, for instance the one suggested by Hotta and Dagatto, allows additional, energetically favorable hopping processes. Thus, in this simple picture, an antiferro-orbital state should be realized in $Ca_3Ru_2O_7$.

4.2 Experimental Details

The single crystalline $Ca_3Ru_2O_7$ samples were grown using the floating zone technique at the University of St. Andrews by N. Kikugawa and at the National Institute of Advanced Industrial Science by S. I. Ikeda and Y. Yoshida. Details on the growth technique and the crystal characterization have been given elsewhere [60]. The

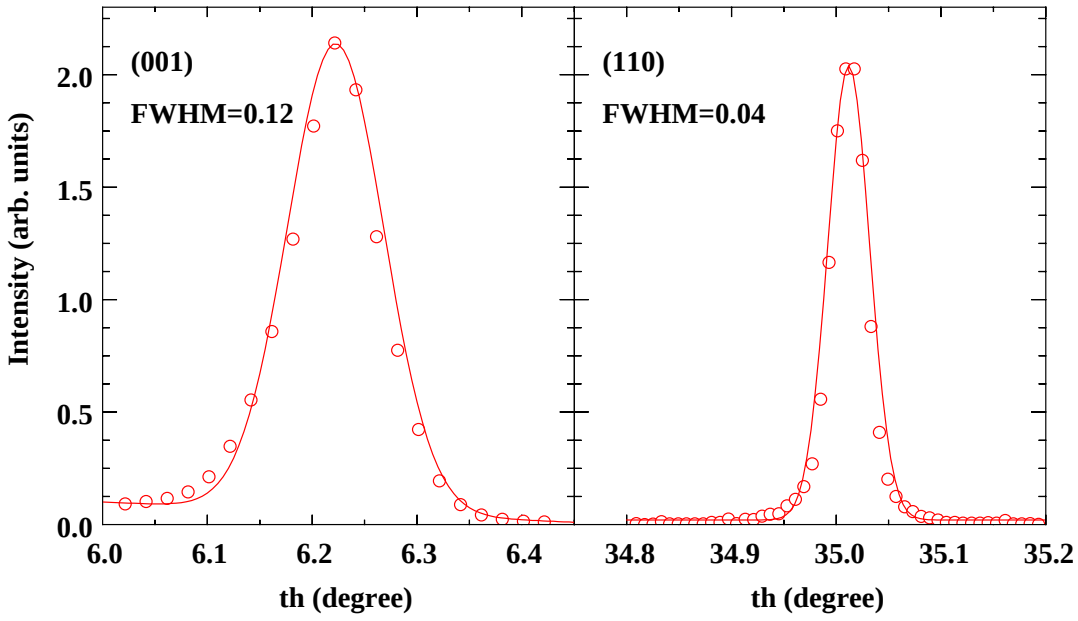

Figure 4.7: Rocking curves of $Ca_3Ru_2O_7$ crystals with orientation (001) and (110). The rocking curves have a full width at half maximum (FWHM) of less than 0.12°.

crystals are platelet shaped with the c-axis along the short axis and dimensions of $2\times1\times0.2\text{mm}^3$. They are almost untwinned; the ratio of orthorhombic twin domains is smaller than 0.1. Typical rocking curves, shown in Figure 4.7, have a full width at half maximum of less than 0.12° indicating a high crystal quality.
The crystals were prealigned in the x-ray laboratory at the Max Planck Institute for Solid State Research. The resonant x-ray diffraction experiments were carried out at beamline 4ID-D of the APS (Ru L-absorption edge), at beamline KMC-1 of BESSY (Ru L-absorption edge) and at beamline MagS of BESSY (Ru K-absorption edge). High energy x-ray diffraction studies in the presence of an applied magnetic field were performed at beamline BW5 of HASYLAB.

4.3 Magnetic Structure

Resonant x-ray diffraction was used to study the magnetic structure of $Ca_3Ru_2O_7$. At the Ru L-absorption edges two magnetic reflections, (001) and (110), were studied which are not allowed by charge Bragg scattering. Their energy dependence is shown in Figure 4.8. These energy profiles are normalized to the intensity of the incident x-ray beam but are not corrected for absorption effects. Both reflections exhibit a strong resonant enhancement at the Ru L-edges due to electric allowed dipole $2p \rightarrow 4d$ transitions which directly probe the partially occupied $4d$ orbitals responsible for magnetism. The magnetic signal vanishes below and above the absorption edges, since nonresonant magnetic scattering is too weak to be detected. The observation of a resonant signal at (001) and (110) is consistent with an A-type

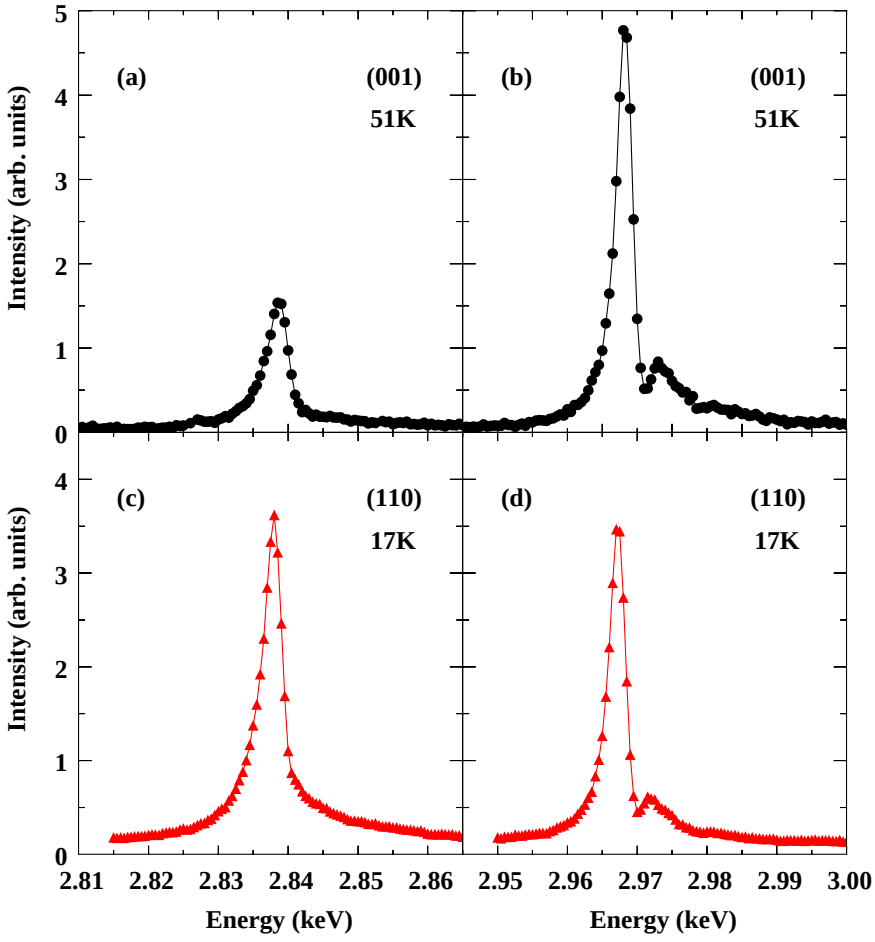

Figure 4.8: Energy dependence of the diffracted intensity at the magnetic reflections (001) and (110) near the Ru L-absorption edges. The energy profiles are not corrected for absorption.

AFM structure, as suggested by magnetization [53] as well as neutron scattering data [58]. Based on the absence of the (003) reflection in the neutron diffraction pattern, Yoshida *et al.* proposed that the magnetic moments are aligned ferromagnetically within the bilayers and antiferromagnetically between adjacent bilayers. Our data are consistent with this suggestion, since the (110) reflection would not be observed if another A-type AFM structure was realized.

In order to determine the direction of the magnetic moment, we studied the azimuthal and polarization dependence of the integrated intensity of the longitudinal reciprocal space scans at (001) and (110). The investigations of both reflections

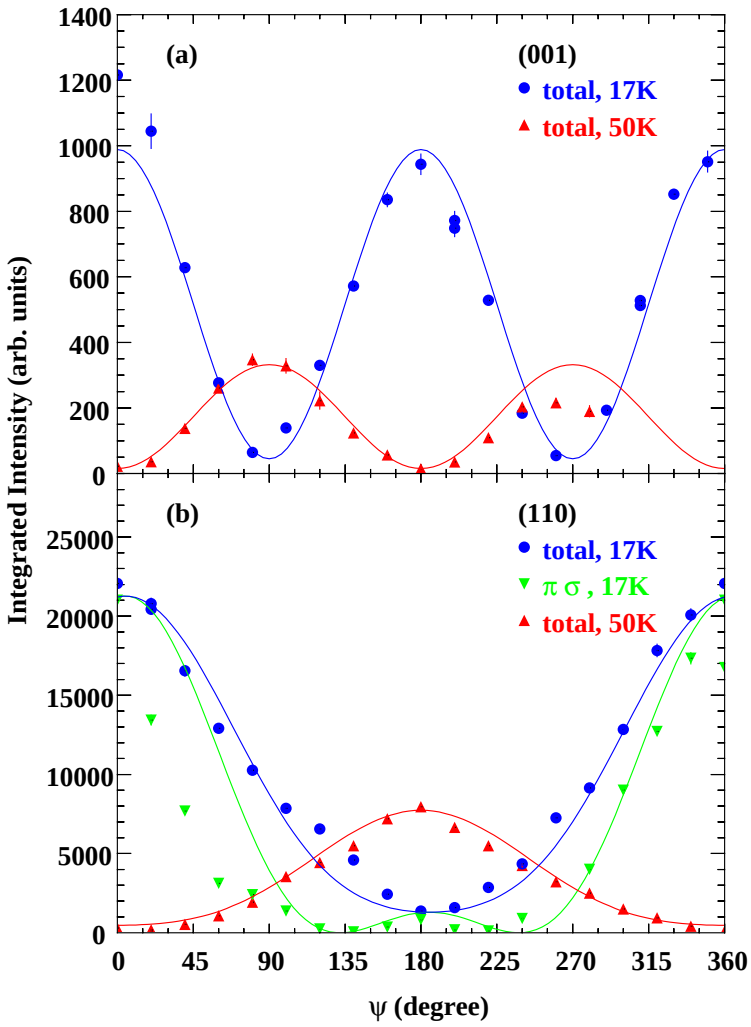

Figure 4.9: Azimuthal dependence of the scattered intensity at reflections (a) (001) and (b) (110) measured below and above T_{MI}. The solid lines are calculations based on the electric-dipole approximation and a magnetic moment direction along the *b*-axis below and along the *a*-axis above T_{MI}.

were carried out in horizontal scattering geometry, where the incident beam had π-polarization, and the diffracted beam contained two polarization components, namely σ' and π'. The azimuthal dependence of the resonant signal at reflection (001) measured below and above T_{MI} is shown in Figure 4.9a. In the low temperature phase, the maximum intensity is observed when the b-axis lies in the scattering plane ($\psi = 0°$), whereas the intensity almost vanishes when the a-axis is parallel to the diffraction plane ($\psi = 90°$). The opposite behavior is found in the metallic AFM phase above T_{MI}, where the azimuthal dependence is shifted by 90° with respect to the one below T_{MI}. The azimuthal dependence of the scattered intensity at wave vector (110), shown in Figure 4.9b, is quite different from that at (001). In the low temperature phase, the total intensity exhibits a maximum when the ab-plane coincides with the scattering plane, with the b-axis pointing towards the incident beam ($\psi = 0°$). Above T_{MI}, maximum intensity is found when the a-axis lies in the diffraction plane and points to the direction of the incident beam ($\psi = 180°$).

The observed azimuthal dependences at both reflections suggest a magnetic moment direction along the b-axis below T_{MI} and along the a-axis above T_{MI}. Therefore, the total scattering intensity at (001) and (110) has been calculated as a function of azimuthal angle based on these moment directions and an A-type AFM structure with ferromagnetic bilayers coupled antiferromagnetically along the c-axis as shown in Figure 4.10. To determine the total scattering intensity at a particular reflection all eight ruthenium ions of the unit cell need to be taken into account.

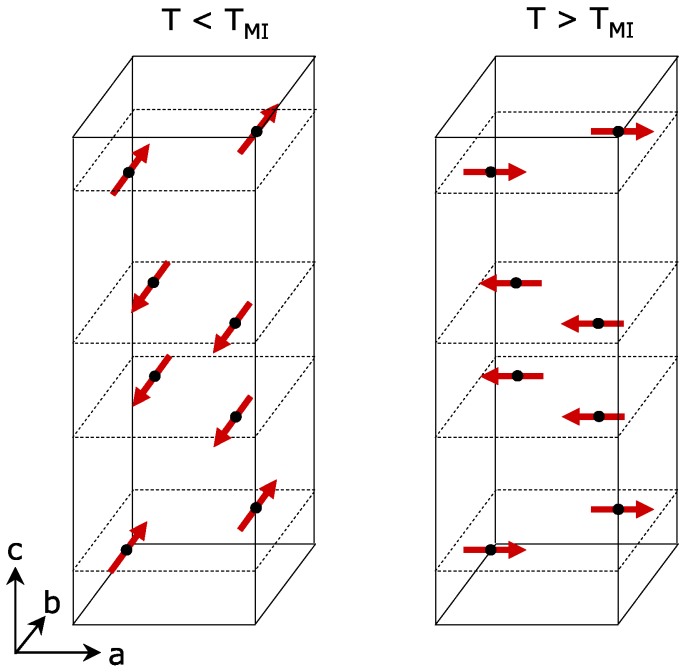

Figure 4.10: Magnetic structure of $Ca_3Ru_2O_7$ below and above T_{MI}.

The spin-up ions among them are located at

$$\mathbf{R}_1 = \left(\frac{1}{4}\,\frac{1}{4}\,\frac{1}{10}\right), \qquad \mathbf{R}_2 = \left(\frac{3}{4}\,\frac{3}{4}\,\frac{1}{10}\right),$$
$$\mathbf{R}_3 = \left(\frac{1}{4}\,\frac{1}{4}\,\frac{9}{10}\right), \qquad \mathbf{R}_4 = \left(\frac{3}{4}\,\frac{3}{4}\,\frac{9}{10}\right), \tag{4.1}$$

and the spin-down ions are found at

$$\mathbf{R}_5 = \left(\frac{1}{4}\,\frac{3}{4}\,\frac{2}{5}\right), \qquad \mathbf{R}_6 = \left(\frac{3}{4}\,\frac{1}{4}\,\frac{2}{5}\right),$$
$$\mathbf{R}_7 = \left(\frac{1}{4}\,\frac{3}{4}\,\frac{3}{5}\right), \qquad \mathbf{R}_8 = \left(\frac{3}{4}\,\frac{1}{4}\,\frac{3}{5}\right). \tag{4.2}$$

For reflection (001), the magnetic moment forms an angle of α =90° with the scattering vector and the scattering angle is $\theta = 6.1°$ at the Ru L_2-absorption edge. Using this information the diffracted intensity in the $\pi\sigma'$-channel at wave vector (001) is calculated according to Equations 2.1 and 2.15 as

$$\begin{aligned}
I^{\pi\sigma'}(001) &\propto \Big|\sum_{\mathbf{R}_j} e^{i(001)\boldsymbol{R}_j} f^{\pi\sigma'}_{\uparrow,\downarrow}\Big|^2 \\
&= \Big|f^{\pi\sigma'}_{\uparrow}\left(e^{\pi i\frac{1}{5}} + e^{\pi i\frac{1}{5}} + e^{\pi i\frac{9}{5}} + e^{\pi i\frac{9}{5}}\right) + f^{\pi\sigma'}_{\downarrow}\left(e^{\pi i\frac{4}{5}} + e^{\pi i\frac{4}{5}} + e^{\pi i\frac{6}{5}} + e^{\pi i\frac{6}{5}}\right)\Big|^2 \\
&\propto \Big|f^{\pi\sigma'}_{\uparrow} - f^{\pi\sigma'}_{\downarrow}\Big|^2 \\
&= \Big| - iF^{(1)}(m_x\cos\theta + m_z\sin\theta) + F^{(2)}m_y(m_x\sin\theta - m_z\cos\theta) \\
&\quad - \left(-iF^{(1)}(-m_x\cos\theta - m_z\sin\theta) - F^{(2)}m_y(-m_x\sin\theta + m_z\cos\theta)\right)\Big|^2 \\
&= \left|-2iF^{(1)}(m_x\cos\theta + m_z\sin\theta)\right|^2 \\
&= 4\,F^{(1)2}\left|(\cos\theta\sin\alpha\cos\psi - \sin\theta\cos\alpha)\right|^2 \\
&= 3.95\,F^{(1)2}\cos^2\psi,
\end{aligned} \tag{4.3}$$

where $f_\uparrow$ and $f_\downarrow$ denote the resonant scattering amplitude of a spin-up and a spin-down ion, respectively. The diffracted intensity in the $\pi\pi'$-channel at reflection (001)

is determined as

$$\begin{aligned} I^{\pi\pi'}(001) &\propto \left| f_{\uparrow}^{\pi\pi'} - f_{\downarrow}^{\pi\pi'} \right|^2 \\ &= \Big| F^{(0)} \cos 2\theta + iF^{(1)} m_y \sin 2\theta - F^{(2)} \cos^2\theta (m_x^2 \tan^2\theta + m_z^2) \\ &\quad - \left(F^{(0)} \cos 2\theta - iF^{(1)} m_y \sin 2\theta - F^{(2)} \cos^2\theta (m_x^2 \tan^2\theta + m_z^2) \right) \Big|^2 \\ &= \left| 2iF^{(1)} m_y \sin 2\theta \right|^2 \\ &= 4F^{(1)2} \left| \sin 2\theta \sin\alpha \sin\psi \right|^2 \\ &= 0.18\ F^{(1)2} \sin^2\psi. \end{aligned} \tag{4.4}$$

Hence, the total scattering intensity at the reciprocal space position (001) is given by

$$\begin{aligned} I^{total}(001) &= I^{\pi\sigma'}(001) + \cos 2\theta\ I^{\pi\pi'}(001) \\ &\propto F^{(1)2} \left(3.95\ \cos^2\psi + 0.18\ \sin^2\psi \right), \end{aligned} \tag{4.5}$$

where the intensity of the $\pi\pi'$-channel has been multiplied with $\cos 2\theta$ in order to take into account the attenuation of the signal as the Brewster angle is approached. At reflection (110), the magnetic moment forms an angle of $\alpha \approx 45^\circ$ with the scattering vector and the scattering angle amounts $\theta = 32.7^\circ$ at a photon energy of 2.968 keV. The intensity in the $\pi\sigma'$-channel at wave vector (110) is calculated as

$$\begin{aligned} I^{\pi\sigma'}(110) &\propto \left| \sum_{\mathbf{R}_j} e^{i(110)\boldsymbol{R}_j} f_{\uparrow,\downarrow}^{\pi\sigma'} \right|^2 \\ &= \left| f_{\uparrow}^{\pi\sigma'} \left(e^{\pi i} + e^{3\pi i} + e^{\pi i} + e^{3\pi i} \right) + f_{\downarrow}^{\pi\sigma'} \left(e^{2\pi} + e^{2\pi} + e^{2\pi} + e^{2\pi} \right) \right|^2 \\ &\propto \left| f_{\downarrow}^{\pi\sigma'} - f_{\uparrow}^{\pi\sigma'} \right|^2 \\ &= \Big| - iF^{(1)} (m_x \cos\theta + m_z \sin\theta) + F^{(2)} m_y (m_x \sin\theta - m_z \cos\theta) \\ &\quad - \left(-iF^{(1)} (-m_x \cos\theta - m_z \sin\theta) - F^{(2)} m_y (-m_x \sin\theta + m_z \cos\theta) \right) \Big|^2 \\ &= \left| -2iF^{(1)} (m_x \cos\theta + m_z \sin\theta) \right|^2 \\ &= 4\ F^{(1)2} \left| (\cos\theta \sin\alpha \cos\psi - \sin\theta \cos\alpha) \right|^2 \\ &= 4\ F^{(1)2} \left| (0.60 \cos\psi - 0.38) \right|^2 \\ &= F^{(1)2} \left(1.44 \cos^2\psi - 1.84 \cos\psi + 0.58) \right). \end{aligned} \tag{4.6}$$

The intensity in the $\pi\pi'$-channel at reflection (110) is given by

$$\begin{aligned} I^{\pi\pi'}(110) &\propto \left| f_{\downarrow}^{\pi\pi'} - f_{\uparrow}^{\pi\pi'} \right|^2 \\ &= \Big| F^{(0)} \cos 2\theta + iF^{(1)} m_y \sin 2\theta - F^{(2)} \cos^2\theta (m_x^2 \tan^2\theta + m_z^2) \\ &\quad - \left(F^{(0)} \cos 2\theta - iF^{(1)} m_y \sin 2\theta - F^{(2)} \cos^2\theta (m_x^2 \tan^2\theta + m_z^2) \right) \Big|^2 \\ &= \left| 2iF^{(1)} m_y \sin 2\theta \right|^2 \\ &= 4F^{(1)2} \left| \sin 2\theta \sin\alpha \sin\psi \right|^2 \\ &= 1.65\ F^{(1)2} \sin^2\psi. \end{aligned} \tag{4.7}$$

Thus, the total intensity at (110) takes the following form

$$\begin{aligned} I^{total}(110) &= I^{\pi\sigma'}(110) + \cos 2\theta\ I^{\pi\pi'}(110) \\ &\propto F^{(1)2} \left(1.44 \cos^2\psi - 1.84 \cos\psi + 0.58 + 0.69\ \sin^2\psi \right). \end{aligned} \tag{4.8}$$

The simulation results are shown as solid curves in Figure 4.9. They are in good agreement with the experimental data and hence confirm the magnetic moment orientations along the b-axis below and along the a-axis above T_{MI}.

The temperature dependence of the integrated intensities of both reflections is displayed in Figure 4.11. Both reflections exhibit almost the same temperature dependence at $\psi = 0°$, which corresponds to the maximum intensity position in the low temperature phase. Below T_{MI}, the intensity remains approximately constant with increasing temperature, followed by an intensity loss of approximately two orders of magnitude at T_{MI}. This drastic intensity change is mainly due to the reorientation of the magnetic moment and consistent with the azimuthal dependence shown in Figure 4.9. In the metallic AFM phase, the intensity further decreases upon heating and continuously vanishes at T_N, as expected for a second-order phase transition. Figure 4.11(b) shows the temperature dependence at wave vector (110) for $\psi = 180°$, where the moment reorientation results in an intensity enhancement by almost one order of magnitude above T_{MI}. From a comparison of the maximum intensities in the two phases we conclude that the amplitude ratio of sublattice magnetizations in the metallic and insulating states is $\sim 1/\sqrt{3}$.

Figure 4.12 shows longitudinal reciprocal space scans of both reflections, which have been fitted with Lorentzian profiles at (001) and with Gaussian functions at (110), respectively. For both reflections, the half width at half maximum (HWHM) of the scans does not change significantly as a function of temperature and shows no anomaly at T_{MI}. The HWHM takes a value of 0.0065(5) rlu at (001). In contrast, it amounts 0.0005(3) rlu at (110), which might be resolution limited due to the Gaussian shape. The large difference in the HWHM indicates that the in-plane magnetic correlation length is much larger than the out-of-plane correlation length.

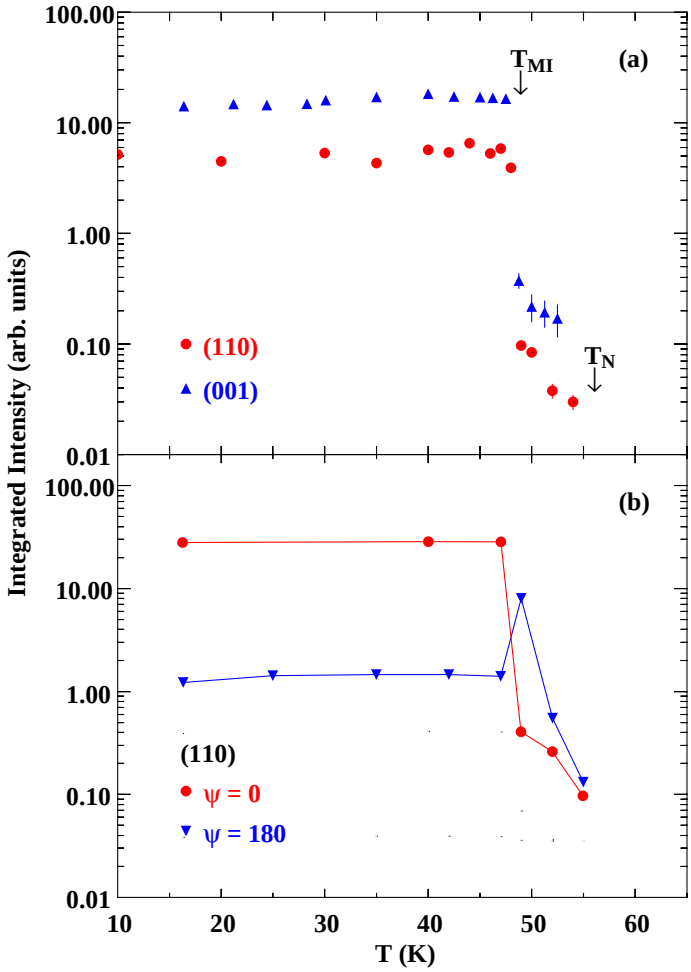

Figure 4.11: (a) Temperature dependence of the integrated intensity at the magnetic reflections (001) and (110) measured at $\psi = 0°$ and (b) temperature dependence of the scattered intensity at wave vector (110) taken at $\psi = 0°$ and $\psi = 180°$.

This is acutally not surprising since the coupling within the RuO_2 planes is expected to be much stronger than the one between neighboring planes. The correlation length ξ_{hkl} can be estimated by the following expression

$$\xi_{hkl} = \frac{d_{hkl}}{2\pi \text{ HWHM}}, \tag{4.9}$$

where d_{hkl} denotes the lattice distance of a particular reciprocal space vector. This approximation leads to an in-plane correlation length of ~ 1200 Å and an out-of-plane correlation length of ~ 450 Å.

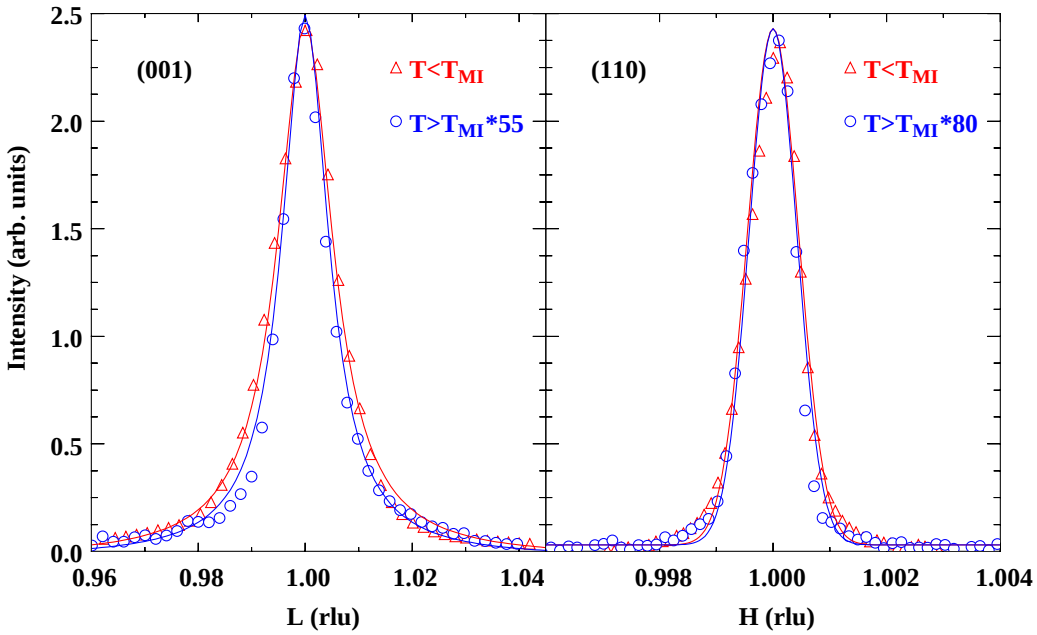

Figure 4.12: Longitudinal reciprocal space scans at reflections (001) and (110) measured at $\psi = 0°$. The scans are fitted with Lorentzian profiles at (001) and with Gaussian profiles at (110).

4.4 Orbital Order

In order to obtain direct evidence of orbital order, we searched for resonant superstructure reflections characteristic of an antiferro-orbital (AFO) order at various high-symmetry positions in reciprocal space including (1/2 1/2 0), (1 0 0), (0 1 0), (1/2 0 0), and (0 1/2 0), with the photon energy tuned to one of the Ru L-absorption edges, but we did not find any signal above background. In Ca_2RuO_4, orbital order with the same propagation vector as the antiferromagnetically ordered state was deduced from the persistence of a weak resonant reflection above the magnetic ordering temperature [75]. An analogous phenomenon (namely, weak A-type AFO order) would not be detectable in $Ca_3Ru_2O_7$, because the magnetic ordering temperature exceeds the onset of orbital order so that the magnetic intensity would dominate at all temperatures.

To look for ferro-orbital order (FO) order, which manifests itself as resonant intensity at the main crystallographic Bragg reflections, we made use of the resonant x-ray interference technique where the orbital signal is amplified due to the interference with the Thomson scattering as discussed in Chapter 2. In principle, this experiment can also be performed at the Ru L-absorption edges where the FO signal is expected to be most pronounced. However, this option is unfavorable based on two considerations. First, all Bragg reflections that can be reached at this pho-

ton energy have a magnetic contribution that is expected to dominate the orbital one. Second, the polarization analyzer currently available for this energy, Si (111), has an extremely small mosaicity, which causes additional experimental problems. Following the protocol established by Kiyama and coworkers [43, 44], we therefore performed the experiment at the Ru K-absorption edge, using pyrolytic graphite as analyzer.

Although a strong contribution from magnetic order is not expected to be present at the Ru K-edge, a b-axis reflection was chosen to be investigated. For this orientation, a magnetic signal, if present at all, gives rise to additional resonant intensity, which does not show any azimuthal dependence, since the magnetic moment is parallel to the scattering vector below T_{MI}. In contrast, a signal due to orbital order

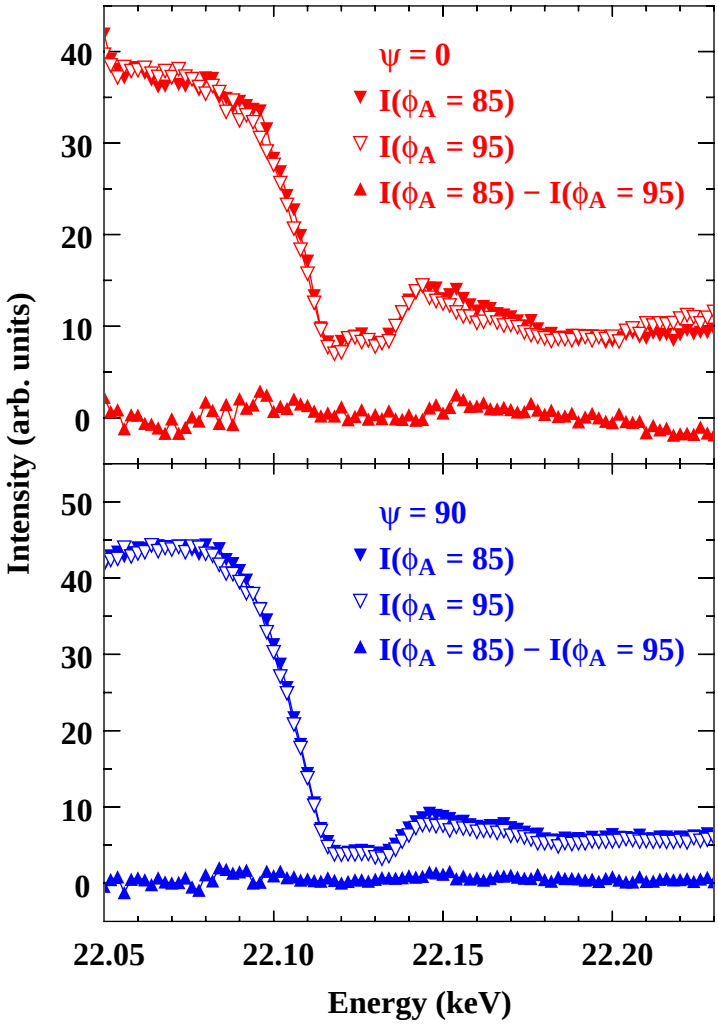

Figure 4.13: Energy scans for $\phi_A = 85°$ and $\phi_A = 95°$ at the reflection (060) taken at two azimuthal positions $\psi = 0°$ and $\psi = 90°$ measured at 20K.

is expected to exhibit an azimuthal angle dependence and thus orbital order can be identified by measuring an azimuthal dependence of the observed signal. Figure 4.13 shows energy scans near the Ru K-absorption edge at the reflection (0 6 0) taken at two azimuthal positions. The difference of the two signals measured at $\phi_A = 85°$ and $\phi_A = 95°$ does not indicate any FO contribution, since the latter would give rise to a signal difference at the resonance energy which is clearly not observed. In addition to searching for a FO signal within a wide azimuthal range of 180°, we also varied the angular difference Δ between the two analyzer positions, but no FO intensity was detected within the experimental sensitivity.
Discussing this result in comparison with single layered Ca_2RuO_4, where a substantial FO signal has been revealed using the same experimental method [76], the amplitude of the FO signal, if present at all, has to be considerably weaker in $Ca_3Ru_2O_7$. This is not unexpected in view of the much lower metal-insulator transition temperature in $Ca_3Ru_2O_7$ and the ability of a small applied magnetic field to rearrange or destroy the orbital order in this material [57]. Corresponding magnetic field-induced transitions have not been reported for Ca_2RuO_4, indicating that orbital ordering phenomena are more robust in that compound. The relatively weak FO order parameter in $Ca_3Ru_2O_7$, yielding a resonant signal below our detection limit, could result from orbital quantum fluctuations or residual charge fluctuations in the insulating state.

4.5 Structural investigations in an applied magnetic field

To investigate the coupling between various degrees of freedom in $Ca_3Ru_2O_7$, several studies in an applied magnetic field have been carried out. While these have been focused on transport and magnetization measurements [53, 54], we have investigated the structural in-plane changes in the vicinity of the metal-insulator transition as a function of applied magnetic field complementing studies by C. Nelson *et al.* [56].
Figure 4.14 shows longitudinal reciprocal space scans at reflections (200) and (020) measured in zero field at 100 keV near T_{MI}. A clear shift in the position of both reflections is observed between 48.1 K and 48.6 K due to the lattice contraction in the ab-plane at T_{MI}. The shift of the reflections corresponds to a lattice parameter change of -0.07 % and -0.03 % along the a- and b-axis, respectively.

The field dependence of the structural changes was investigated for applied magnetic fields along the a- and b-axis. The results for both field directions are summarized in Figure 4.15 and 4.16, where the relative change of the lattice parameters with respect to their values at 25 K is plotted as a function of temperature. For both field orientations, the onset of the structural change is initially shifted to lower temperatures indicating a stabilization of the high temperature phase as a function of applied magnetic field. However, the magnitude of the shift as well as the temperature range of the structural change is quite different for both field directions suggesting a large anisotropy as a function of magnetic field consistent with trans-

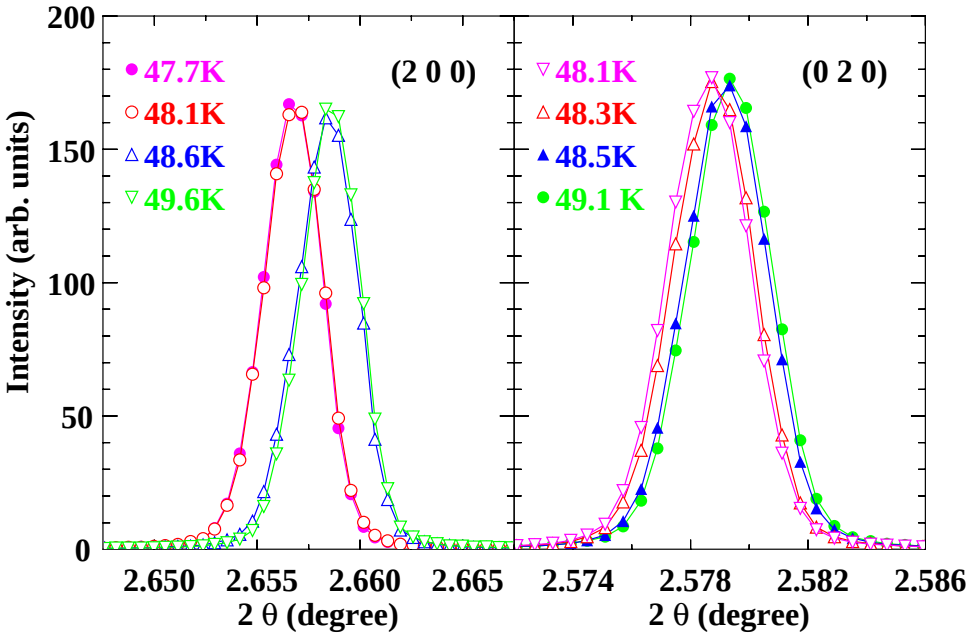

Figure 4.14: Reciprocal space scans at reflections (200) and (020) in zero field as a function of temperature near T_{MI}.

port and magnetization results [53, 54].

For $B \parallel a$, a step like change of the in-plane lattice parameters is observed for all magnetic fields, its magnitude is almost field independent. This suggests that the structural phase transition is of first order for all fields. Evidences for a phase transition have also been detected by other experimental methods, including transport and magnetization [53, 54], which are sensitive to the charge and spin degrees of freedom, respectively. For a better comparison, the transition temperatures deduced by various experimental probes have been plotted together in a BT phase diagram, which is shown in Figure 4.17. The structural transition coincides with the magnetic and metal-insulator transition, separating the insulating AFM phase from the metallic AFM state at low fields and from the metallic paramagnetic phase at high fields, respectively. This clearly demonstrates a strong coupling between the spin, charge and lattice degree of freedom in $Ca_3Ru_2O_7$.

A step like change of the in-plane lattice parameters is also found for $B \parallel b$ and fields below 2 T (Figure 4.16), however, the transition starts to broaden between 2 T and 4 T resulting in a gradual change of the lattice constants at higher fields. This indicates that the nature of the transition changes between 2 T and 4 T, being of first order at low fields and of second order at high fields. In addition, the onset of the transition is initially shifted to lower temperatures with increasing field, but starts to decrease again around 6 T, where the metamagnetic transition is observed. Since a transition temperature is difficult to define for fields above 2 T, a transition

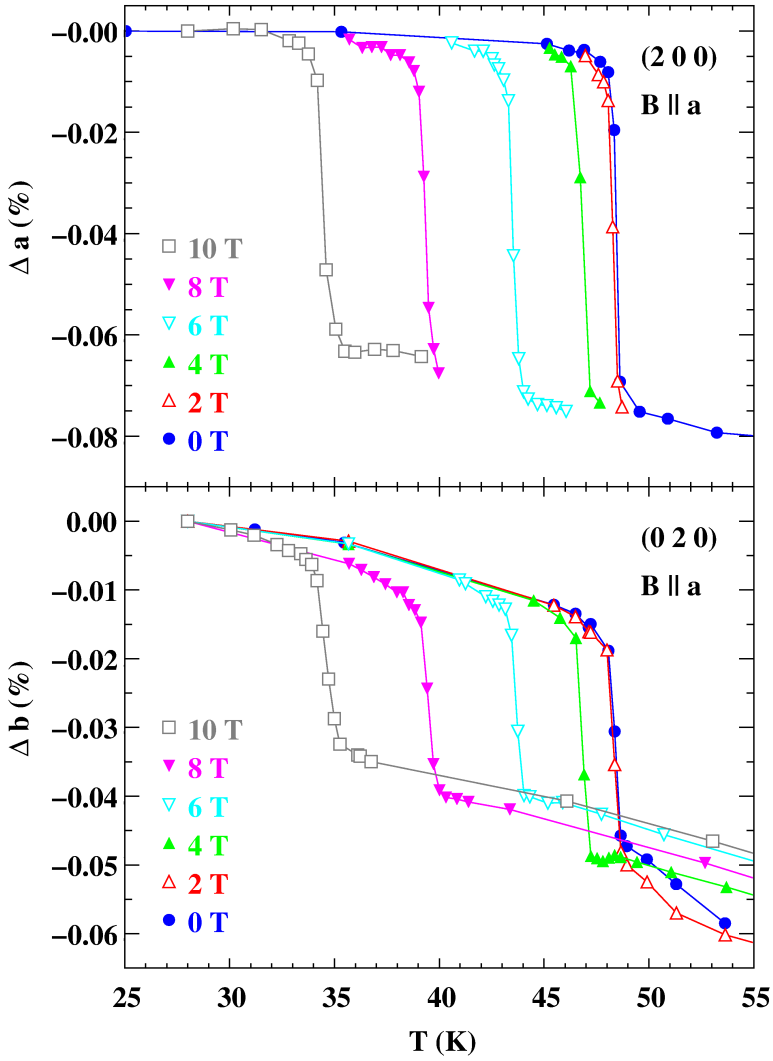

Figure 4.15: Lattice parameter change as a function of temperature for $B \parallel a$.

range characterized by two temperatures, marking the starting and the end point of the transition (dashed lines in Figure 4.16), has been extracted from the each data set of Figure 4.16. For comparison, the results have been plotted along with the data extracted by other experimental methods in a BT-diagram, displayed in Figure 4.17. For magnetic fields below 2 T, the structural, magnetic and metal-insulator transition coincide, clearly indicating the transition from the insulating AFM phase to the metallic AFM phase. The situation is more complicated for high magnetic fields: The shaded region in the phase diagram, defined by the starting and end points of the structural changes of Figure 4.16, is characterized by a gradual structural change. At its boundaries, anomalies are also found in the magnetization and transport data [53, 54]. For the interpretation of the shaded region, it is helpful to discuss the results of a neutron diffraction study [65], which have not been included

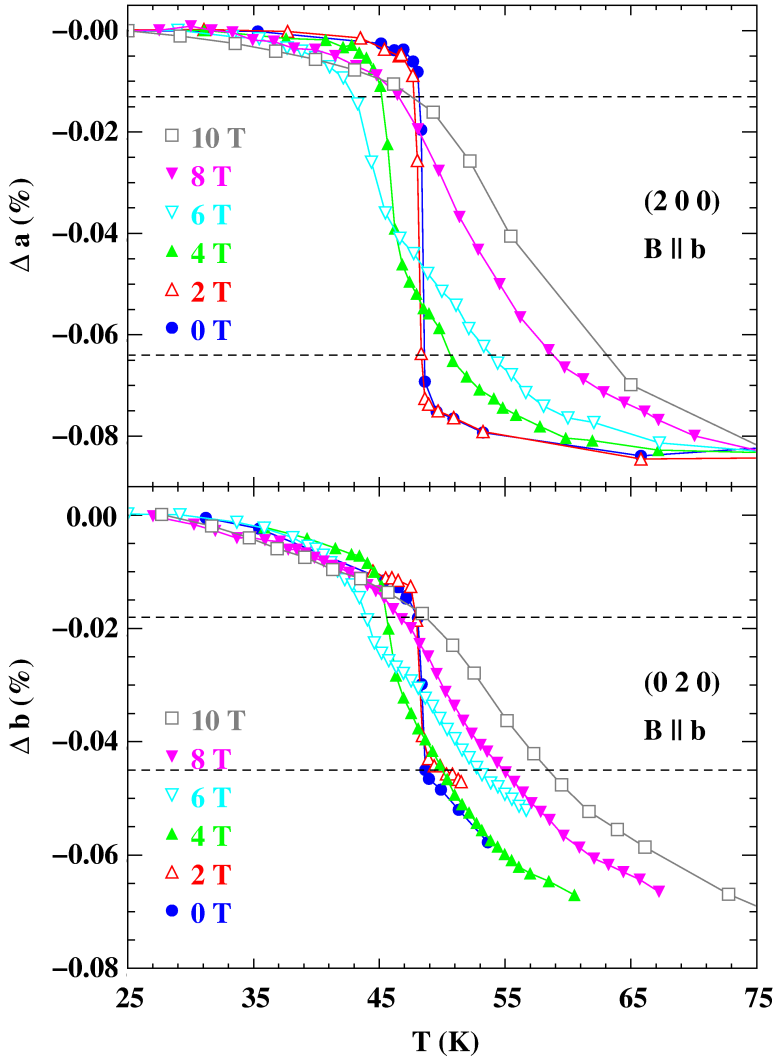

Figure 4.16: Lattice parameter change as a function of temperature for $B \parallel b$.

in the diagram, since the zero field transition temperatures of the investigated crystals differ significantly from those reported in literature. Despite this difference, the neutron results give valuable information about the magnetic phases as a function of magnetic field and temperature. According to the neutron data, the shaded region corresponds to a second order phase transition from a canted antiferromagnetic (CAFM) phase to a paramagnetic state. In the CAFM phase, the magnetic moment is predominantly aligned ferromagnetically along the b-axis with a small antiferromagnetic canting along the a-axis. Considering this issue, the second order phase transition is characterized by a continuous decrease of the AFM component. Due to the strong spin-charge-lattice coupling this transition is reflected in the structure, namely in the gradual change of the in-plane lattice parameters, we observe using x-ray diffraction.

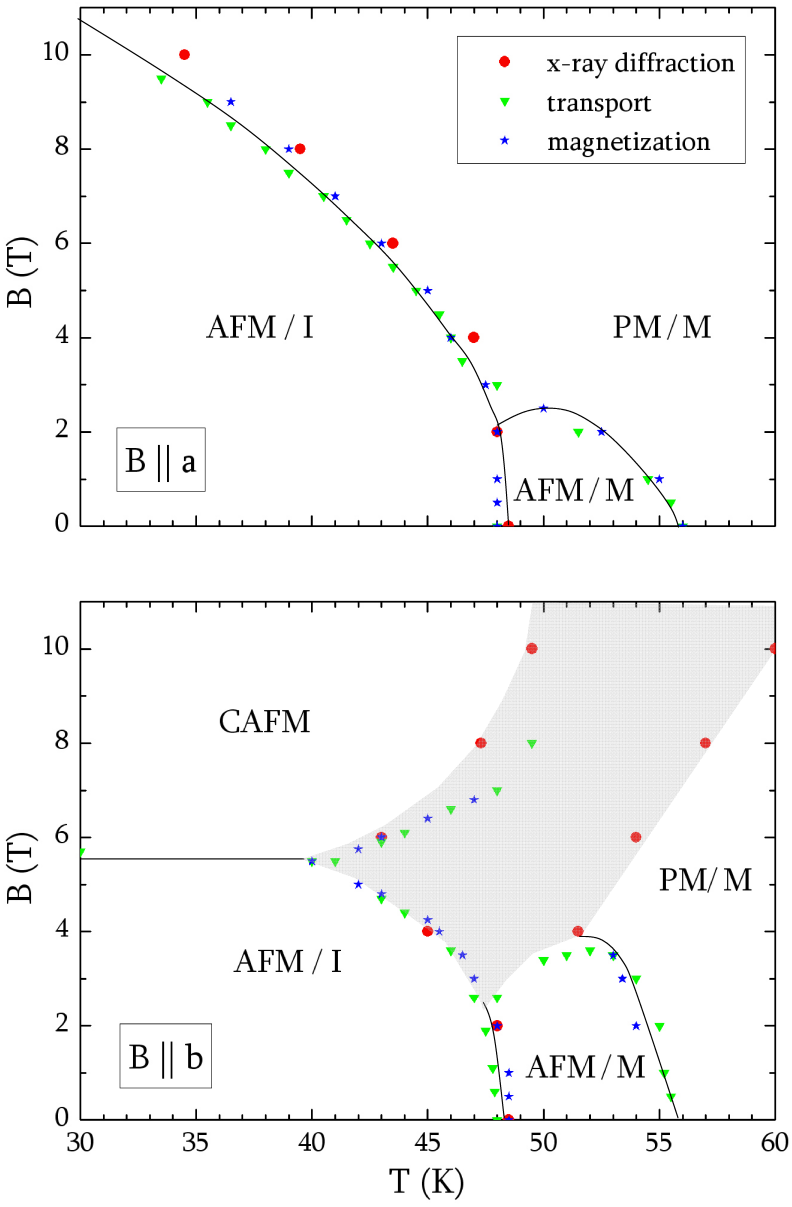

Figure 4.17: Phase diagram of $Ca_3Ru_2O_7$ for $B \parallel a$ and $B \parallel b$ deduced from structural changes detected by x-ray diffraction, transport and magnetization data [53, 54]. Various magnetic phases arise in an applied magnetic field including an insulating antiferromagnetic state (AFM / I), a metallic antiferromagnetic state (AFM / M), a metallic paramagnetic state (PM /M) and a canted antiferromagnetic (CAFM) state.

4.6 Discussion

One of the most significant results of our x-ray diffraction studies is the determination of the magnetic structure of $Ca_3Ru_2O_7$ in its insulating and metallic AFM phase, and the related observation of the magnetic moment reorientation at T_{MI}. While insulating AFM states are common in transition metal oxides, metallic AFM states, as the one observed in $Ca_3Ru_2O_7$ between T_{MI} and T_N, are quite unusual. Nevertheless, a related phenomenon has been observed in bilayered manganates which also exhibit A-type antiferromagnetism [66]. The small amplitude of the ordered magnetic moment in this phase is probably due to charge or orbital fluctuations, which complicate the formation of long range magnetic order. Considering the strong spin-orbit interaction and the weak Jahn-Teller coupling of the $4d$ t_{2g} electrons, an unquenched orbital magnetization is expected. Additional terms in the spin Hamiltonian induced by the orbital moment may then be responsible for the observed magnetic moment reorientation at the metal-insulator transition.
X-ray diffraction has also been used to investigate the lattice degree of freedom of $Ca_3Ru_2O_7$ near the metal-insulator transition in an applied magnetic field. The anisotropic behavior of the structural changes found for magnetic fields applied along the a- and b-axis give rise to a phase diagram that is in good agreement with the results available from transport and magnetization measurements, confirming a strong spin-charge-lattice coupling in the material.
Although orbital order has been proposed by various experiments, our resonant x-ray diffraction investigation has not given any evidence for orbital order within the experimental sensitivity. This indicates that the orbital order parameter is significantly weaker than in the single layered counterpart Ca_2RuO_4. Weak orbital order in combination with a strong spin-orbit coupling are presumably at least partially responsible for the rich phase behavior of $Ca_3Ru_2O_7$ observed in applied magnetic fields.

Chapter 5

Magnetic Structure of $RuSr_2GdCu_2O_8$

$RuSr_2GdCu_2O_8$ and related materials with alternating RuO_2 and CuO_2 layers have attracted tremendous scientific interest in recent years, mainly due to the microscopic coexistence of long-range magnetic order and superconductivity [77, 78, 79]. With a magnetic ordering temperature $T_N = 100 - 150$ K and a superconducting transition temperature of $\sim 15 - 50$ K, $RuSr_2GdCu_2O_8$ exhibits one of the broadest coexistence range of magnetic order and superconductivity. This makes $RuSr_2GdCu_2O_8$ an ideal compound to study the interplay between these cooperative phenomena.

5.1 Properties of $RuSr_2GdCu_2O_8$

The crystal structure of $RuSr_2GdCu_2O_8$ is shown in Figure 5.1. The material consists of RuO_2 layers and CuO_2 bilayers, which extend parallel to the *ab*-plane. Each Cu ion is surrounded by five oxygen ions forming a CuO_5 square pyramid. The Ru ions are located in the center of corner-sharing RuO_6 octahedra, which are alternatingly rotated by 13.8° clockwise and anticlockwise around the crystallographic *c*-axis [80]. In addition, the polyhedra are slightly tilted reducing the Cu-O-Ru angle to 173° [81]. The crystal structure is approximately tetragonal with room-temperature lattice parameters $a = b = 3.836$ Å and $c = 11.563$ Å [80]. Although small orthorhombic distortions have been reported in the literature [82, 83], all Bragg reflections are indexed in the tetragonal space group $P4/mmm$ in the following, unless noted otherwise.

The formal oxidation states of Ru and Cu in $RuSr_2GdCu_2O_8$ are +5 and +2, respectively. However, there is clear evidence for a charge transfer between the RuO_2 and the CuO_2 planes. If p denotes the charge transferred between the planes, the oxidation states of Ru and Cu become 5-2p and and 2+p, respectively. According to absorption studies [84], nuclear magnetic resonance (NMR) [85, 86, 87] and ferromagnetic resonance (FMR) [88], the charge transfer is approximately $p = 0.2$. Hence, Cu has a valence of +2.2, which is close to the value for optimal hole doping

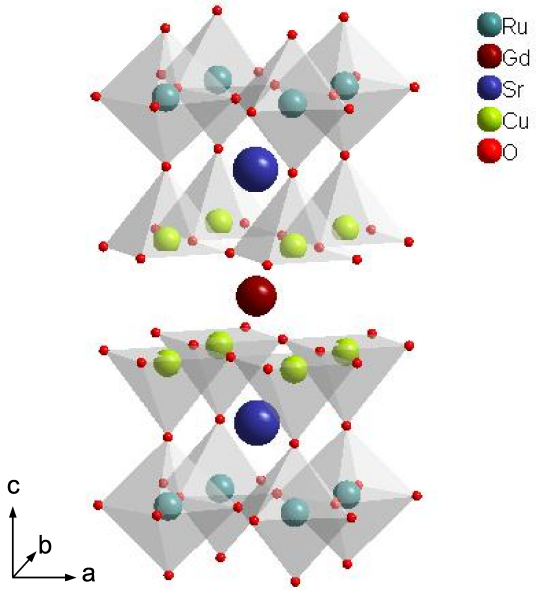

Figure 5.1: Crystal structure of $RuSr_2GdCu_2O_8$.

in many superconducting cuprates. On the ohter hand, the valence of +4.6 for Ru corresponds to a ratio of Ru^{5+}: Ru^{4+} = 60% : 40%. The electron configurations of Ru^{5+} and Ru^{4+} are $4d^3$ and $4d^4$, respectively. Since the $e_g t_{2g}$-crystal field splitting in $RuSr_2GdCu_2O_8$ is larger than the Hund coupling, all valence electrons occupy the t_{2g} orbitals, leading to a $t_{2g}^3 e_g^0$ configuration for Ru^{5+} and a $t_{2g}^4 e_g^0$ configuration for Ru^{4+}.

Long-range magnetic order is established in the RuO_2 planes of $RuSr_2GdCu_2O_8$ below $T_N = 100 - 150$ K. Since most investigations have been carried out on powder samples, the information about the nature of the magnetic state is limited and is to some extend even contradictory. Neutron powder diffraction experiments have revealed magnetic superstructure reflections below T_N, which indicate antiferromagnetic order in all three crystallographic directions (G-type antiferromagnetism) [89, 90], as schematically shown in Figure 5.2. Although a magnetic structure refinement could not be performed, the neutron powder diffraction data suggest a magnetic moment direction along the c-axis perpendicular to the RuO_2 layers. In addition, an upper limit of 0.2 μ_B/Ru has been determined for a ferromagnetic moment component which might result from spin canting. These assumptions have been supported by a magnetization study, carried out on an Eu substituted compound [91]. In contrast, NMR [87] and FMR data [88] have been interpreted in terms of an antiferromagnetic state consisting of ferromagnetic RuO_2 layers stacked antiferromagnetically along the c-axis (A-type antiferromagnetism) and a magnetic moment orientation in the RuO_2 planes, as schematically shown in Figure 5.2. The net ferromagnetic exchange field in the CuO_2 layers implied by the this scenario would cause the intimate coupling between ferromagnetism and d-wave superconductivity that has motivated much of the work on $RuSr_2GdCu_2O_8$ [77, 78, 79].

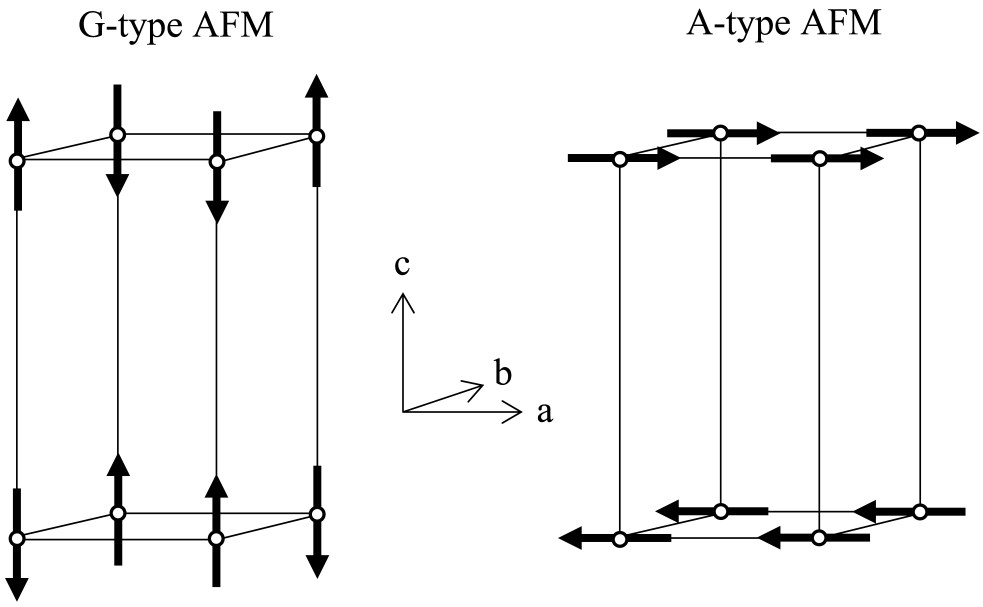

Figure 5.2: Proposed magnetic structures of $RuSr_2GdCu_2O_8$. While neutron powder diffraction data suggest a G-type antiferromagnetic structure [89, 90], FMR and NMR studies indicate an A-type antiferromagnetic structure [88, 87].

In addition to the magnetic order of the Ru sublattice, the Gd ions order antiferromagnetically in all three crystallographic directions below 2.5 K [89]. The magnetic moment of 7 μ_B/Gd is aligned along the c-axis. The Ru and Gd spin systems are only weakly coupled to each other due to the position of the Gd ions with respect to the Ru ions. Every Gd ion is located in the body-center of the tetragonal Ru lattice. An antiferromagnetic structure of the Ru subsystem then results in an average cancellation of the interactions between the Ru and Gd spins.
While the CuO_2 planes are not involved in the magnetism of $RuSr_2GdCu_2O_8$, they play a crucial role for the superconductivity. The superconducting transition depends strongly on the crystal preparation and is observed between 15 K and 50 K. Various experimental techniques like thermoelectric power, resistivity and heat capacity studies have confirmed the existence of bulk superconductivity [92].

5.2 Experimental Details

The $RuSr_2GdCu_2O_8$ samples with typical sizes of $100 \times 100 \times 50\ \mu m^3$ were grown by C. T. Lin using the self-flux method at the Max Planck Institute for Solid State Research. Details on the growth technique and the crystal characterization have been given elsewhere [93]. Since the growth product, a large polycrystalline piece, also contained the impurity phases Gd_2CuO_4, Sr_2RuO_4 and $RuSr_{10}Pt_2Cu_3O_{14}$, the $RuSr_2GdCu_2O_8$ crystals needed to be crystallographically identified and separated from the other phases. To this end, a small crystal was chosen out of a large poly-

crystalline piece and mounted on a sample holder. Its crystal structure was then determined by using the x-ray diffraction setup available in the laboratory. Empirically, one out of five samples was identified as a $RuSr_2GdCu_2O_8$ crystal. Once a crystal with the correct phase was found, it was prealigned along the direction needed for the synchrotron experiments. For this purpose, the crystal usually had to be reglued, which was a nontrivial task due to the small crystal size and the nonsymmetric crystal shape. The resonant x-ray diffraction experiments were carried out at beamline 4ID-D of the APS and at beamline KMC-1 of BESSY.
Magnetization measurements, shown in Figure 5.3, reveal a magnetic ordering temperature of 102 K. This transition temperature is consistent with prior single-crystal data [77], but lower than that of most polycrystalline samples reported in the literature [77, 78, 79]. On the other hand, the superconducting transition temperature $T_c = 45$ K, also seen in the magnetization measurements, is higher than that of typical $RuSr_2GdCu_2O_8$ powders. These differences are probably due to variations of the distribution of Ru, Cu, or O ions with the synthesis conditions.

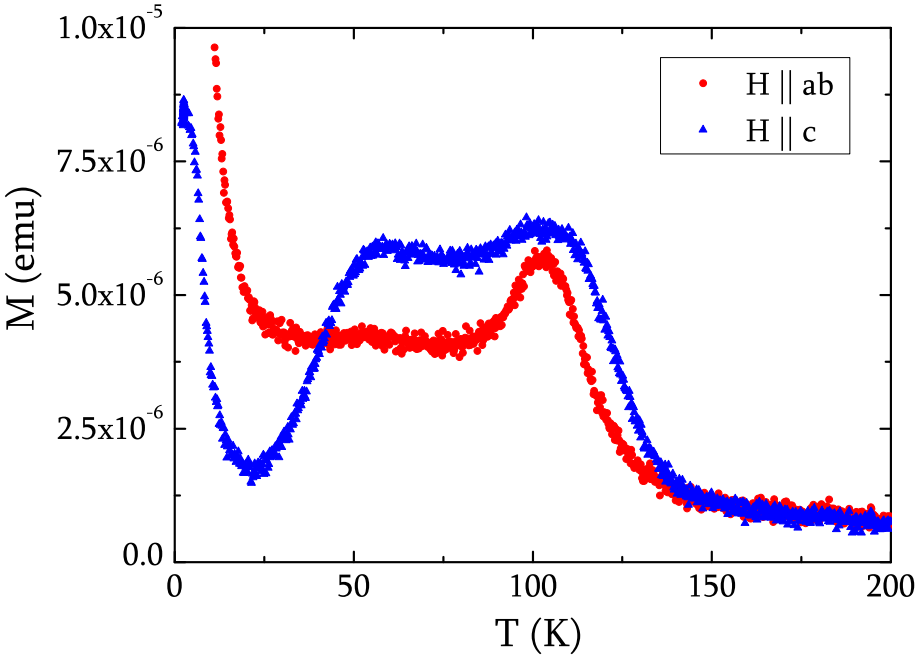

Figure 5.3: Single crystal magnetization data measured at 100 Oe. The Néel and superconducting transition temperatures are in good agreement with previously reported single crystal data [77].

5.3 Magnetic structure

In order to at least partly resolve the controversy concerning the magnetic structure of $RuSr_2GdCu_2O_8$, we have performed a resonant x-ray diffraction study with the photon energy tuned close to the L_2-absorption edge of ruthenium. Figure 5.4 shows the energy dependence of the intensity of the reflections $(\frac{1}{2}\ \frac{1}{2}\ \frac{1}{2})$ and $(\frac{1}{2}\ \frac{1}{2}\ \frac{3}{2})$. For both reflections, a large resonant enhancement of the magnetic scattering cross-section is observed at the L_2-absorption edge. This originates from electric dipole transitions from the $2p$ core level directly into the partly occupied $4d$ t_{2g} orbitals. A second, weaker resonant peak approximately 4 eV above the absorption edge is probably due to electric dipole transitions into the unoccupied $4d$ e_g orbitals, as previously observed in resonant x-ray diffraction experiments on Ca_2RuO_4 [75]. No off-resonant scattering was observed above background. The intensity of the reso-

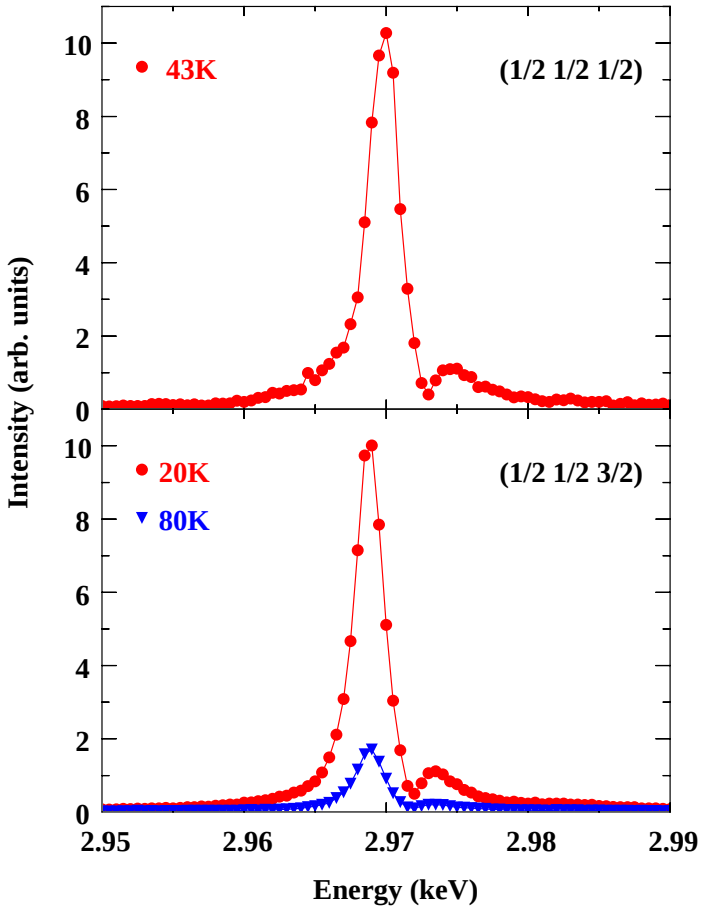

Figure 5.4: Energy dependence of the scattered intensity at the reflections $(\frac{1}{2}\ \frac{1}{2}\ \frac{1}{2})$ and $(\frac{1}{2}\ \frac{1}{2}\ \frac{3}{2})$ near the Ru L_2-absorption edge. The energy profiles have not been corrected for absorption.

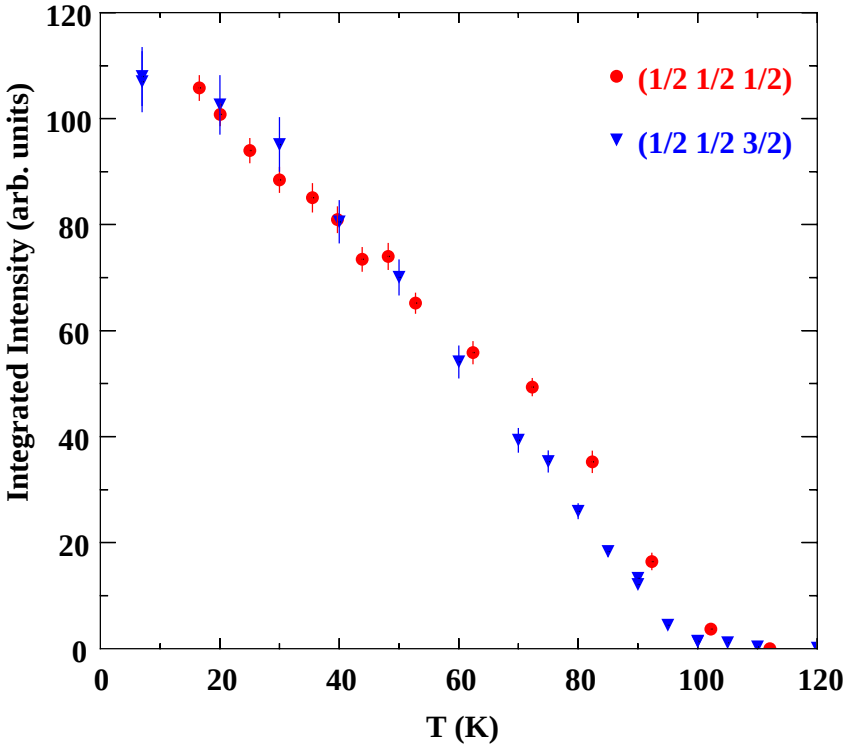

Figure 5.5: Temperature dependence of the integrated intensity of the magnetic reflections $(\frac{1}{2}\ \frac{1}{2}\ \frac{1}{2})$ and $(\frac{1}{2}\ \frac{1}{2}\ \frac{3}{2})$. The Néel temperature of about 102 K agrees with the one found by field cooled magnetization measurements.

nant reflections vanishes above the Néel temperature of 102 K (Fig. 5.5), in good agreement with the magnetization data (Figure 5.3).

The observation of resonant superstructure reflections at reciprocal space positions $(\frac{1}{2}\ \frac{1}{2}\ \frac{1}{2})$ and $(\frac{1}{2}\ \frac{1}{2}\ \frac{3}{2})$ indicates a doubling of the unit cell along all three crystallographic directions. This could either result from magnetic order confirming conclusions from neutron diffraction studies [89, 90] or from charge order, reflecting the different valence states of the ruthenium ion, for which there is independent evidence from from x-ray absorption [84], NMR [85, 86, 87] and FMR [88]. In order to distinguish the two scenarios, we have analyzed the polarization of the scattered signal at the $(\frac{1}{2}\ \frac{1}{2}\ \frac{1}{2})$ reflection, which was measured with an incident polarization perpendicular to the diffraction plane (σ-polarization). The polarization analysis has shown that the scattered intensity of the superstructure reflection originates entirely from scattering events in which the photon polarization is rotated ($\sigma \rightarrow \pi'$). No intensity above background was detected in the $\sigma \rightarrow \sigma'$ polarization channel. Since charge order does not rotate the polarization of the scattered photons, the observed superstructure reflections cannot result from this phenomenon. In contrast,

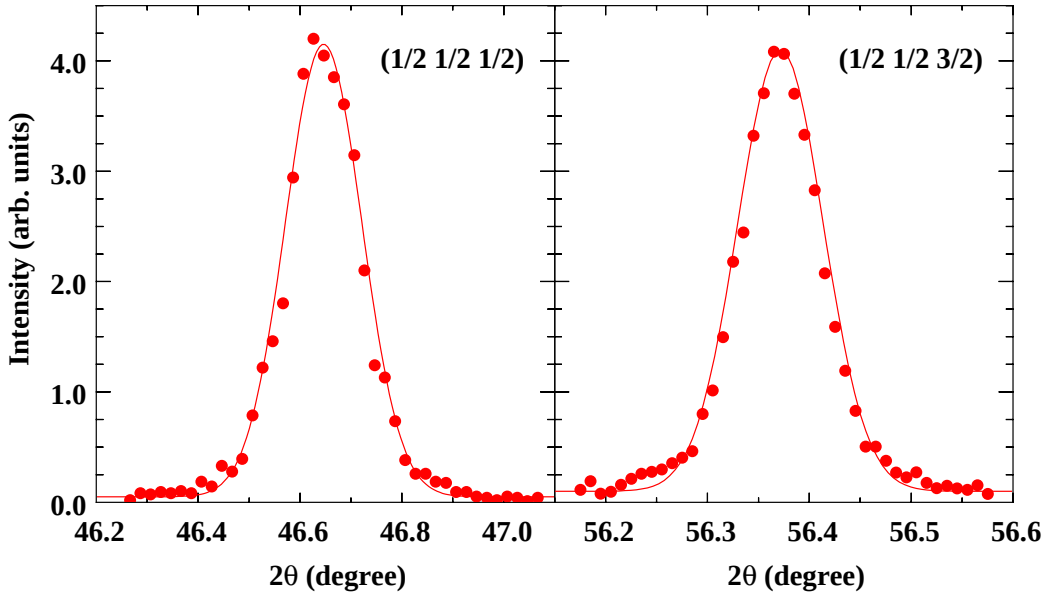

Figure 5.6: Typical longitudinal reciprocal space scans at the magnetic reflections $(\frac{1}{2}\ \frac{1}{2}\ \frac{1}{2})$ and $(\frac{1}{2}\ \frac{1}{2}\ \frac{3}{2})$. The HWHM of the scans leads to magnetic domain size of at least 500 Å .

the results support an interpretation in terms of G-type antiferromagnetic order, as suggested by neutron powder diffraction studies [89, 90].

Figure 5.6 shows typical reciprocal space scans at both magnetic reflections. The half width at half maximum (HWHM) of the scans is temperature independent up to 90 K and broadens above this temperature. Based on the HWHM of the scans the magnetic correlation length has been calculated according to Equation 4.9. This leads to a lower bound of 500 Å on the magnetic domain size in the RuO_2 planes.

In order to determine the direction of the magnetic moments, we rotated the sample around the scattering vector and measured the azimuthal dependence of the scattered intensity at the $(\frac{1}{2}\ \frac{1}{2}\ \frac{1}{2})$ reflection, which is shown in Figure 5.7. For a collinear antiferromagnet, the diffracted intensity is maximum, when the magnetic moment lies in the scattering plane. Hence, based on the neutron results one would expect to observe the maximum intensity when the c-axis lies in the diffraction plane. However, this is not case. Instead, the c-axis forms an angle of $53° \pm 3°$ with the maximum intensity position ($\psi = 0$), clearly indicating that the magnetic moment is not aligned along the c-axis. This deviation cannot be explained as a consequence of canting, as suggested by Jorgensen *et al.* [90]. Neither an antiferromagnetic alignment along the c-axis with a small ferromagnetic component in the ab-plane nor an antiferromagnetic alignment in the ab-plane with canting along c can reproduce both the intensity modulation of the azimuthal dependence and the experimentally observed angle between the c-axis and the maximum intensity position. However, these simulation constraints can be satisfied by a collinear antiferromagnetic struc-

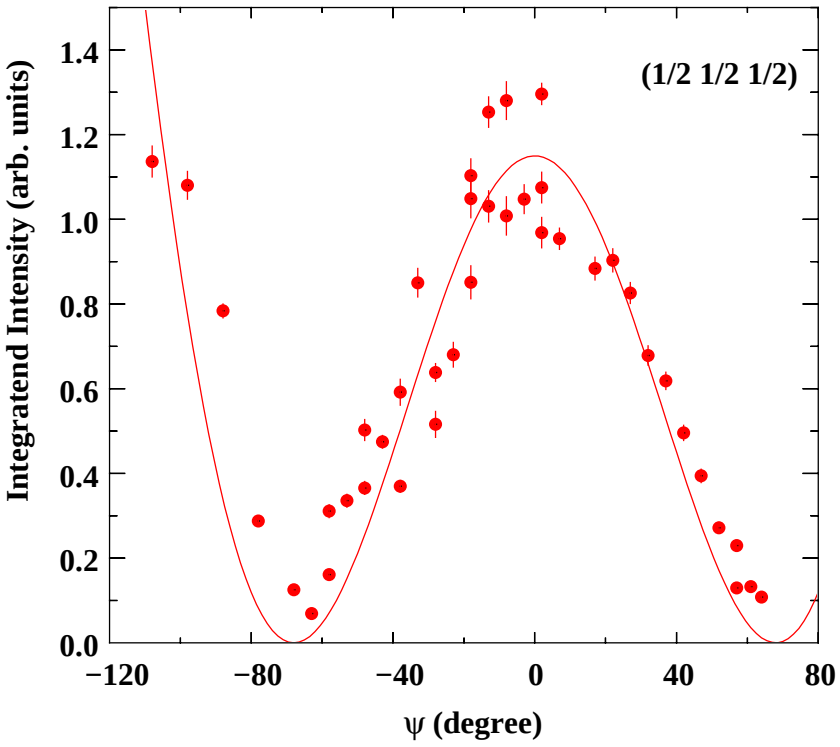

Figure 5.7: Azimuthal dependence of the integrated scattering intensity at reflection $(\frac{1}{2}\ \frac{1}{2}\ \frac{1}{2})$ at $T = 43$ K, where $\psi = 0$ is defined in such a way that (1 0 2) lies in the diffraction plane. The solid line is the result of a fit to a theoretical expression for the resonant electric dipole scattering intensity.

ture and a low symmetry magnetic moment direction. Following the approach of Hill and McMorrow [41] discussed in Chapter 2, the scattered intensity is given by

$$I^{\sigma\to\pi'}_{(\frac{1}{2}\ \frac{1}{2}\ \frac{1}{2})} \propto \left|\sin\alpha\ \cos\theta\ \cos(\psi-\psi_0)+\cos\alpha\ \sin\theta\right|^2, \tag{5.1}$$

where θ is the Bragg angle, ψ the azimuthal angle with offset ψ_0, and α the angle between the magnetic moment and the scattering vector. A detailed derivation of this expression can be found in the PhD thesis of I. Zegkinoglou [94]. The best simulation result was obtained for α =49°±1°. Together with the observed angle of 53°± 3° between the c-axis and the magnetic moment, this leads to an approximate direction of the magnetic moment along the (1 0 2) in reciprocal space, since $\angle\left((102),(111)\right) = 45.6°$ and $\angle\left((102),(001)\right) = 56°$. This moment direction, schematically shown in Figure 5.8, is also supported by the azimuthal dependence measured at the second magnetic reflection $(\frac{1}{2}\ \frac{1}{2}\ \frac{3}{2})$, which also exhibits maximum intensity when the (1 0 2) reflection lies in the scattering plane.

The direction of the magnetic moment deduced from our resonant x-ray diffraction

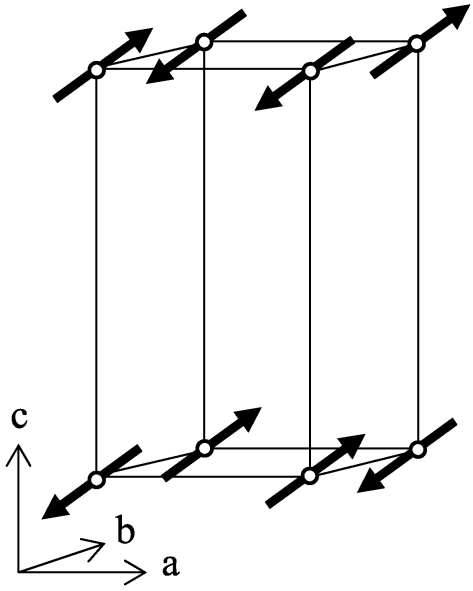

Figure 5.8: Schematic sketch of the magnetic structure of $RuSr_2GdCu_2O_8$. The magnetic moments lie along the (1 0 2) direction in reciprocal space.

data is consistent with the macroscopic susceptibility, which is reduced below the Néel temperature for magnetic fields applied both along and perpendicular to the *c*-axis (Figure 5.3). It is also interesting to compare our results to those of the neutron powder diffraction experiments. Based on the intensity ratio of the $(\frac{1}{2}\ \frac{1}{2}\ \frac{1}{2})$ and $(\frac{1}{2}\ \frac{1}{2}\ \frac{3}{2})$ reflections, the tentative conclusion was drawn that the magnetic moments are oriented along the *c*-axis [89]. By coincidence, the same ratio is derived for the moment direction inferred from our data (The calculation details are discussed in the PhD thesis of I. Zegkinoglou [94].). Hence, the results of neutron powder diffraction study are in full agreement with our experiment. On the other hand, the large in-plane component of the sublattice magnetization confirms conclusions from FMR and NMR experiments [85, 86, 87, 88].
In order to further assess the implications of our results, we have performed a representation analysis [95, 96] to check if the low symmetry direction of the magnetic moment is compatible with the orthorhombic space group *Pbam*, which has been identified recently by a crystallographic study [82, 83]. With respect to the tetragonal $P4/mmm$ unit cell, the orthorhombic unit cell is doubled and rotated by 45° in the *ab*-plane, as shown in Figure 5.9, due to the alternating rotation of the RuO_6 octahedra around the *c*-axis in the *ab*-plane. The representation analysis yields the basis functions $[-,-,F_z]$, $[-,-,A_z]$, $[A_x,F_y,-]$ and $[F_x,A_y,-]$, where F and A denote parallel and antiparallel alignment of the Ru moments in the Wyckoff position 2a of space group *Pbam* consisting of sites (0 0 0) and $(\frac{1}{2}\ \frac{1}{2}\ 0)$, respectively. In the orthorhombic notation, the magnetic moment deduced from our resonant x-ray diffraction study is aligned along the (1 1 2) direction in reciprocal space. Hence, in contrast to most magnetic insulators whose spin arrangements are described by a sin-

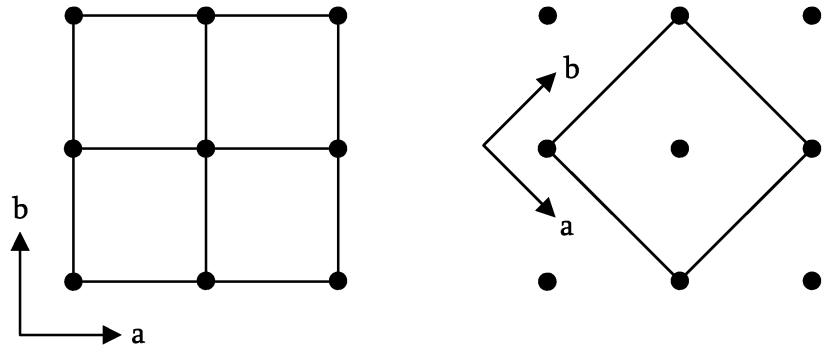

Figure 5.9: Comparision of the tetragonal $P4/mmm$ (left) and orthorhombic $Pbam$ (right) unit cells of $RuSr_2GdCu_2O_8$ in the ab-plane. The black spheres represent the Ru ions and the squares denote the unit cells.

gle irreducible representation, a combination of irreducible representations, namely $[-,-,A_z]$, $[A_x,F_y,-]$ and $[F_x,A_y,-]$, is needed to describe the observed magnetic sturcture. This might reflect structural distortions beyond those reported in the literature, or additional terms in the spin Hamiltonian, resulting from charge or orbital fluctuations in the RuO_2 layers, or from the proximity to the highly conducting CuO_2 bilayers. A similar effect was recently observed in insulating vanadates and tentatively attributed to orbital fluctuations [97].
The representation analysis reveals that a ferromagnetic in-plane component is required by symmetry to accompany the experimentally observed G-type antiferromagnetic structure due to the rotation of the RuO_6 octahedra which gives rise to a Dzyaloshinski-Moriya interaction. Interestingly, the propagation vector $(0\ 0\ \frac{1}{2})$ in $Pbam$ requires an alternation of the ferromagnetic moment along the c-axis. This mode corresponds precisely to the A-type antiferromagnetic structure deduced from FMR and NMR experiments [87, 88]. While the ferromagnetic component seems to be too small to be observed by resonant x-ray scattering and neutron powder diffraction, the pronounced upturn in the magnetization above the Néel temperature might be an indirect manifestation of it. Due to the antiferromagnetic interlayer exchange coupling, the weak ferromagnetic moment of each RuO_2 layer is compensated, as observed in other weak ferromagnets such as La_2CuO_4 [98]. Defects such as stacking faults [99] or structural distortions beyond $Pbam$ might then induce an uncompensated ferromagnetic moment observed in some (but not all) experiments [77, 78, 79].

5.4 Discussion

The broad coexistence range of superconductivity and long range magnetic order has motivated numerous investigations of $RuSr_2GdCu_2O_8$. However, as most studies were performed on powder samples the information on the magnetic structure was limited and to some extent even contradictory. In this situation, reso-

nant x-ray diffraction has turned out to be the ideal tool for the investigation of $RuSr_2GdCu_2O_8$ since it is sensitive to the magnetism and in contrast to single neutron diffraction does not depend on a large crystal mass.
Our resonant x-ray diffraction results indicate a *G*-type antiferromagnetic structure, consistent with the neutron powder diffraction data [89, 90]. However, the magnetic moment was not found to lie along the crystallographic *c*-axis as suggested by the neutron results, but along a low symmetry axis with substantial components parallel and perpendicular to the RuO_2 planes. A symmetry analysis in conjunction with a recent crystallographic study revealed that the experimentally observed *G*-type antiferromagnetic structure needs to be accompanied by an additional ferromagnetic in-plane component, which alternates between neighboring RuO_2 layers. Interestingly, this ferromagnetic mode corresponds exactly to the one inferred from NMR and FMR experiments [87, 88]. Therefore, our resonant x-ray diffraction data reconcile a variety of apparently contradictory findings on the magnetic structure of $RuSr_2GdCu_2O_8$ and thus resolve a big controversy in the experimental literature. Future work is required to assess the influence of the surprisingly complex magnetic structure on the superconducting properties of the CuO_2 layers.

Chapter 6

Magnetic structure of Mn substituted $Sr_3Ru_2O_7$

The Ruddlesden-Popper type $Sr_{n+1}Ru_nO_{3n+1}$ show a wide variety of interesting phenomena. $SrRuO_3$ is an itinerant ferromagnet with a Curie temperature of about 160 K [100], whereas Sr_2RuO_4 is a paramagnetic Fermi liquid and turns into an unconventional spin-triplet superconductor below 1.5 K [26, 101]. The bilayered compound $Sr_3Ru_2O_7$ has attracted a lot of interest in the past years due to the observation of quantum critical behavior related to a metamagnetic transition between two metallic phases [102]. The quantum criticality results from a critical end point, whose temperature is decreased as the direction of the magnetic field is varied [103, 104]. However, several aspects of the metamagnetic transition are still not understood, including the splitting of the metamagnetic transition, accompanied by the formation of a new phase, and the importance of anti- and ferromagnetic fluctuations for metamagnetism. To shed light on the role of magnetic fluctuations in $Sr_3Ru_2O_7$, the investigation of substitution effects is a useful tool, since chemical substitution helps to stabilize the fluctuations.

6.1 Properties of pure and Mn substituted $Sr_3Ru_2O_7$

The crystal structure of $Sr_3Ru_2O_7$ is shown in Figure 6.1. It consists of RuO_2 bilayers with corner sharing RuO_6 octahedra which are separated by SrO planes. Initially, the material was reported to have the tetragonal space group $I4/mmm$ with room temperature lattice parameters $a = b = 3.8903(6)$ Å and $c = 20.5520(5)$ Å [105]. However, later neutron diffraction studies revealed an alternating rotation of the RuO_6 octahedra by about 7 ° around the crystallographic c-axis [106, 107, 108, 109] reducing the Ru-O-Ru bond angle in the RuO_2 planes to 165 °. The resulting crystal structure is described by the orthorhombic space group $Bbcb$ with room temperature lattice parameters $a = b = 5.5006(4)$ Å and $c = 20.7225(1)$ Å [107]. Since the in-plane lattice constants are identical within experimental uncertainty, the distortions in $Sr_3Ru_2O_7$ seem to involve only pure rotations.

The electronic structure of $Sr_3Ru_2O_7$ near the Fermi level has been studied by

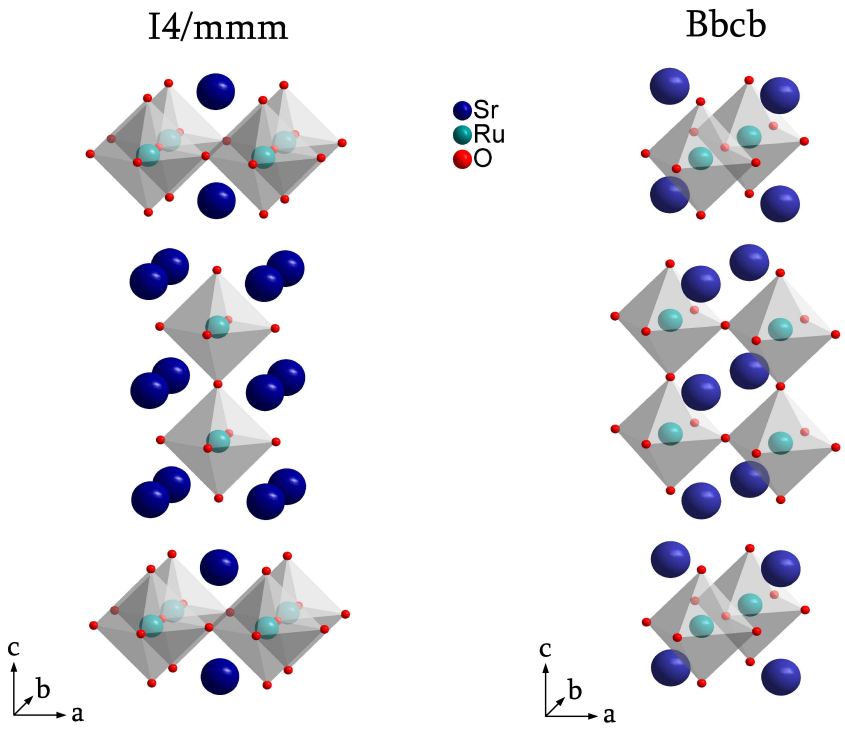

Figure 6.1: Crystal structure of $Sr_3Ru_2O_7$. It was initially reported to be tetragonal with space group $I4/mmm$ [105]. However, later studies revealed an alternating rotation of the RuO_6 octahedra in the RuO planes, which leads to the orthorhombic space group $Bbcb$ [107]. In the this setting, the unit cell is doubled and rotated by 45 ° in the ab-plane with respect to the tetragonal unit cell. For simplicity, some authors still use the tetragonal notation.

ARPES [110]. In combination with LDA based band structure calculations, which take spin-orbit coupling into account, it was possible to identify the orbital character of the experimentally observed Fermi surface pockets. According to the ARPES data, shown in Figure 6.2, the Fermi surface consists of six sheets, three of them are centered around the Γ point. The innermost pocket, labeled δ, has $d_{x^2-y^2}$ character. Hence, in contrast to Sr_2RuO_4 and $Ca_3Ru_2O_7$, the e_g-manifold is occupied. The other two pockets centered at Γ are holelike and composed of the d_{xz}- and d_{yz}-orbitals. The two Fermi sheets around the M point, labeled β and γ_1 are electron like. The β pocket has d_{xz}/d_{yz} character, the γ_1 has contributions from all three t_{2g}-orbitals. The small holelike pocket γ_2 barely touches the Fermi surface. Therefore, it is not clear if it really contributes to the Fermi surface of $Sr_3Ru_2O_7$. Since the cyclotron masses extracted from ARPES are in good agreement with the values determined by de Haas van Alphen data [111], the electronic structure of $Sr_3Ru_2O_7$ seen by ARPES resembles that of the bulk. Based on the ARPES results, the γ_1 and γ_2 sheets, which have a significant d_{xy} character, have a very high density of states near the Fermi surface including van Hove singularities. Since the

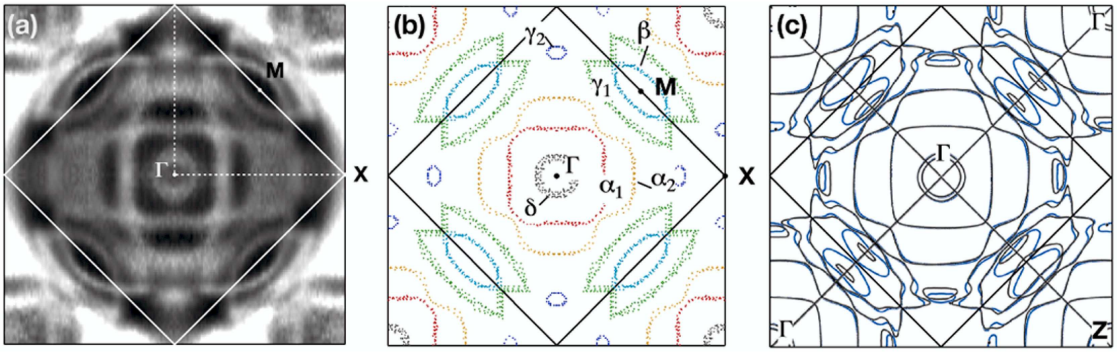

Figure 6.2: Fermi surface of $Sr_3Ru_2O_7$[110]. (a) shows the experimental ARPES data, (b) depicts the Fermi surface contours extracted from the experimental results and (c) shows the results of LDA calculations incorporating spin-orbit coupling for the basal plane ($k_z = 0$, black) and the midplane ($k_z = 1/4$, blue).

situation is qualitatively similar to the one discussed by Binz and Sigrist in the model of the metamagnetic transition [112], the two sheets might play an important role for the metamagnetic transition.

In the ground state, $Sr_3Ru_2O_7$ is a paramagnetic metal close to a ferromagnetic instability [113]. It exhibits Fermi liquid behavior below 10 K, characterized by a quadratic temperature dependence of the in-plane and out-of-plane electrical resistivity [113, 102]. The Fermi liquid state is very sensitive to disorder, thus its onset temperature depends strongly on the purity of the sample [114]. Upon the application of a magnetic field, a metamagnetic transition is induced at 5.5 T for $B \parallel ab$ [102] and at 7.8 T for $B \parallel c$ [103]. For $B \parallel ab$, metamagnetism coincides with a first order phase transition which terminates in a critical point at a finite temperature. As the magnetic field is rotated towards the c-axis, the temperature of the critical point is lowered, resulting in a quantum critical point for $B \parallel c$ [102, 103, 115]. In the vicinity of the quantum critical point, non Fermi liquid behavior has been observed by various experimental probes including resistivity [102, 103], specific heat [116] and thermal conductivity [117]. Interestingly, as the temperature is decreased below 1.2 K for $B \parallel c$, the metamagnetic transition splits into two first order transitions [118, 119], which indicate the boundaries of a new phase that masks the quantum critical point. This new phase is accompanied by a pronounced upturn in the electrical resistivity, which exhibits a strong in-plane anisotropy when the magnetic field has an additional in-plane component [120], as shown in Figure 6.3. When the magnetic field is applied in the ac-plane, the resistivity decreases along the b-axis, but remains unchanged along the a-axis. This resistivity behavior is reversed as the magnetic field is applied in the bc-plane. No evidences have been found for a formation of magnetic domains or for a structural phase transition that lowers the crystal symmetry. Thus, the new phase cannot be associated with a known phase and the observed anisotropic resistivity behavior cannot be explained in a conventional way. Therefore, the new phase has been named electronic nematic phase.

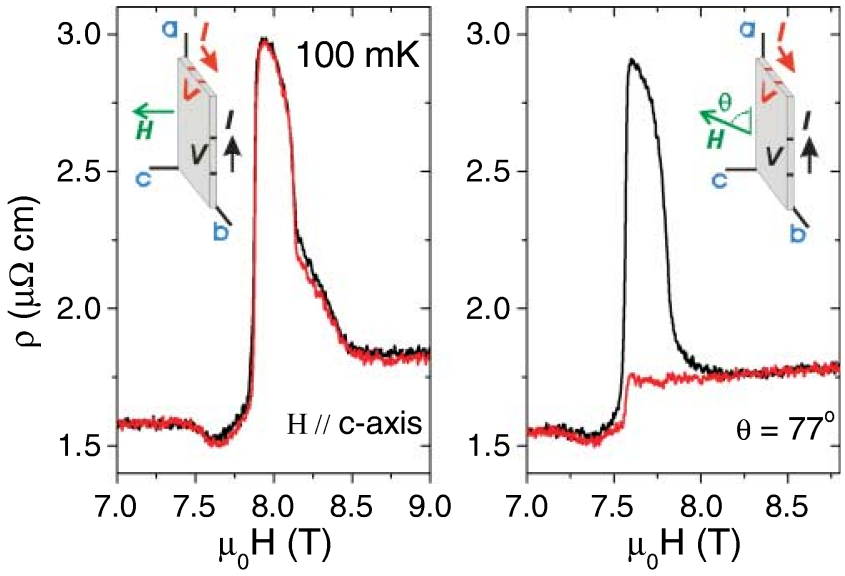

Figure 6.3: In-plane resistivity of $Sr_3Ru_2O_7$ [120]. For an applied magnetic field along the c-axis, the in-plane resistances ρ_{aa} and ρ_{bb} are identical. However, as the magnetic field is applied in the ac-plane, an anisotropy is observed, with the easy current flow direction along the b-axis, perpendicular to the external magnetic field. This behavior is inversed as the magnetic field is applied in the bc-plane.

Far from the electronic nematic phase, the behavior of $Sr_3Ru_2O_7$ is in qualitative agreement with the Stoner picture of itinerant electron metamagnetism [111, 117, 121, 122]. This immediately implies that the relevant excitations near the quantum critical point are ferromagnetic fluctuations. However, there is independent evidence from inelastic neutron diffraction [123], NMR [124, 125], and Hall measurements [126] that the magnetic fluctuations are indeed ferromagnetic above 20 K, but become predominantly antiferromagnetic as the temperature is decreased.

In order to shed light on the nature of the magnetic fluctuations in $Sr_3Ru_2O_7$, the investigation of substitution effects can be a useful tool, since chemical substitution helps to stabilize the fluctuations. In fact, a partial Mn substitution for Ru induces an insulating antiferromagnetic state above a Mn concentration of 5% [127]. The transition temperature of this phase is continuously shifted to higher temperatures as the Mn concentration is increased (Figure 6.4). Below the metal-insulator transition, two superstructure reflections are observed in the neutron powder diffraction pattern [127]. These are characteristic of long-range antiferromagnetic order and indicate an up-up-down-down spin arrangement in the RuO_2 planes, as schematically shown in Figure 6.5. The same antiferromagnetic structure has been observed in $HoMnO_3$ [128, 129]. In this material, the superexchange interaction between Mn next nearest neighbors in the MnO_2 layers is enhanced due to $GdFeO_3$-type distortions. In conjunction with orbital order, this leads to a spin frustration that causes the complex antiferromagnetic structure. A similar scenario might be realized in

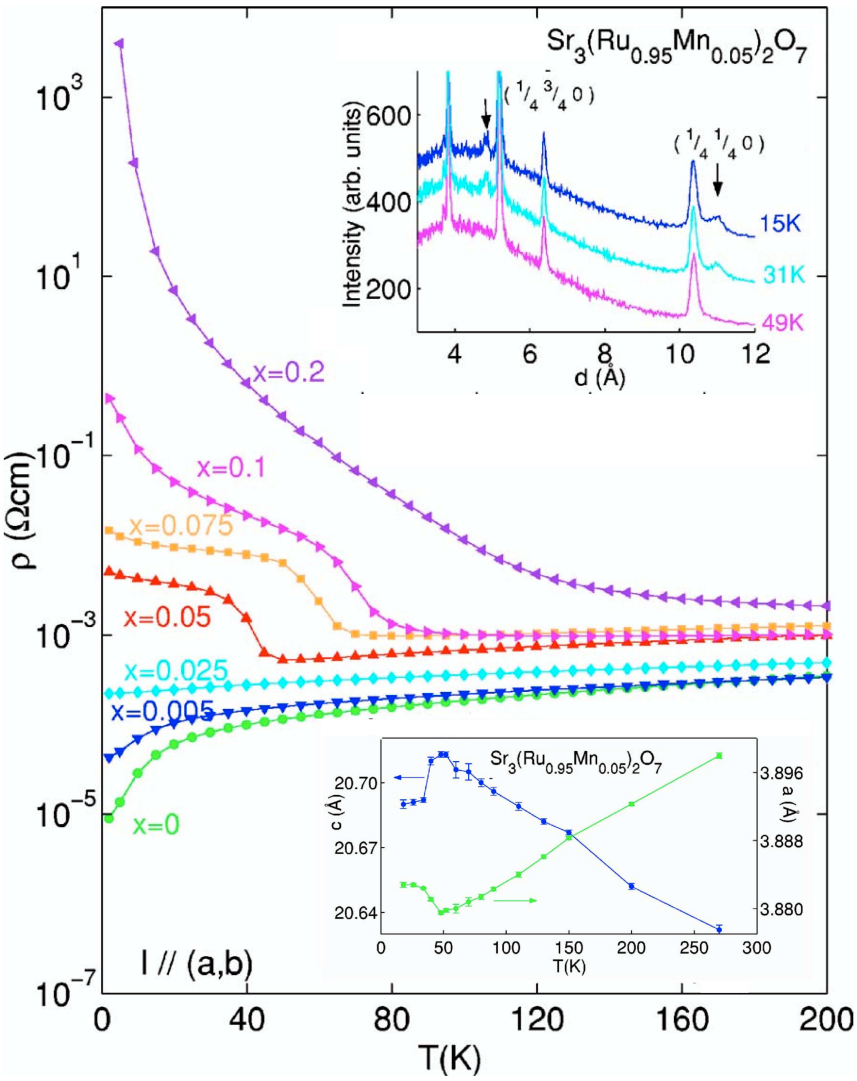

Figure 6.4: Temperature dependence of the in-plane resistivity of $Sr_3(Ru_{1-x}Mn_x)_2O_7$ as a function of Mn concentration x [127]. Upon 5% Mn substitution a metal-insulator transition is induced, which is shifted to higher temperatures as the Mn concentration is increased. The insets show data measured on 5% Mn substituted $Sr_3Ru_2O_7$. At the metal-insulator transition, two superstructure reflections occur in the powder neutron diffraction pattern (upper inset) and lattice parameters exhibit an anomaly (lower inset).

Mn substituted $Sr_3Ru_2O_7$. The complex magnetic structure might then reflect the existence of long-range orbital order.
To confirm the complex antiferromagnetic structure deduced from powder neutron diffraction, to determine the direction of the magnetic moment and to verify the existence of orbital order in Mn substituted $Sr_3Ru_2O_7$, single crystal diffraction studies are needed. In this context, resonant x-ray diffraction is especially suited since it is sensitive to both, magnetic and orbital order.

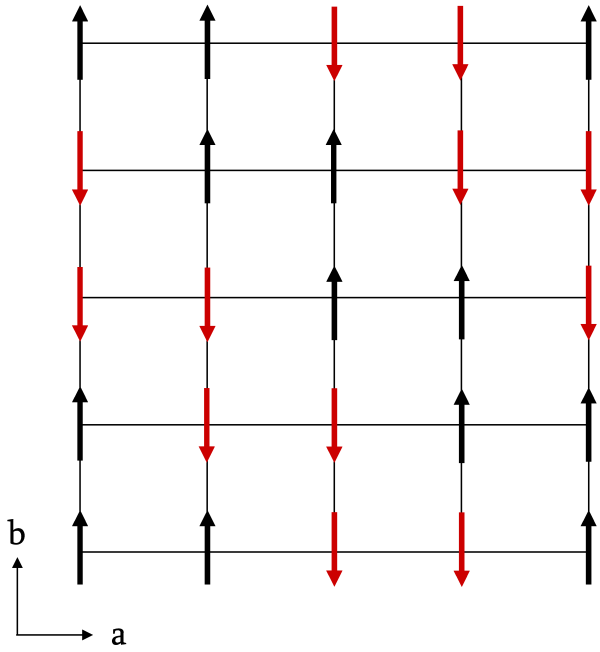

Figure 6.5: Schematic picture of the spin arrangement in the *ab*-plane in Mn substituted $Sr_3Ru_2O_7$ which is consistent with the observation of the superstructure reflections at $(\frac{1}{4}\ \frac{1}{4}\ 0)$ and $(\frac{1}{4}\ \frac{3}{4}\ 0)$. Based on the neutron powder diffraction results the magnetic moment direction cannot be determined.

6.2 Experimental Details

Single crystalline samples of $Sr_3(Ru_{1-x}Mn_x)_2O_7$ were grown by the floating zone method. Details on the growth technique and the crystal characterization have been given elsewhere [127, 130]. Since crystals with low Mn concentration are very fragile, we decided to carry out the experiments on 10% Mn substituted $Sr_3Ru_2O_7$. The investigated crystals easily cleave along the *ab*-plane and have typical dimensions of $4\times4\times1mm^3$. As shown in Figure 6.6, the rocking curves of the studied crystals have a full width at half maximum of less than 0.06° indicating a high crystal quality. The resonant x-ray diffraction studies at the Ru *L*-absorption edges were performed at beamline KMC1 of BESSY.

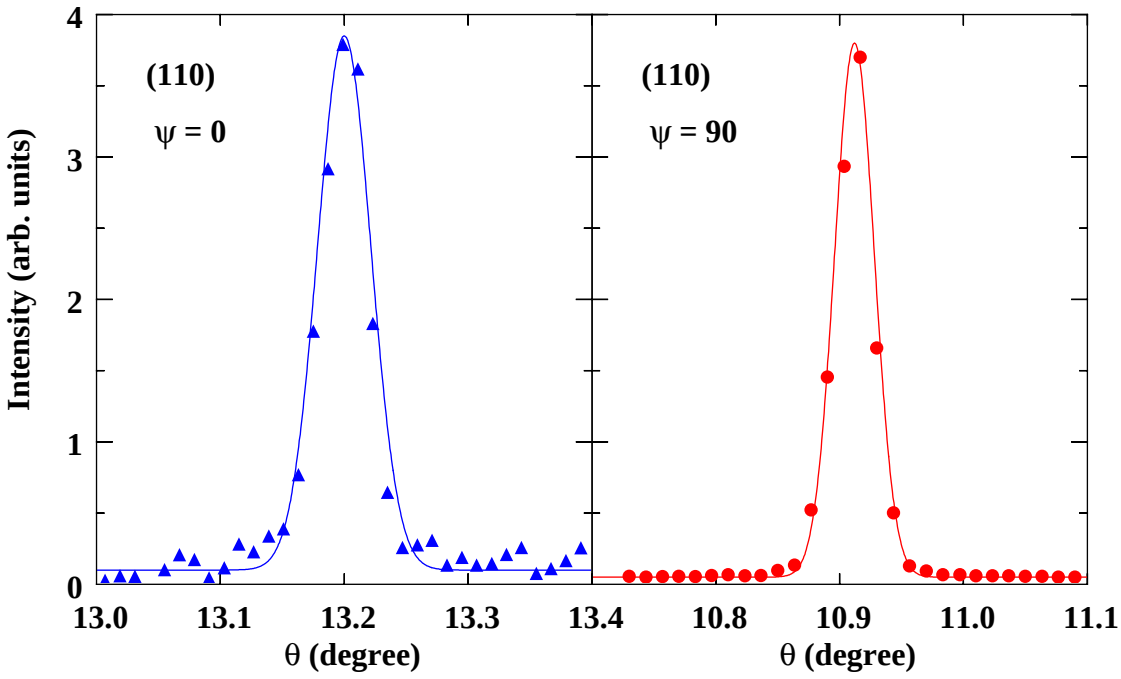

Figure 6.6: Rocking curves of a 10% Mn substituted $Sr_3Ru_2O_7$ crystal measured at the (110) crystallographic Bragg reflection with the *c*-axis parallel (ψ =0°) and perpendicular (ψ =90°) to the diffraction plane, respectively. The rocking curves have a full width at half maximum (FWHM) of less than 0.06° indicating a high crystal quality.

6.3 Magnetic Structure

Inspired by the results of a transport and neutron powder diffraction study on Mn substituted $Sr_3Ru_2O_7$ [127], which revealed the existence of an insulating antiferromagnetic state above a Mn concentration of 5%, we investigated the magnetic

structure of 10% Mn substituted $Sr_3Ru_2O_7$ using resonant x-ray diffraction. For simplicity, all reflections ($h\ k\ l$) are indexed in the tetragonal space group $I4/mmm$. The fluorescence corrected energy profiles of the magnetic superstructure reflections ($\frac{1}{4}\ \frac{1}{4}\ 0$) and ($\frac{3}{4}\ \frac{3}{4}\ 0$) measured near the Ru L-absorption edges are shown in Figure

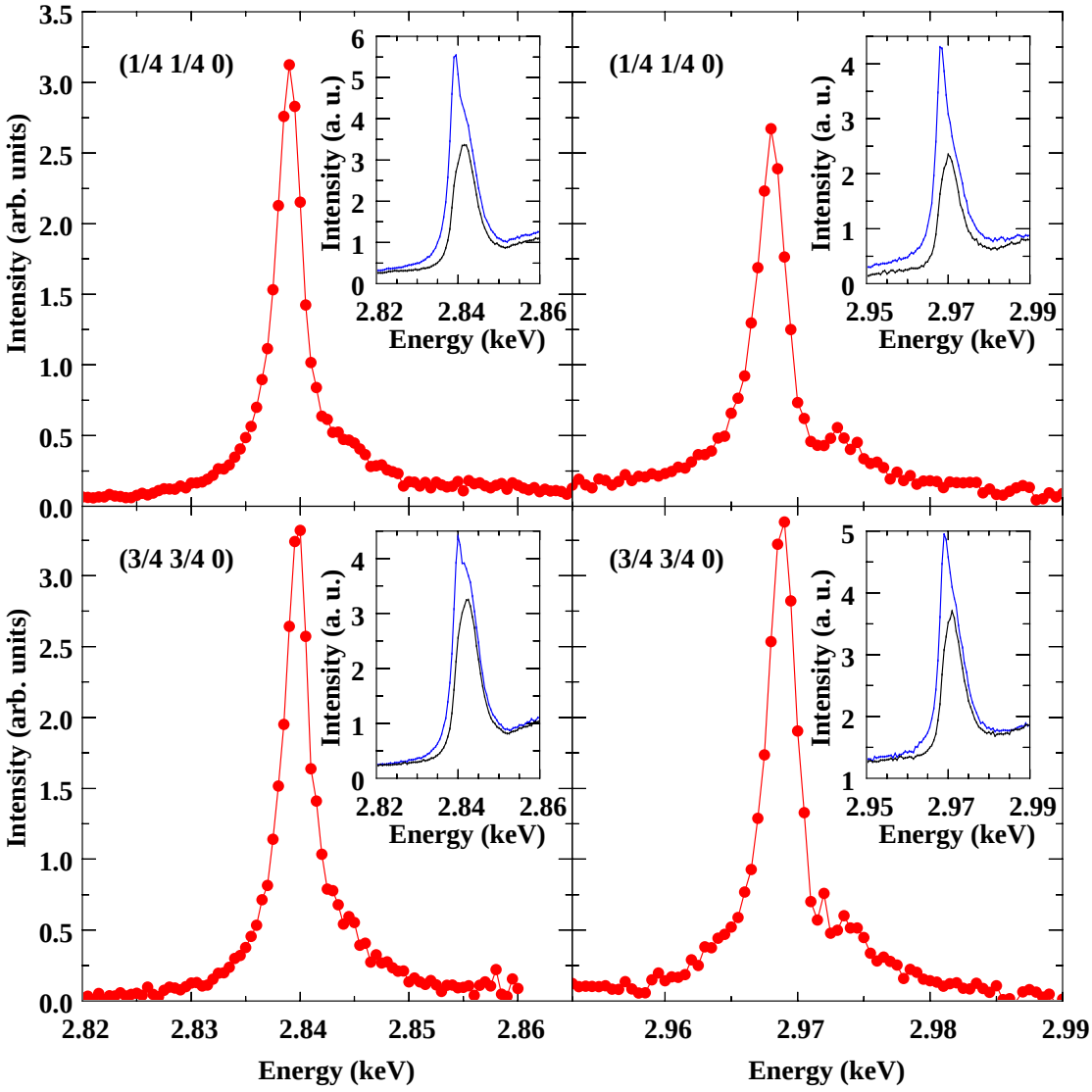

Figure 6.7: For fluorescence corrected energy profiles of the magnetic reflections ($\frac{1}{4}\ \frac{1}{4}\ 0$) and ($\frac{3}{4}\ \frac{3}{4}\ 0$) measured at 16 K at the Ru L-absorption edges of 10% Mn substituted $Sr_3Ru_2O_7$ with the c-axis perpendicular to the diffraction plane ($\psi = 90°$). The insets show the raw data including the energy scan at the particular reflection (blue) and the fluorescence scan (black), taken at an detector offset angle of 1°with respect to the one of the energy scan.

6.7. A moderate resonance enhancement is observed at both reflections resulting from electric dipole transitions from the $2p$ core level to the partially occupied $4d$ orbitals, responsible for magnetism. No off-resonant scattering has been detected above background.

In comparison with other ruthenates, such as the isostructural $Ca_3Ru_2O_7$ [131], the observed resonance enhancement is quite weak indicating that the magnetic order is less well established. To check this assumption, we determined the magnetic correlation length of both reflections from the HWHM of typical longitudinal reciprocal space scans according to Equation 4.9. The reciprocal space scans, displayed in Figure 6.8, have been fitted with Gaussian functions and have a HWHM of less than $0.2° = 0.0025$ rlu which corresponds to a magnetic domain size of 175 Å in the RuO_2 planes. It is also interesting to estimate the magnetic correlation length perpendicular to the RuO_2 layers, along the c-axis. To this end, we measured transversal reciprocal space scans (θ-scans) at various azimuthal positions of reflection $(\frac{1}{4}\ \frac{1}{4}\ 0)$. The azimuthal angle ψ describes the rotation of the sample around the scattering vector. At $\psi = 0°$, the c-axis lies in the scattering plane and a transversal θ-scan corresponds approximately to a l-scan. In contrast, at $\psi = 90°$, the ab-plane is parallel

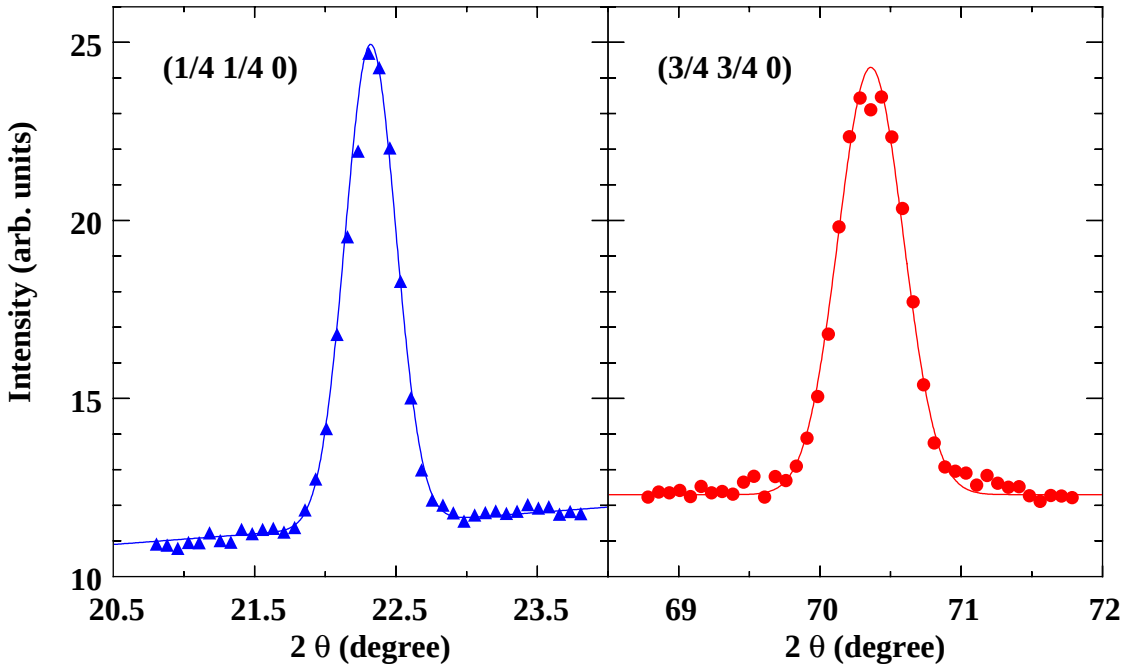

Figure 6.8: Typical longitudinal reciprocal space scans at the magnetic reflections $(\frac{1}{4}\ \frac{1}{4}\ 0)$ and $(\frac{3}{4}\ \frac{3}{4}\ 0)$ measured at the Ru L_2-absorption edge at 16 K. The scans have been fitted with Gaussian functions. From the half width at half maximum of the scans (HWHM) a correlation length of ≈175 Å has been deduced.

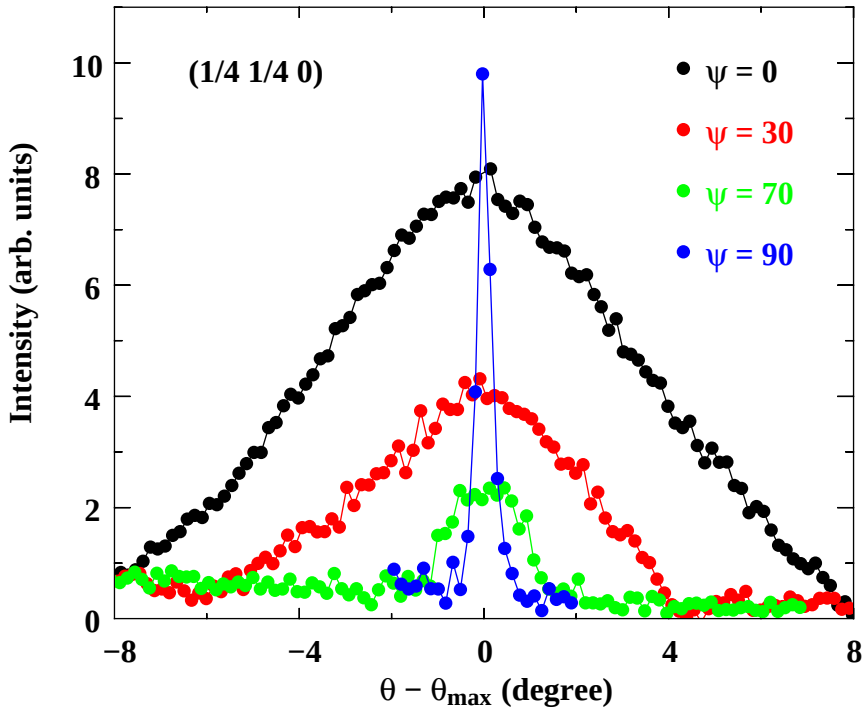

Figure 6.9: Transversal reciprocal space scans (θ-scans) at reflection ($\frac{1}{4}$ $\frac{1}{4}$ 0) taken at the Ru L_2-absorption edge at 16 K. For better comparison, the scans have been corrected for background and shifted to zero.

to the diffraction plane and a transversal θ-scan corresponds approximately to a $h\bar{k}$-scan. Figure 6.9 shows transversal reciprocal space scans of reflection ($\frac{1}{4}$ $\frac{1}{4}$ 0) taken at various azimuthal angles. For better comparison, each scan has been corrected for background and has been shifted to zero. The HWHM of the peaks broadens dramatically as the azimuth is changed from $\psi = 90°$ to $\psi = 0°$, indicating a much smaller correlation length perpendicular to the RuO_2 planes than parallel to them. In fact, the HWHM of the transversal scan of about 2° at $\psi = 0°$ translates into a c-axis correlation length of roughly 20 Å which corresponds to one unit cell. Hence, the magnetic order in Mn substituted $Sr_3Ru_2O_7$ is essentially two-dimensional. Together with the small magnetic domain size in the RuO_2 planes, this causes the moderate resonance enhancement of the magnetic signal compared to other ruthenates.

In addition to the investigation of the magnetic signal at reflections ($\frac{1}{4}$ $\frac{1}{4}$ 0) and ($\frac{3}{4}$ $\frac{3}{4}$ 0), we also searched for a resonance signal at reciprocal space position ($\frac{1}{2}$ $\frac{1}{2}$ 0). A resonance intensity at this wave vector would either indicate orbital order or a magnetic structure less complex than the proposed up-up-down-down antiferromagnetic structure, for instance an up-down spin arrangement in the RuO_2 planes. The

two scenarios could then be distinguished by a polarization analysis of the scattered signal and by the investigation of the azimuthal dependence of the integrated intensity. However, we did not detect any resonance signal above background. In combination with a previous powder neutron diffraction study of 5% Mn substituted $Sr_3Ru_2O_7$ [127], which revealed magnetic intensity at wave vectors $(\frac{1}{4}\ \frac{1}{4}\ 0)$ and $(\frac{1}{4}\ \frac{3}{4}\ 0)$, this result clearly rules out antiferromagnetic structures with a less complex spin arrangement, and thus supports the up-up-down-down antiferromagnetic structure, shown in Figure 6.5. Nevertheless, a single crystal neutron diffraction investigation with a complete magnetic structure refinement is needed to confirm this complex spin arrangement. As far as orbital order is concerned, it might be too weak to be detected since the orbital signal is expected to be at least one order of magnitude weaker than the magnetic signal [75], whose resonant enhancement is already quite small as discussed above.

In order to determine the direction of the magnetic moment, we measured the azimuthal dependence of the integrated intensity of the transversal reciprocal space scans at reflections $(\frac{1}{4}\ \frac{1}{4}\ 0)$ and $(\frac{3}{4}\ \frac{3}{4}\ 0)$. These studies were carried out in a horizontal scattering geometry, thus the incident beam was polarized parallel to the diffraction plane (π-polarization) and the diffracted beam contained polarization components perpendicular (σ') and parallel (π') to the scattering plane. The azimuthal dependence of the integrated intensity at both reflections is shown in Figure 6.10. For both wave vectors, it exhibits a maximum when the c-axis lies in the scattering plane ($\psi = 0°$) indicating a magnetic moment orientation along the c-axis. Therefore, the total scattering intensity at both reciprocal space positions has been calculated as a function of azimuthal angle based on this moment direction and the up-up-down-down antiferromagnetic structure (Figure 6.5) using the approach of Hill and McMorrow [41]. According to Equation 2.1 and 2.15, the intensity in the $\pi\sigma'$-channel at reflection $(q\ q\ 0)$ with $q = \frac{1}{4}$ or $q = \frac{3}{4}$ is given by

$$
\begin{aligned}
I^{\pi\sigma'}(q\,q\,0) &\propto \Big| \sum_{\mathbf{R}_j} e^{i(q\,q\,0)\boldsymbol{R}_j} f^{\pi\sigma'}_{\uparrow,\downarrow} \Big|^2 \\
&\propto \Big| f^{\pi\sigma'}_{\uparrow} - f^{\pi\sigma'}_{\downarrow} \Big|^2 \\
&= \Big| -iF^{(1)}(m_x\cos\theta + m_z\sin\theta) + F^{(2)}m_y(m_x\sin\theta - m_z\cos\theta) \\
&\quad - \big(-iF^{(1)}(-m_x\cos\theta - m_z\sin\theta) - F^{(2)}m_y(-m_x\sin\theta + m_z\cos\theta)\big) \Big|^2 \\
&= 4\ \big|F^{(1)}(m_x\cos\theta + m_z\sin\theta)\big|^2 \\
&= 4\ F^{(1)2}\ |(\cos\theta\sin\alpha\cos\psi - \sin\theta\cos\alpha)|^2 \\
&= 4\ F^{(1)2}\cos^2\theta\cos^2\psi, \qquad (6.1)
\end{aligned}
$$

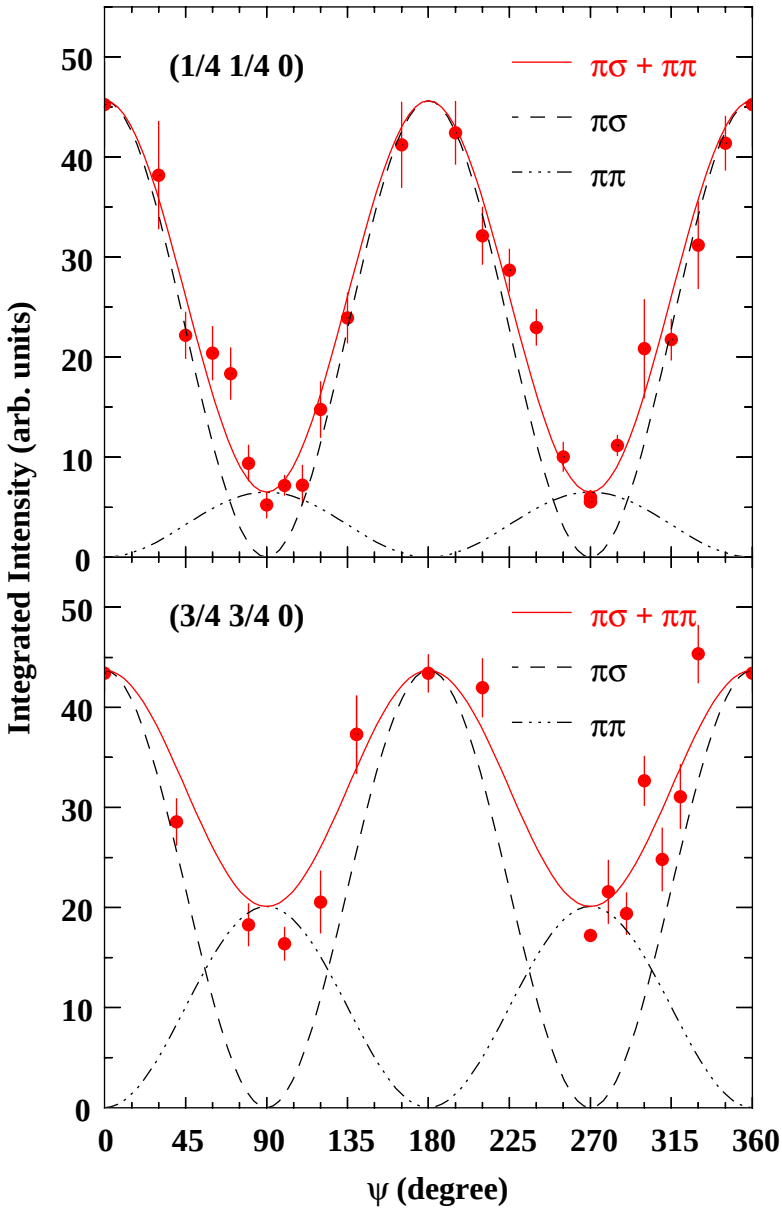

Figure 6.10: Azimuthal dependence of the integrated intensity of the transversal reciprocal space scans at reflections $(\frac{1}{4}\ \frac{1}{4}\ 0)$ and $(\frac{3}{4}\ \frac{3}{4}\ 0)$ measured at the Ru L_2-absorption edge at 16 K. The red solid lines are fits to the experimental results according to the expression for the resonant electric dipole scattering intensity, as explained in the text.

where $f_\uparrow$ and $f_\downarrow$ are the resonant scattering amplitude of a spin-up and a spin-down ion, respectively. θ denotes the scattering angle ($\theta_{(\frac{1}{4}\ \frac{1}{4}\ 0)} = 10.91\,°$; $\theta_{(\frac{1}{4}\ \frac{1}{4}\ 0)} = 34.75\,°$) and α represents the angle between the magnetic moment and the scattering vector

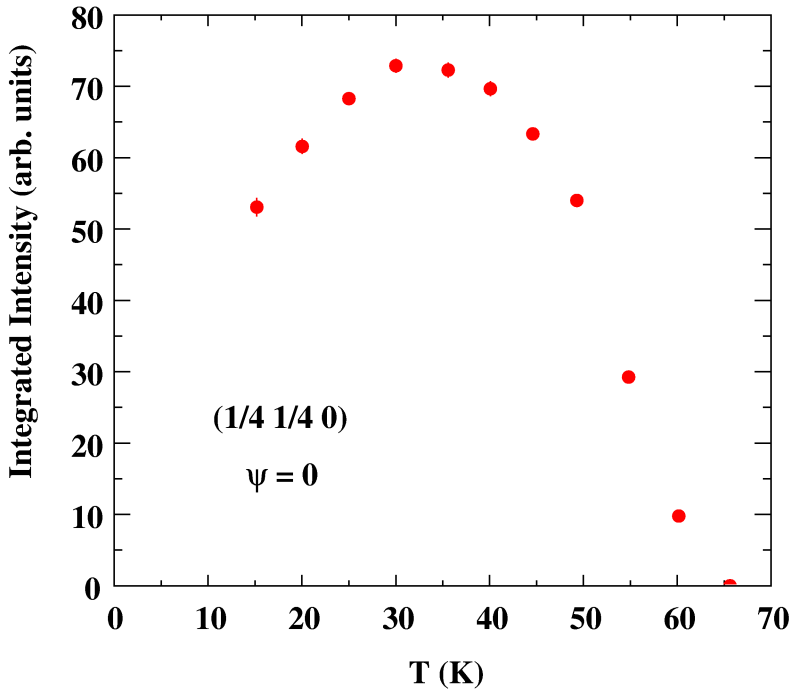

Figure 6.11: Temperature dependence of the integrated intensity of the magnetic reflection ($\frac{1}{4}$ $\frac{1}{4}$ 0) measured at the Ru L_2-absorption edge with the c-axis in the scattering plane ($\psi = 0°$).

($\alpha = 90°$). The diffracted intensity in the $\pi\pi'$-channel is calculated as

$$\begin{aligned} I^{\pi\pi'}(q\,q\,0) &\propto \left| f_{\uparrow}^{\pi\pi'} - f_{\downarrow}^{\pi\pi'} \right|^2 \\ &= \Big| F^{(0)} \cos 2\theta + iF^{(1)} m_y \sin 2\theta - F^{(2)} \cos^2\theta (m_x^2 \tan^2\theta + m_z^2) \\ &\quad - \left(F^{(0)} \cos 2\theta - iF^{(1)} m_y \sin 2\theta - F^{(2)} \cos^2\theta (m_x^2 \tan^2\theta + m_z^2) \right) \Big|^2 \\ &= 4 \left| F^{(1)} m_y \sin 2\theta \right|^2 \\ &= 4\, F^{(1)2} \left| \sin 2\theta \sin\alpha \sin\psi \right|^2 \\ &= 4\, F^{(1)2} \sin^2 2\theta \sin^2\psi. \end{aligned} \tag{6.2}$$

The total intensity is given by

$$I^{total}(q\,q\,0) = I^{\pi\sigma'}(q\,q\,0) + \cos 2\theta\; I^{\pi\pi'}(q\,q\,0), \tag{6.3}$$

where the signal of the $\pi\pi'$-channel has been multiplied by $\cos 2\theta$ to correct for the signal attenuation as the Brewster angle is approached. The simulation results are shown as red solid lines in Figure 6.10. Due to the different scattering angle at the

two reflections, the signal ratios of the $\pi\sigma'$- and $\pi\pi'$-channel are not identical for both reflections and therefore cause the different intensity modulation observed in the experiment. The simulation results are in good agreement with the experimental data and thus confirm, that the Ru moments are aligned along the crystallographic c-axis, perpendicular to the RuO_2 layers.
The temperature dependence of the magnetic signal at reflection $(\frac{1}{4}\ \frac{1}{4}\ 0)$ is shown in Figure 6.11. Antiferromagnetic order is established at about 65 K, which coincides with the metal-insulator transition (see Figure 6.4). Interestingly, the magnetic intensity does not saturate at low temperatures, but exhibits a maximum at about 30 K and decreases again below this temperature. This behavior is probably due to the interaction of the Ru spins with the Mn spins, which also participate in the up-up-down-down spin arrangement and exhibit the same magnetic moment direction as the Ru spins as revealed by a resonant x-ray diffraction study at the Mn L-absorption edges [132], which focused on the investigation of the superstructure reflection $(\frac{1}{4}\ \frac{1}{4}\ 0)$.

6.4 Discussion

Our resonant x-ray diffraction studies at the Ru L-absorption edges of 10% Mn substituted $Sr_3Ru_2O_7$ were focused on the investigation of the magnetic reflections $(\frac{1}{4}\ \frac{1}{4}\ 0)$ and $(\frac{3}{4}\ \frac{3}{4}\ 0)$. Based on the determination of the magnetic correlation length parallel and perpendicular to the RuO_2 layers, it has been shown that the magnetic order is essentially two dimensional. In conjunction with the small magnetic domain size in the RuO_2 planes, this is responsible for the moderate resonance enhancement of the signal observed in the experiment.
The observation of the $(\frac{1}{4}\ \frac{1}{4}\ 0)$ and $(\frac{3}{4}\ \frac{3}{4}\ 0)$ reflections and the absence of the $(\frac{1}{2}\ \frac{1}{2}\ 0)$ reflection are consistent with the up-up-down-down spin structure suggested by a previous neutron powder diffraction study [127]. Since the latter has been carried out on 5% Mn substituted $Sr_3Ru_2O_7$, the magnetic structure seems to be independent of the Mn concentration. This indicates that an antiferromagnetic instability is already present in the parent compound $Sr_3Ru_2O_7$ and is stabilized by the partial substitution of Ru by Mn.
Based on the azimuthal dependences of the magnetic signal at the $(\frac{1}{4}\ \frac{1}{4}\ 0)$ and $(\frac{3}{4}\ \frac{3}{4}\ 0)$ reflections, we deduced a magnetic moment direction along the crystallographic c-axis. These findings, concerning both the magnetic structure and the orientation of the magnetic moment, are in full agreement with the results of a resonant x-ray diffraction study of 5% and 10% Mn substituted $Sr_3Ru_2O_7$ carried out at the Mn L-absorption edges [132], suggesting that Mn ions also participate in the magnetic order.
Instead of partially substituting Mn for Ru, it might also be possible to induce the exotic up-up-down-down spin state by the application of a magnetic field. Considering the orientation of the magnetic moments, a magnetic field along the c-axis seems to be best suited for this purpose. In the orthorhombic notation, which is usually

used for $Sr_3Ru_2O_7$, an anisotropic resistivity behavior is then expected between the a- and b-axis, since the spins are aligned ferromagnetically in one and antiferromagnetically in the other direction. However, due to the formation of magnetic domains in the RuO_2 planes, there should be no macroscopic resistivity difference between the two directions. This scenario might actually be realized in the nematic phase of $Sr_3Ru_2O_7$ for $B \parallel c$. The application of an additional in-plane field might then cause the selection of one domain type and thus lead to the observed resistivity anisotropy, which would be entirely due to the different spin couplings along the a- and b-axis. In order to prove this speculative assumption, the existence of magnetism in the nematic phase has to be verified, and it needs to be checked, if the magnetic structure in fact corresponds to the exotic up-up-down-down spin arrangement observed in Mn substituted $Sr_3Ru_2O_7$. These issues can be best addressed by a single crystal neutron diffraction study including a complete structure refinement.

Chapter 7

Summary

The magnetic and orbital properties of the ruthenium oxides $Ca_3Ru_2O_7$ and Mn doped $Sr_3Ru_2O_7$ and the ruthenocuprate $RuSr_2GdCu_2O_8$ were investigated using resonant and high-energy x-ray diffraction.
Bilayered $Ca_3Ru_2O_7$ is a paramagnetic metal at high temperatures and orders antiferromagnetically at $T_N = 56\,\mathrm{K}$. A second phase transition to a less conductive state is observed at $T_{MI} = 48\,\mathrm{K}$. This transition is accompanied by abrupt structural changes and a reorientation of the magnetic moment. In addition, there is experimental evidence for the existence of orbital order below T_{MI}. Our resonant x-ray diffraction studies at the Ru L-absorption edges were focused on the investigation of the magnetic reflections (001) and (110). The observation of a magnetic signal at these reciprocal space positions is in full agreement with an A-type antiferromagnetic structure, consisting of ferromagnetic bilayers coupled antiferromagnetically along the c-axis. Based on the azimuthal angle dependence of the signals, the direction of the magnetic moment was determined to lie along the b-axis below T_{MI} and along the a-axis between T_{MI} and T_N. The origin of the reorientation of the magnetic moment at T_{MI} is not yet completely understood. However, it might result from the strong spin-orbit coupling which presumably causes an unquenched orbital magnetization. The latter might then induce additional terms in the spin Hamiltonian that are responsible for the reorientation of the magnetic moment. Although various experiments have given indirect evidence of orbital order below T_{MI}, we did not detect any orbital signal within the experimental sensitivity. This indicates that the orbital ordering parameter is significantly weaker than in the single layered counterpart Ca_2RuO_4, which is presumably due to residual charge or orbital fluctuations in the insulating state.
$RuSr_2GdCu_2O_8$ has attracted tremendous scientific interest in recent years due to the broad coexistence range of long range magnetic order and superconductivity, which makes it an ideal compound to study the interplay between these phenomena. However, limited information about the magnetic structure has been available so far, as most studies were performed on powder samples due to the small size of available crystals. In this situation, resonant x-ray diffraction at the Ru L-absorption edges has turned out to be the ideal tool for the investigation of $RuSr_2GdCu_2O_8$ since it

is sensitive to magnetism, but does not depend on a large crystal mass. Our single crystal studies of the magnetic reflections $(\frac{1}{2}\ \frac{1}{2}\ \frac{1}{2})$ and $(\frac{1}{2}\ \frac{1}{2}\ \frac{3}{2})$ indicate a G-type antiferromagnetic structure, characterized by a doubling of the unit cell along all three crystallographic directions. From the azimuthal angle dependence of the magnetic signal, we deduced a magnetic moment direction along a low symmetry axis with substantial components parallel and perpendicular to the RuO_2 planes. These findings are consistent with previous neutron powder diffraction results and magnetization data. A symmetry analysis in conjunction with a recent crystallographic study revealed that the experimentally observed G-type antiferromagnetic structure needs to be accompanied by an additional ferromagnetic in-plane component, which alternates between neighboring RuO_2 layers. This ferromagnetic mode corresponds exactly to the one deduced from nuclear and ferromagnetic resonance experiments. Therefore, our resonant x-ray diffraction data reconcile a variety of apparently contradictory results on the magnetic structure of $RuSr_2GdCu_2O_8$ and thus resolve a big controversy in the experimental literature.

Bilayered $Sr_3Ru_2O_7$ has attracted a lot of interest in the past years due to the observation of the quantum critical behavior which is related to a metamagnetic transition. In the ground state, the material is a paramagnetic metal and shows Fermi liquid behavior below 10 K. Upon substituting Mn for Ru, an insulating antiferromagnetic state is induced; its transition temperature varies with the Mn concentration. Using resonant x-ray diffraction at the Ru L-absorption edges, we investigated the antiferromagnetic structure of 10% Mn substituted $Sr_3Ru_2O_7$. Our studies of the superstructure reflections $(\frac{1}{4}\ \frac{1}{4}\ 0)$ and $(\frac{3}{4}\ \frac{3}{4}\ 0)$ indicate that the magnetic order is essentially two dimensional and that the magnetic moments are aligned along the c-axis. In combination with a previous neutron powder diffraction study, which was carried out on 5% Mn substituted $Sr_3Ru_2O_7$, our results suggest an up-up-down-down spin arrangement in the RuO_2 planes, which is independent of the Mn concentration. This implies that an antiferromagnetic instability is already present in the parent compound $Sr_3Ru_2O_7$. Interestingly, the anisotropic resistivity behavior, observed in the nematic phase of $Sr_3Ru_2O_7$, could be explained assuming the same up-up-down-down spin arrangement as in Mn substituted $Sr_3Ru_2O_7$. If the two phases are in fact identical, has to be checked by a detailed single crystal neutron diffraction study including a complete structure refinement.

Bibliography

[1] P. A. Cox, *Transition Metal Oxides* (Oxford University Press, 1992).

[2] S. Maekawa, T. Tohyama, S. E. Barnes, S. Ishihara, W. Koshibae, and G. Khaliullin, *Physics of Transition Metal Oxides* (Springer, 2004).

[3] Z. Fang, N. Nagaosa, and K. Terakura, Phys. Rev. B **69**, 045116 (2004).

[4] H. A. Jahn and E. Teller, Phys. Rev. **49**, 874 (1936).

[5] T. Oguchi, Phys. Rev. B **51**, 1385 (1995).

[6] D. J. Singh, Phys. Rev. B **52**, 1358 (1995).

[7] A. P. Mackenzie, S. R. Julien, A. J. Diver, G. J. McMullan, M. P. Ray, G. G. Lonzarich, Y. Maeno, S. Nishizaki, and T. Fujita, Phys. Rev. Lett. **76**, 3786 (1996).

[8] C. Bergemann, S. R. Julian, A. P. Mackenzie, S. NishiZaki, and Y. Maeno, Phys. Rev. Lett. **84**, 2662 (2000).

[9] E. Ohmichi, H. Adachi, Y. Mori, Y. Maeno, T. Ishiguro, and T. Oguchi, Phys. Rev. B **59**, 7263 (1999).

[10] A. Damascelli, D. H. Lu, K. M. Shen, N. P. Armitage, F. Ronning, D. L. Feng, C. Kim, Z.-X. Shen, T. Kimura, Y. Tokura, Z. Q. Mao, and Y. Maeno, Phys. Rev. Lett. **85**, 5194 (2000).

[11] M. W. Haverkort, I. S. Elfimov, L. H. Tjeng, G. A. Sawatzky, and A. Damascelli, Phys. Rev. Lett. **101**, 026406 (2008).

[12] K. Yosida, *Theory of Magnetism* (Springer, 1998).

[13] J. Hubbard, Proc. Roy. Soc. **A276**, 238 (1963).

[14] P. Fazekas, *Lecture notes on electron correlation and magnetism* (World Scientific, 1999).

[15] J. B. Goodenough, J. Phys. Chem. Solids **6**, 287 (1958).

[16] J. Kanamori, J. Phys. Chem. Solids **10**, 87 (1959).

[17] I. Dzyaloshinsky, J. Phys. Chem. Solids **4**, 241 (1958).

[18] T. Moriya, Phys. Rev. **120**, 92 (1960).

[19] J. G. Bednorz and K. A. Müller, Z. Phys. B **64**, 189 (1986).

[20] J. Orenstein and A. J. Millis, Science **288**, 468 (2000).

[21] J. Bardeen, L. N. Cooper, and J. R. Schrieffer, Phys. Rev. **108**, 1157 (1957).

[22] P. W. Andersen, Science **235**, 1196 (1987).

[23] J. M. Tranquada, B. J. Sternlieb, J. D. Axe, Y. Nakamura, and S. Ushida, Nature **375**, 561 (1995).

[24] J. M. Tranquada, J. D. Axe, N. Ichikawa, A. R.Moodenbaugh, Y. Nakamura, and S. Uchida, Phys. Rev. Lett. **78**, 338 (1997).

[25] K. Yamada, C. H. Lee, K. Kurahashi, J. Wada, S. Wakimoto, S. Ueki, H. Kimura, Y. Endoh, S. Hosoya, G. Shirane, R. J. Birgeneau, M. Greven, M. A. Kastner, and Y. J. Kim, Phys. Rev. B **57**, 6165 (1998).

[26] Y. Maeno, H. Hashimoto, K. Yoshida, S. Nishizaki, T. Fujita, J. G. Bednorz, and F. Lichtenberg, Nature (London) **372**, 532 (1994).

[27] T. M. Rice and M. Sigrist, J. Phys.: Condens. Matter **7**, L643 (1995).

[28] G. Baskaran, Physica B **223-224**, 490 (1996).

[29] K. Ishida, Y. Kitaoka, K. Asayama, S. Ikeda, S. Nishizaki, Y. Maeno, K. Yoshida, and T. Fujita, Phys. Rev. B **56**, R505 (1997).

[30] A. P. Mackenzie, R. K. W. Haselwimmer, A. W. Tyler, G. G. Lonzarich, Y. Mori, S. Nishizaki, and Y. Maeno, Phys. Rev. Lett. **80**, 161 (1998).

[31] K. Ishida, H. Mukuda, Y. Kitaoka, K. Asayama, Z. Q. Mao, Y. Mori, and Y. Maeno, Nature **396**, 658 (1998).

[32] G. M. Luke, Y. Fudamoto, K. M. Kojima, M. I. Larkin, J. Merrin, B. Nachumi, Y. J. Uemura, Y. Maeno, Z. Q. Mao, Y. Mori, H. Nakamura, and M. Sigrist, Nature **394**, 558 (1998).

[33] S. NishiZaki, Y. Maeno, and Z. Mao, J. Low Temp. Phys. **117**, 1581 (1999).

[34] K. Ishida, H. Mukuda, Y. Kitaoka, Z. Q. Mao, Y. Mori, and Y. Maeno, Phys. Rev. Lett. **84**, 5387 (2000).

[35] K. Izawa, H. Takahashi, H. Yamaguchi, Y. Matsuda, M. Suzuki, T. Sasaki, T. Fukase, Y. Yoshida, R. Settai, and Y. Onuki, Phys. Rev. Lett. **86**, 2653 (2001).

[36] M. E. Zhitomirsky and T. M. Rice, Phys. Rev. Lett. **87**, 057001 (2001).

[37] M. Blume, J. Appl. Phys. **57**, 3615 (1985).

[38] M. Blume, in *Resonant Anomalous X-Ray Scattering: Theory and Appplications*, edited by G. Materlik, C. J. Sparks, and K. Fischer (Elsevier Science, 1994), p. 495.

[39] D. Gibbs, J. P. Hill, and C. Vettier, phys. stat. sol. (b) **215**, 667 (1999).

[40] J. P. Hannon, G. T. Trammell, M. Blume, and D. Gibbs, Phys. Rev. Lett. **61**, 1245 (1988).

[41] J. P. Hill and D. F. McMorrow, Acta Cryst. **A52**, 236 (1996).

[42] F. Bergevin and M. Brunel, Acta Cryst. **A37**, 314 (1981).

[43] T. Kiyama, Y. Wakabayashi, H. Nakao, H. Ohsumi, Y. Murakami, M. Izumi, M. Kawasaki, and Y. Tokura, J. Phys. Soc. Jpn. **72**, 785 (2003).

[44] H. Ohsumi, Y. Murakami, T. Kiyama, H. Nakao, M. Kubota, Y. Wakabayashi, Y. Konishi, M. Izumi, M. Kawasaki, and Y. Tokura, J. Phys. Soc. Jpn. **72**, 1006 (2003).

[45] G. Cao, L. Balicas, Y. Xin, J. E. Crow, and C. S. Nelson, Phys. Rev. B **67**, 184405 (2003).

[46] C. S. Snow, S. L. Cooper, G. Cao, J. E. Crow, H. Fukazawa, S. Nakatsuji, and Y. Maeno, Phys. Rev. Lett. **89**, 226401 (2002).

[47] J. F. Karpus, C. S. Snow, R. Gupta, H. Barath, S. L. Cooper, and G. Cao, Phys. Rev. B **73**, 134407 (2006).

[48] Y. Yoshida, S.-I. Ikeda, N. Shirakawa, M. Hedo, and Y. Uwatoko, J. Phys. Soc. Jpn. **77**, 093702 (2008).

[49] G. Cao, K. Abboud, S. McCall, J. E. Crow, and R. P. Guertin, Phys. Rev. B **62**, 998 (2000).

[50] V. Varadarajan, S. Chikara, V. Durairaj, X. N. Lin, G. Cao, and J. W. Brill, Solid State Comm. **141**, 402 (2007).

[51] Z. Qu, L. Spinu, H. Yuan, V. Dobrosavljevic, W. Bao, J. W. Lynn, M. Nicklas, J. Peng, T. Liu, D. Fobes, E. Flesch, and Z. Q. Mao, Phys. Rev. B **78**, 180407(R) (2008).

[52] K. Iwata, Y. Yoshida, M. Kosaka, and S. Katano, J. Phys. Soc. Jpn. **77**, 104716 (2008).

[53] S. McCall, G. Cao, and J. E. Crow, Phys. Rev. B **67**, 094427 (2003).

[54] X. N. Lin, Z. X. Zhou, V. Durairaj, P. Schlottmann, and G. Cao, Phys. Rev. Lett. **95**, 017203 (2005).

[55] J. F. Karpus, R. Gupta, H. Barath, S. L. Cooper, and G. Cao, Phys. Rev. Lett. **93**, 167205 (2004).

[56] C. S. Nelson, H. Mo, B. Bohnenbuck, J. Strempfer, N. Kikugawa, S. I. Ikeda, and Y. Yoshida, Phys. Rev. B **75**, 212403 (2007).

[57] G. Cao, X. N. Lin, L. Balicas, S. Chikara, J. E. Crow, and P. Schlottmann, New J. Phys. **6**, 159 (2004).

[58] Y. Yoshida, S. I. Ikeda, H. Matsuhata, N. Shriakawa, C. H. Lee, and S. Katano, Phys. Rev. B **72**, 054412 (2005).

[59] G. Cao, S. McCall, J. E. Crow, and R. P. Guertin, Phys. Rev. Lett. **78**, 1751 (1997).

[60] Y. Yoshida, I. Nagai, S. I. Ikeda, N. Shirakawa, M. Kosaka, and N. Môri, Phys. Rev. B **69**, 220411(R) (2004).

[61] E. Ohmichi, Y. Yoshida, S. I. Ikeda, N. Shirakawa, and T. Osada, Phys. Rev. B **70**, 104414 (2004).

[62] G. Cao, L. Balicas, Y. Xin, E. Dagotto, J. E. Crow, C. S. Nelson, and D. F. Agterberg, Phys. Rev. B **67**, 060406(R) (2003).

[63] O. Friedt, M. Braden, G. André, P. Adelmann, S. Nakatsuji, and Y. Maeno, Phys. Rev. B **63**, 174432 (2001).

[64] G. Cao, L. Balicas, X. N. Lin, S. Chirkara, E. Elhami, V. Durairaj, J. W. Brill, R. C. Rai, and J. E. Crow, Phys. Rev. B **69**, 014404(R) (2004).

[65] W. Bao, Z. Q. Mao, Z. Qu, and J. W. Lynn, Phys. Rev. Lett. **100**, 247203 (2008).

[66] T. Kimura and Y. Tokura, Annu. Rev. Mater. Sci. **30**, 451 (2000).

[67] V. Durairaj, X. N. Lin, Z. X. Zhou, S. Chikara, E. Ehami, A. Douglass, P. Schlottmann, and G. Cao, Phys. Rev. B **73**, 054434 (2006).

[68] H. L. Liu, S. Yoon, S. L. Cooper, G. Cao, and J. E. Crow, Phys. Rev. B **60**, R6980 (1999).

[69] M. N. Iliev, S. Jandl, V. N. Popov, A. P. Litvinchuk, J. Cmaidalka, R. L. Meng, and J. Meen, Phys. Rev. B **71**, 214305 (2005).

[70] J. S. Lee, S. J. Moon, B. J. Yang, J. Yu, U. Schade, Y. Yoshida, S. I. Ikeda, and T. W. Noh, Phys. Rev. Lett. **98**, 097403 (2007).

[71] F. Baumberger, N. J. C. Ingle, N. Kikugawa, M. A. Hossain, W. Meevasana, R. S. Perry, K. M. Shen, D. H. Lu, A. Damascelli, A. Rost, A. P. Mackenzie, Z. Hussain, and Z.-X. Shen, Phys. Rev. Lett. **96**, 107601 (2006).

[72] V. I. Anisimov, I. A. Nekrasov, D. E. Kondakov, T. M. Rice, and M. Sigrist, Eur. Phys. J. B **25**, 191 (2002).

[73] J. H. Jung, Z. Fang, J. P. He, Y. Kaneko, Y. Okimoto, and Y. Tokura, Phys. Rev. Lett. **91**, 056403 (2003).

[74] T. Hotta and E. Dagotto, Phys. Rev. Lett. **88**, 017201 (2002).

[75] I. Zegkinoglou, J. Strempfer, C. S. Nelson, J. P. Hill, J. Chakhalian, C. Bernhard, J. C. Lang, G. Srajer, H. Fukazawa, S. Nakatsuji, Y. Maeno, and B. Keimer, Phys. Rev. Lett. **95**, 136401 (2005).

[76] M. Kubota, Y. Murakami, M. Mizumaki, H. Ohsumi, N. Ikeda, S. Nakatsuji, H. Fukazawa, and Y. Maeno, Phys. Rev. Lett. **95**, 026401 (2005).

[77] T. Nachtrab, C. Bernhard, C.T. Lin, D. Koelle, and R. Kleiner, C.R.Physique **7**, 68 (2006).

[78] P.W. Klamut, Supercond. Sci. Technol. **21**, 093001 (2008).

[79] C. W. Chu, in *Frontiers in Superconducting Materials*, edited by A. V. Narlikar (Springer, 2005), p. 331.

[80] O. Chmaissem, J.D. Jorgensen, H. Shaked, P. Dollar, and J.L. Tallon, Phys. Rev. B **61**, 6401 (2000).

[81] A.C. McLaughlin, W. Zhou, J.P. Attfield, A.N. Fitch, and J.L. Tallon, Acta Cryst. **A52**, 236 (1996).

[82] A. Martinelli, C. Artini, M. R. Cimberle, G. A. Costa, M. Ferretti, R. Masini, and P. Mele, Phys. Rev. B **69**, 052507 (2004).

[83] A. Martinelli and M. R. Cimberle, Z. Kristallogr. **222**, 459 (2007).

[84] R. S. Liu, L.-Y. Jang, H.-H. Hung, and J. L. Tallon, Phys. Rev. B **63**, 024507 (2001).

[85] Y. Tokunaga, H. Kotegawa, K. Ishida, Y. Kitaoka, H. Takagiwa, and J. Akimitsu, Phys. Rev. Lett. **86**, 5767 (2001).

[86] K. Kumagai, S. Takada, and Y. Furukawa, Phys. Rev. B **63**, 180509 (R) (2001).

[87] Z.H. Han, J.I. Budnick, W.A. Hines, P.W. Klamut, M. Maxwell, and B. Dabrowski, J. Mag. Mag. Mat. **299**, 338 (2006).

[88] A. Butera, A. Fainstein, E. Winkler, and J. Tallon, Phys. Rev. B **63**, 054442 (2001).

[89] J.W. Lynn, B. Keimer, C. Ulrich, C. Bernhard, and J.L. Tallon, Phys. Rev. B **61**, R14964 (2000).

[90] J.D. Jorgensen, O. Chmaissem, H. Shaked, S. Short, P.W. Klamut, B. Dabrowski, and J.L. Tallon, Phys. Rev. B **63**, 054440 (2001).

[91] G.V.M. Williams and S. Krämer, Phys. Rev. B **62**, 4132 (2000).

[92] J.L. Tallon, J.W. Loram, G.V.M. Williams, and C. Bernhard, Phys. Rev. B **61**, R6471 (2000).

[93] C.T. Lin, B. Liang, C. Ulrich, and C. Bernhard, Physica C **364-365**, 373 (2001).

[94] I. Zegkinoglou, Ph.D. thesis, Stuttgart, 2007.

[95] E. F. Bertaut, in *Magnetism III*, edited by G. T. Rado and H. Suhl (Academic Press, 1963), p. 149.

[96] E. F. Bertaut, Acta Crystallogr. A **24**, 217 (1968).

[97] M. Reehuis, C. Ulrich, P.Pattison, B. Ouladdiaf, M.C. Rheinstädter, M. Ohl, L.P. Regnault, M. Miyasaka, Y. Tokura, and B. Keimer, Phys. Rev. B **73**, 094440 (2006).

[98] T. Thio, T. R. Thurston, N. W. Preyer, P. J. Picone, M. A. Kastner, H. P. Jenssen, D. R. Gabbe, C. Y. Chen, R. J. Birgeneau, and A. Aharony, Phys. Rev. B **38**, 905 (1988).

[99] O. I. Lebedev, G. Van Tendeloo, J. P. Attfield, and A. C. Mclaughlin, Phys. Rev. B **73**, 224524 (2006).

[100] A. Callaghan, C. W. Möller, and R. Ward, Inorg. Chem. **5**, 1572 (1966).

[101] A. P. Mackenzie and Y. Maeno, Rev. Mod. Phys. **75**, 657 (2003).

[102] R. S. Perry, L. M Galvin, S. A. Grigera, L. Capogna, A. J. Schofield, A. P. Mackenzie, M. Chiao, S. R. Julian, S. I. Ikeda, S. Nakatsuji, Y. Maeno, and C. Pfleiderer, Phys. Rev. Lett. **86**, 2661 (2001).

[103] S. A Grigera, R. S. Perry, A. J. Schofield, M. Chiao, S. R. Julian, G. G. Lonzarich, S. I. Ikeda, Y. Maeno, A. J. Millis, and A. P. Mackenzie, Science **294**, 329 (2001).

[104] A. J. Millis, A. J. Schofield, G. G. Lonzarich, and S. A. Grigera, Phys. Rev. Lett. **88**, 217204 (2002).

[105] H. K. Mueller-Buschbaum and J. Wilkens, Z. Anorg. Allg. Chem. **591**, 161 (1990).

[106] Q. Huang, J. W. Lynn, R. W. Erwin, J. Jarupatrakorn, and R. J. Cava, Phys. Rev. B **58**, 8515 (1998).

[107] H. Shaked, J. D. Jorgensen, O. Chmaissem, S. Ikeda, and Y. Maeno, J. Solid State Chem. **154**, 361 (2000).

[108] H. Shaked, J. D. Jorgensen, S. Short, O. Chmaissem, S.-I. Ikeda, and Y. Maeno, Phys. Rev. B **62**, 8725 (2000).

[109] R. Kiyanagi, K. Tsuda, N. Naofumi, H. Kimura, Y. Noda, Y. Yoshida, S.-I. Ikeda, and Y. Uwatoko, J. Phys. Soc. Jpn. **73**, 639 (2004).

[110] A. Tamai, M. P: Allan, J. F. Mercure, W. Meevasana, R. Dunkel, D. H. Lu, R. S. Perry, A. P. Mackenzie, D. J. Singh, Z.-X. Shen, and F. Baumberger, Phys. Rev. Lett. **101**, 026407 (2008).

[111] R. A. Borzi, S. A. Grigera, R. S. Perry, N. Kikugawa, K. Kitagawa, Y. Maeno, and A. P. Mackenzie, Phys. Rev. Lett. **92**, 216403 (2004).

[112] B. Binz and M. Sigrist, Europhys. Lett **65**, 816 (2004).

[113] S.-I. Ikeda, Y. Maeno, S. Nakatuji, M. Kosaka, and Y. Uwatoko, Phys. Rev. B **62**, R6089 (2000).

[114] L. Capogna, A. P. Mackenzie, R. S. Perry, S. A. Grigera, L. M. Galvin, P. Raychaushuri, A. J. Schofield, C. S. Alexander, G. Cao, S. R. Julian, and Y. Maeno, Phys. Rev. Lett. **88**, 076602 (2002).

[115] S. A. Grigera, R. A. Borzi, A. P. Mackenzie, S. A. Julian, R. S. Perry, and Y. Maeno, Phys. Rev. B **67**, 214427 (2003).

[116] Z. X. Zhou, S. Mc Call, C. S. Alexander, J. E. Crow, P. Schlottmann, A. Bianchi, C. Capan, R. Movshovich, K. H. Kim, M. Jaime, N. Harrison, M. K. Haas, R. J. Cava, and G. Cao, Phys. Rev. B **69**, 140409 (2004).

[117] F. Ronning, R. W. Hill, M. Sutherland, D. G. Hawthorn, M. A. Tanatar, J. Paglione, L. Taillefer, M. J. Graf, R. S. Perry, Y. Maeno, and A. P. Mackenzie, Phys. Rev. Lett. **97**, 067005 (2006).

[118] R. S. Perry, K. Kitagawa, S. A. Grigera, R. A. Borzi, A. P. Mackenzie, K. Ishida, and Y. Maeno, Phys. Rev. Lett. **92**, 166602 (2004).

[119] S. A. Grigera, P. Gegenwart, R. A. Borzi, F. Weickert, A. J. Schofield, R. S. Perry, T. Tayama, T. Sakakibara, Y. Maeno, A. G. Green, and A. P. Mackenzie, Science **306**, 1154 (2004).

[120] R. A. Borzi, S. A. Grigera, J. Farrell, R. S. Perry, S. J. S. Lister, S. L. Lee, D. A. Tennant, Y. Maeno, and A. P. Mackenzie, Science **315**, 214 (2007).

[121] P. Gegenwart, F. Weickert, M. Garst, R. S. Perry, and Y. Maeno, Phys. Rev. Lett. **96**, 136402 (2006).

[122] K. Iwaya, S. Satow, T. Hanaguri, N. Shannon, Y. Yoshida, S. I. Ikeda, J. P. He, Y. Kaneko, Y. Tokura, T. Yamada, and H. Takagi, Phys. Rev. Lett. **99**, 057208 (2007).

[123] L. Capogna, E. M. Forgan, S. M. Hayden, A. Wildes, J. A. Duffy, A. P. Mackenzie, R. S. Perry, S. Ikeda, Y. Maeno, and S. P. Brown, Phys. Rev. B **67**, 012504 (2003).

[124] K. Kitagawa, K. Ishida, R. S. Perry, T. Tayama, T. Sakakibara, and Y. Maeno, Phys. Rev. Lett. **95**, 127001 (2005).

[125] K. Kitagawa, K. Ishida, R. S. Perry, H. Murakawa, K. Yoshimuda, and Y. Maeno, Phys. Rev. B **75**, 024421 (2007).

[126] Y. Liu, R. Jin, Z. Q. Mao, K. D. Nelson, M. K. Haas, and R. J. Cava, Phys. Rev. B **63**, 174435 (2001).

[127] R. Mathieu, A. Asamitsu, Y. Kaneko, J. P. He, X. Z. Yu, R. Kumai, Y. Onose, N. Takeshita, T. Arima, H. Takagi, and Y. Tokura, Phys. Rev. B **72**, 092404 (2005).

[128] T. Kimura, S. Ishihara, H. Shintani, T. Arima, K. T. Takahashi, K. Ishizaka, and Y. Tokura, Phys. Rev. B **68**, 060403(R) (2003).

[129] T. Hotta, M. Moraghebi, A. Feiguin, A. Moreo, S. Yunoki, and E. Dagotto, Phys. Rev. Lett. **90**, 247203 (2003).

[130] R. S. Perry and Y. Maeno, J. Crystal Growth **271**, 134 (2004).

[131] B. Bohnenbuck, I. Zegkinoglou, J. Strempfer, C. Schüssler-Langeheine, C. S. Nelson, Ph. Leininger, H.-H. Wu, E. Schierle, J. C. Lang, G. Srajer, S. I. Ikeda, Y. Yoshida, K. Iwata, S. Katano, N. Kikugawa, and B. Keimer, Phys. Rev. B **77**, 224412 (2008).

[132] M. A. Hossain *et al.*, in preparation .

Publication List

- B. Bohnenbuck, I. Zegkinoglou, J. Strempfer, C. S. Nelson, H.-H. Wu, C. Schüßler-Langeheine, M. Reehuis, E. Schierle, Ph. Leininger, T. Herrmannsdörfer, J. C. Lang, G. Srajer, C. T. Lin, and B. Keimer, *Magnetic Structure of $RuSr_2GdCu_2O_8$ Determined by Resonant X-Ray Diffraction*, Phys. Rev. Lett. **102** (2009), 037205

- B. Bohnenbuck, I. Zegkinoglou, J. Strempfer, C. Schüßler-Langeheine, C. S. Nelson, Ph. Leininger, H.-H. Wu, E. Schierle, J. C. Lang, G. Srajer, S. I. Ikeda, Y. Yoshida, K. Iwata, S. Katano, N. Kikugawa, and B. Keimer, *Magnetic structure and orbital state of $Ca_3Ru_2O_7$ investigated by resonant x-ray diffraction*, Phys. Rev. B **77** (2008), 224412

- J. Strempfer, B. Bohnenbuck, I. Zegkinoglou, N. Aliouane, S. Landsgesell, M. v. Zimmermann, and D. N. Argyriou, *Magnetic-field-induced transitions in multiferroic $TbMnO_3$ probed by resonant and nonresonant x-ray diffraction*, Phys. Rev. B **78**, (2008), 024429

- C. S. Nelson, H. Mo, B. Bohnenbuck, J. Strempfer, N. Kikugawa, S.I. Ikeda, and Y. Yoshida, *Spin-charge-lattice coupling near the metal-insulator transition in $Ca_3Ru_2O_7$*, Phys. Rev. B **75** (2007), 212403

- J. Strempfer, B. Bohnenbuck, M. Mostovoy, N. Aliouane, D. N. Argyriou, F. Schrettle, J. Hemberger, A. Krimmel, and M. v. Zimmermann, *Absence of commensurate ordering at the polarization flop transition in multiferroic $DyMnO_3$*, Phys. Rev. B **75** (2007), 212402

- D. N. Argyriou, N. Aliouane, J. Strempfer, I. Zegkinoglou, B. Bohnenbuck, K. Habicht, and M. v. Zimmermann, *Melting of incommensurate-ferroelectric phase with magnetic field in multiferroic $TbMnO_3$*, Phys. Rev. B **75** (2007), 020101(R)

- A. Krimmel, J. Strempfer, B. Bohnenbuck, B. Keimer, M. Hoinkis, M. Klemm, S. Horn, A. Loidl, M. Sing, R. Claessen, and M. v. Zimmermann, *Incommensurate structure of the spin-Peierls compound TiOCl in zero and finite magnetic fields*, Phys. Rev. B **73** (2006), 172413

Acknowledgements

This work would not have been possible without the support and contributions of many people. Thanks to ...

... Prof. Dr. Bernhard Keimer for giving me the opportunity to carry out this work and for this support during the last four years. Despite his restricted time, he was always open for discussions, from which I strongly benefited.

... Prof. Dr. Peter Michler for accepting the task of reading and reviewing the thesis.

... Jörg Strempfer for supervising me during the first one and a half years of the thesis, in which he taught me the basics of resonant x-ray diffraction, and for the close collaboration after he left the institute.

... Ioannis Zegkinoglou and Philippe Leininger for their support in the x-ray laboratory and during numerous synchrotron experiments and for being a great colleagues, without whom beamtimes would have been less fun.

... Heinrich Klann, Michael Schulz and Manfred Ohl for their help with the x-ray laboratory setup and for designing the sample holders used in the synchrotron experiments.

... Christian Schüssler-Langeheine, Enrico Schierle and Hsueh-Hung Wu for the excellent collaboration and for spending much effort on the preparation of the first experiments at KMC-1.

... Christie Nelson for the fruitful collaboration in the investigation of $Ca_3Ru_2O_7$ and $RuSr_2GdCu_2O_8$.

... Suman Hossain, Maurits Haverkort and Prof. Andrea Damascelli for the good collaboration in the investigation of Mn doped $Sr_3Ru_2O_7$.

... Jonathan Lang, George Srajer and the staff of Sector 4 for the excellent support during the experiments at beamline 4-ID-D, Franz Schäfers and Marcel Mertin for their help during the beamtimes at KMC-1, Martin von Zimmermann for his support during the experiments at BW5, Esther Dudzik and Ralf Feyerherm for their help during beamtime at the MagS beamline.

... the crystal growers Naoki Kikugawa, Shin-Ichi Ikeda and Yoshiyuki Yoshida for providing $Ca_3Ru_2O_7$ single crystals, Chengtian Lin for growing $RuSr_2GdCu_2O_8$ samples, Yoshiyuki Yoshida, Prof. Yoshinori Tokura and his collaborators for providing

Mn substituted $Sr_3Ru_2O_7$ crystals.

... Manfred Reehuis for performing a representation analysis of the magnetic structure of $RuSr_2GdCu_2O_8$.

... all former and present members of Prof. Keimer's group for the good atmosphere in the group.

... the "lunch and coffee" group for many interesting discussions about all kinds of topics: Eva Benckiser, Daniel Haug, Maurits Haverkort, Vladimir Hinkov, Dmytro Inosov, Yulia Matiks, Martin Rahlenbeck, Anton Suchanek and Ioannis Zegkinoglou.

... my family and friends for their constant support during my studies and the PhD thesis.